Università
degli Studi
di Ferrara

ISTITUTO
ITALIANO DI
TECNOLOGIA

DOCTORAL COURSE IN
TRANSLATIONAL NEUROSCIENCE AND
NEUROTECHNOLOGIES

CYCLE XXXVI

COORDINATOR Prof. Fadiga Luciano

NOVEL ORGANIC AND BIOHYBRID STRATEGIES TO IMPROVE NEURAL INTERFACES BIOCOMPATIBILITY

Scientific Disciplinary Sector (SDS) BIO/09

Candidate	**Supervisor**
Dott. Guzzo Sonia	Prof. Bianchi Michele
(signature)	*(signature)*

Year 2020/2023

ABSTRACT

The field of brain interface devices underwent extensive investigation in the last decades, opening up previously unconceivable possibilities for understanding and treating neurological systems, thus establishing a bidirectional communication between the apparently distant domains of biology and technology. The desire to reach the full potential of brain interface devices has inspired a booming sector of research and innovation, showing the potential to transform the fields of neuroprosthetics, brain-computer interfaces, and basic neuroscience. This technological and scientific endeavor would serve the double purpose of allowing mankind to cure severe medical disorders while also gaining deep knowledge about structural, functional and signaling features of the nervous system. However, the establishment of a long-term functionally stable interface between electrodes and tissue is still a major challenge, and interfacial failures on both sides of the biotic/abiotic interface remain the main compromising factor for devices' lifetime and performance. To overcome this issue, neural interfaces based on advanced biomaterials capable of seamlessly merging with neural tissue and ensuring long-term stable performances would be highly desirable; one of the most significant steps in their development being the assessment of biocompatibility.

This thesis explores the enhancement of neural device performance and longevity by investigating non-conventional materials for electrode and substrate coating. Biocompatibility of materials is evaluated, considering cytotoxicity, inflammation, and long-/mid-term stability, in a framework of cross-validation amongst the most established procedures and standards typically utilized for this assessment.

Additionally, a tissue engineering approach at the interface of the device is presented and discussed, aiming to enhance the interaction and communication between implanted electrodes and adjacent tissue by mitigating the inflammation that typically arises upon implantation. The functionality of this approach is validated through both *in vitro* and *in vivo* testing, showing superior performance with respect to non-engineered devices.

This thesis stands combines the domains of material science, tissue engineering, biology, and clinical medicine, emphasizing the inherent interdisciplinarity of brain interface device development and highlighting the crucial role that collaboration across these fields has played and will play to shape the trajectory of future development in neuroscience and healthcare.

1. INTRODUCTION

This chapter aims to provide a brief discussion on the scientific background of this thesis. Brain-machine interfaces are introduced, and their biocompatibility is discussed, with a focus on the biological foundations of the foreign body reactions. Additionally, the chapter presents Organic Bioelectronics and tissue engineering approaches aimed at ameliorating brain machine interfaces biocompatibility.

1.1 BRAIN MACHINE INTERFACES

The quest to understand and interface the human nervous system has been a driving force in biomedical research for decades. The advent of neural interface devices has revealed itself as a revolutionary technology with the potential to enhance our comprehension of nervous system mechanisms, hence offering opportunities to restore the quality of life for individuals afflicted with neurological illnesses. These devices provide bidirectional communication and control, thereby establishing a connection between organic brain networks and artificial systems. The efficacy of neural interface devices is strongly dependent upon the selection of biomaterials utilized for their fabrication and the comprehensive assessment of their biocompatibility[1]. The human brain is an intricately structured and highly dynamic organ that exhibits a remarkable level of complexity. Its intricate neural networks play a crucial role in orchestrating a wide array of cognitive functions, encompassing sensory perception and motor control, which are vital to the manifestation of human consciousness[2]. The development of brain-machine interfaces (BMIs), a pioneering discipline that integrates principles from engineering and neuroscience to provide direct communication between the brain and external devices, is a potentially significant achievement within this field of scientific investigation. Early experiments on brain-machine interfaces date back to the middle of the 20th century[3]. In recent times, BMIs have gained significant attention from both the scientific community and society as a whole. This has been made possible by technological developments, enhanced comprehension of neurophysiology, and an increasing need for interventions to tackle neurological illnesses and enhance human capacities[4]. By deciphering neural activity patterns, BMIs enable individuals to control prosthetic limbs [5]and to communicate using solely neural signals[6]. They have the potential to greatly improve the quality of life of people who suffer from paralysis or limb loss by restoring the lost sensory or motor functions, as well as to redefine the limits of human capability. Furthermore, BMIs have found applications in cognitive neuroscience, providing insights into neural plasticity, learning, and memory[7]. This developmental work proceeds via continuous iterations between technological development and depth and complexity of the scientific questions that can be addressed by technological means, which, on their turn, orient upcoming technological development, in a virtuous cycle triggering continuous endeavor by scientists, with the final aim of understanding the neural underpinnings of cognition, behavior, and disease.

Neural electrodes play a pivotal role in enabling the investigation of the interplay between the brain structure and its operations, by performing two primary functions: namely recording and stimulation. Importantly, the efficacy of neural electrodes is commonly hindered by a persistent decline in recording fidelity, eventually resulting in complete electrode failure. One significant factor contributing to the occurrence of such failures across extended timescales is the inflammatory reaction of the host's immune system towards the implanted device. The presence of acute and chronic inflammation following electrode insertion leads to the stimulation of glial cells in the host, to the production of reactive oxygen species (ROS), and to the depletion of neurons in close proximity of the implant, thus hindering the devices from achieving their maximum effectiveness in terms of signal quality, stability and, as a consequence, informativeness. As already said, a key material/device aspect that must be taken into account in order to minimize such undesired detrimental effects is biocompatibility.

The following sections examine in detail the issue of biocompatibility in neural interfaces (section 1.2), introducing the technological framework of deep brain probes (section 1.2.1) and their biological effects at the tissue level by reviewing in detail the biological mechanism that causes implant failure in the case of poorly biocompatible implants from a biochemical/physiological perspective (section 1.2.2). In addition, possible approaches to improve the biocompatibility of brain probes will be addressed (section 1.3), discussing coatings in unconventional active materials (section 1.3.1) and tissue engineering (section 1.3.2).

1.2 BIOCOMPATIBILITY

The concept of biocompatibility in neural interfaces encompasses the ability of these devices to integrate seamlessly with neural tissue and with the broader biological environment, without inducing harmful reactions or damage. The importance of biocompatibility in neural interfaces is multifaceted and includes several key aspects, which are hereafter briefly individually discussed. To serve their intended purpose effectively, neural interfaces must remain functional for extended periods of time withing the neuronal environment, this allows us to identify *longevity* and *retention of device functionality* as main key aspects. Amongst the feasible strategies to preserve this key aspect, a crucial role is played by the *Minimization of Immune Responses*, which, although being physiological and protective, leads to inflammation, scar tissue formation, and device rejection. Such minimization can be achieved via *tissue integration*, namely by promoting the growth of neural cells around and within the device, enabling electrical and chemical communication between the device and the neural circuits. Biocompatible neural interfaces should facilitate integration with surrounding neural tissue. Using biocompatible materials is an enabling strategy to address all these key aspects, since biocompatible materials and coatings are designed to minimize immune response and promote long-term integration with the surrounding neural tissue, thus preventing the degradation or failure of BMIs over time and ensuring the preservation of their ultimate functional role, the collection of signals of optima quality for an ideally infinite timespan.

The strategies to achieve biocompatibility in neural interfaces are synergistic, and encompass material science (e.g., the integration of medical-grade silicones, titanium, and variegated coatings to encapsulate device components in BMIs), pharmacology (e.g., immune-modulating drugs) and biotechnology (i.e., tissue engineering) with the final aim of managing neuroinflammation, reducing immune responses and promoting tissue integration.

1.2.1 Deep brain electrode technologies

The origins of Deep Brain Probes (DBPs) may be traced back to the pioneering research carried on by Delgado in 1952.[8] Delgado demonstrated active control of brain activity in animals by means of implanted electrodes to manipulate, providing initial proofs on concept concerning deep brain exploration and neuromodulation. In the last 70 years, deep brain electrodes have been applied towards a plethora of aims, ranging from fundamental research to clinical interventions. DBPs have empowered researchers to map neural circuits responsible for complex behavior[9], investigate the neural bases of decision-making [10], and delve into the mechanisms underlying neurological disorders such as Parkinson's disease [11].

The most established neural prosthesis based on DBPs is the cochlear implant, designed to address severe hearing loss caused by insufficient stimulation of the hair cells. These devices employ multiple stimulating electrodes positioned at various locations along the auditory nerve, to convey electrical signal elicited by an apparatus of sound collection directly to specific hair cells, thus circumventing the impaired cochlea. This concept can eventually be extended to any electrogenic tissue, be it skeletal, smooth muscle, neural, or cardiac, where electrodes are frequently employed as stimulators.

One of the most transformative applications of DBPs is, indeed, Deep Brain Stimulation (DBS), which has emerged as a powerful tool for managing treatment-resistant neurological and neuropsychiatric conditions, offering newfound hope and relief to countless patients[12]. DBS is a neurosurgical technique that involves the implantation of electrodes in specific brain regions to modulate neural activity. Over the years, DBS has evolved, with a significant distinction arising between open-loop and closed-loop stimulation systems. Open-loop stimulation involves the continuous delivery of predefined electrical impulses, while closed-loop systems adapt stimulation in response to variation of electrophysiological data collected in real time from the patient, enabling personalized and optimized treatment. Target locations and DBS parameters are in all cases derived by researchers and neurosurgeons according to their knowledge of neural activity gained through DBP studies.

The development of DBPs went way further the mere objective of stimulation with metal electrodes (which was their primal purpose), and nowadays resulted in a variegated spectrum of bidirectional interfaces which, besides efficiently acting as stimulators, are envisioned to act as sophisticated sensors towards physiological data. In particular, DBPs' inherent capability of collecting electrophysiological signals is sought to be paired with chemical sensing, monitoring a wide range of biomarkers, from pH levels up to the detection and quantification of specific pathophysiologically relevant molecular species. Despite these ambitious goals, it is worth noticing that deep-brain electrodes, just as many other implantable devices commonly employed in clinical practice, still suffer from poor integration (especially in the long term) and performance loss due to non-optimized device design.

One of the main factors to consider in this optimization is the mechanical mismatch between the implant and the receiving tissue, which is amongst the leading causes of impaired long-term integration. The performances of the device post-transplantation are greatly influenced by the stiffness of both the target tissue and the device, hence DBP design cannot ignore mechanical considerations, and it is imperative to engineer DBPs encompassing a wide range of Young's moduli to optimize the interaction with distinct tissue types. (Fig.1).

Except for bones and teeth, most biological tissues are soft and exhibit elastic moduli that vary between hundreds of Pa (e.g. the central nervous system) and $\approx 10^5$ Pa (e.g. arteries, kidneys, and lungs)[13]. On the other hand, commonly employed DBPs are composed of materials such as silicone and metals, exhibiting Young's moduli over 1GPa. Furthermore, biological tissue stiffness can undergo modifications as a consequence of the insurgence of pathological conditions, such as fibrosis.

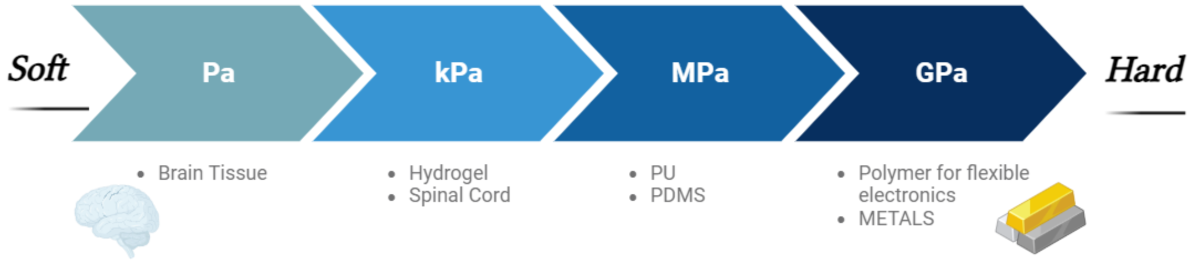

Fig.1 | Mechanical mismatch between soft neural tissues and widely used electronic implants. Created with BioRender.com

The main effect of the mechanical mismatch is, quite obviously, trauma. Indeed, the little movements of the brain at a micro-level and the resulting displacement in relation to the implanted electrode give rise to shear stress and von Mises's stresses exerted on, and harmful for, the adjacent tissue. These persistent stresses are detrimental not only for the tissue but also for the implanted device itself, and result in device failure and permanent structural modification at the interface between the biotic and abiotic components.

Unfortunately, this problem cannot be overcome by simply decreasing *ad libitum* the Young's modulus of the implants. If, on the one hand, a certain degree of softness effectively mitigates the inflammatory reaction of the surrounding tissue and the mechanical stresses described above, on the other hand it lowers the probability of an efficient implantation. Indeed, a suitable level of rigidity is necessary to facilitate DBP insertion into brain tissue.

To guide the design of DBPs in finding the proper balance between stiffness and softness, a quantitative description of the involved forces is mandatory. One of the main aspects to be considered within this framework is the maximum load force that the DBPs can tolerate upon insertion without breaking, quantitatively expressed by the buckling force.

The buckling Force (F) can be calculated using the Euler formula:

$$\boldsymbol{F} = \frac{\boldsymbol{\pi}^2 \boldsymbol{IE}}{(\boldsymbol{KL})^2}$$

Here, the moment of inertia is represented by $\boldsymbol{I}$, the effective length factor is denoted by $\boldsymbol{K}$ and accounts for the presence of mechanical vincula at both ends of the DBP, the electrode length is represented by $\boldsymbol{L}$, and the material's Young's modulus is denoted by $\boldsymbol{E}$.

Hence, the utilization of flexible materials (i.e., small E) diminishes the magnitude of F, thereby potentially hindering the probe's capability to penetrate the meninges or to reach the desired target area. To mitigate the issue of buckling failure (i.e., to increase F), it is possible to coat the device, thus increasing I. Most explored coating layers are made of biodegradable substances, such as gelatin[14] and silk[15]. Apart from mechanical stability, coating layers add a degree of freedom in endowing DBPs with functional features. The utilization of biocompatible and biodegradable polymers has indeed been demonstrated to mitigate persistent immune response and glial scarring.

Immediately following the time of implantation, a cascade of biological factors is triggered, leading first to the adsorption of plasma proteins onto the surface of DPBs. The presence of adsorbed proteins such as albumin, fibrinogen, complement, fibronectin, vitronectin, globulin, and others modulate host inflammatory cell interactions and adhesion and are thus linked to subsequent inflammatory and wound healing responses[16].

The biomaterial surface proprieties worth influence a plethora of factors encompassing the type of the attracted protein, the concentration of them and their conformation. Hence, to hinder these adsorbed protein layer onto the surface of the implanted device the utilization of non-fouling materials has been studied as an approach.

Materials such as polyhydroxyethylmethacrylate (PHEMA) PEG (polyethylene glycol)[17], tyrosine-derived terpolymers[18], and silk itself[15] have been extensively employed toward this aim; unfortunately, they have encountered challenges in sustaining their desirable low fouling characteristics over the required chronic implantation time[19].

In the last decades, conductive polymers such as polypyrrole and PEDOT, have emerged as promising materials due to their interesting characteristics and increasing application in electronic devices. These polymers have been utilized not only as flexible substrates in brain probes but also as electrodes or coatings on electrodes justifying their application on capability of improving the biocompatibility of the system while simultaneously enhancing the device electrical performance and the signal-to-noise ratio (SNR).

1.2.2 Foreign Body Reaction

Apart from mechanical considerations, a crucial cause of DBP failure lies in the complex and multifaceted tissue response, commonly known as the Foreign Body Reaction (FBR). Together with tissue inflammation and immune responses, FBR has profound implications on the utility and safety of these devices[20].

The trauma caused by DBPs implantation triggers the inflammatory cascade which begins at the moment of implantation, known as *acute phase*, and persists up to the formation of a glial scar around the electrode (*chronic phase*), that results in the deterioration of electrode and surrounding tissue, thus irremediably compromising device functionality. [16,21]

Despite the variety of brain’s mechanical and chemical self-protection features, such as the cerebrospinal fluid (CSF) and the blood brain barrier (BBB), it still remains easy to damage it.

The CSF serves as a crucial mechanism for the removal of metabolic waste and offers protection against physical harm to the tissue by endowing it with buoyancy, enabling it to remain suspended without the application of pressure, mitigating sudden movements of the skull. Additionally, endothelial cells provide a barrier that facilitates the segregation of CSF from the capillaries.

Another fundamental brain self-protection system is represented by the blood -brain barrier (BBB) that expresses a complex *ensemble* of activity and characteristics which have, as their common purpose, the wellness of the brain. The BBB is constituted by endothelial cells, pericytes, and astrocytic end-feet, which together form a barrier able to protect the brain's delicate neuronal tissue, deliver glucose, oxygen, and other nutrients to the central nervous system (CNS), while preventing the contact between the brain and any unwanted/toxic moiety that may be circulating in the bloodstream. However, the BBB can easily be breached by the implanted DBPs, leading to pathophysiology of neurological autoimmune disorders[22]. Additionally, leukocytes' propensity to amplify neurotoxic inflammation after entering the CNS further complicates the management of CNS inflammation[23].

As mentioned in the previous section, upon implantation, biomedical devices are immediately covered by a layer of adsorbed proteins such as collagens, laminins, fibronectin, and members of the complement system. This layer is recognized by the immune system and dictates the course of the FBR[24]. Monocytes and macrophages are recruited to the site of the implant, attracted by chemokines (released by the blood-clotting system) and inflammatory molecules (released after tissue injury). This signaling cascade, over time, eventually triggers the fusion of macrophages to form foreign-body giant cells, which attach to the biomaterial, thereby damaging the implant[20]. Macrophages cannot phagocytize large-sized biomaterials and, therefore, release reactive oxygen species (ROS) and degradative enzymes that create an acidic environment around the implant. Such modification of the chemical environment in the implant niche represents one of the main processes responsible for device failure[25] and death of the surrounding neurons, as result of an overabundance of these chemical releases[26–28]. The main consequence of this is the impossibility to restore the electrical performances of the electrode (both in terms of recording and stimulation) and to observe adequate neuronal signals with the chosen DBP.

The timescale of FBR is structured, and encompasses two major phases, termed *acute* and *chronic* as described below (Fig.2).

The acute FBR is initiated when the electrode is implanted in the brain parenchyma, this immediately leads to breach of the BBB, tissue damage, edema, and death of neuronal and glial cells[20]. Bloodborne cells, erythrocytes, platelets, infiltrated peripheral macrophages, and inflammatory factors are then released from disrupted blood vessels within minutes to hours after implantation, activating resting astrocytes and microglia[25].. Microglia-secreted compounds such as neurotoxic factors and cytokines lead to significant neuron death in the vicinity of the electrodes and result in a region of decreased neuron density, also referred to as the "kill zone" [29,30].. Although the acute response phagocytizes cellular debris and partly repairs the initial wound, the constant *in situ* presence of the electrode leads to a chronic FBR.

The chronic FBR is characterized by reactive astrocytes and activated microglia that construct a glial scar in the proximity of the neural interface. The activated microglia secrete lytic enzymes and ROS to remove foreign material and release pro-inflammatory cytokines such as IL-1 and IL-6 that activate astrocyte proliferation[31]. However, if the electrode material is insoluble or non-biodegradable, macrophages and microglia amalgamate into multi-nucleated foreign-body giant cells and continuously attempt phagocytosis, in which they consistently secrete degradative factors[32,33].As a result, a fibrotic layer that can reach thicknesses of several millimeters is formed[34] with significant negative impact on the biotic/abiotic interfaces, especially in the cases of devices aimed at capturing signals from biological tissue, such as recording electrodes[32]. The fibrotic layer acts as a physical barrier that can hinder or prevent the transport of compounds and/or electrical charge carriers across the interface. The consolidation of the glial scar results in a substantial impedance increase, concurrently causing the displacement of neurons from electrodes.

Consequently, this displacement leads to a reduction in the strength of neural signals, which are already of minimal magnitude, up to an extent where their detectability may be compromised. In certain applications involving the recording of single neuron activity, it has been observed that scars with thicknesses as small as 100µm are capable of completely concealing neurons from electrodes[35].

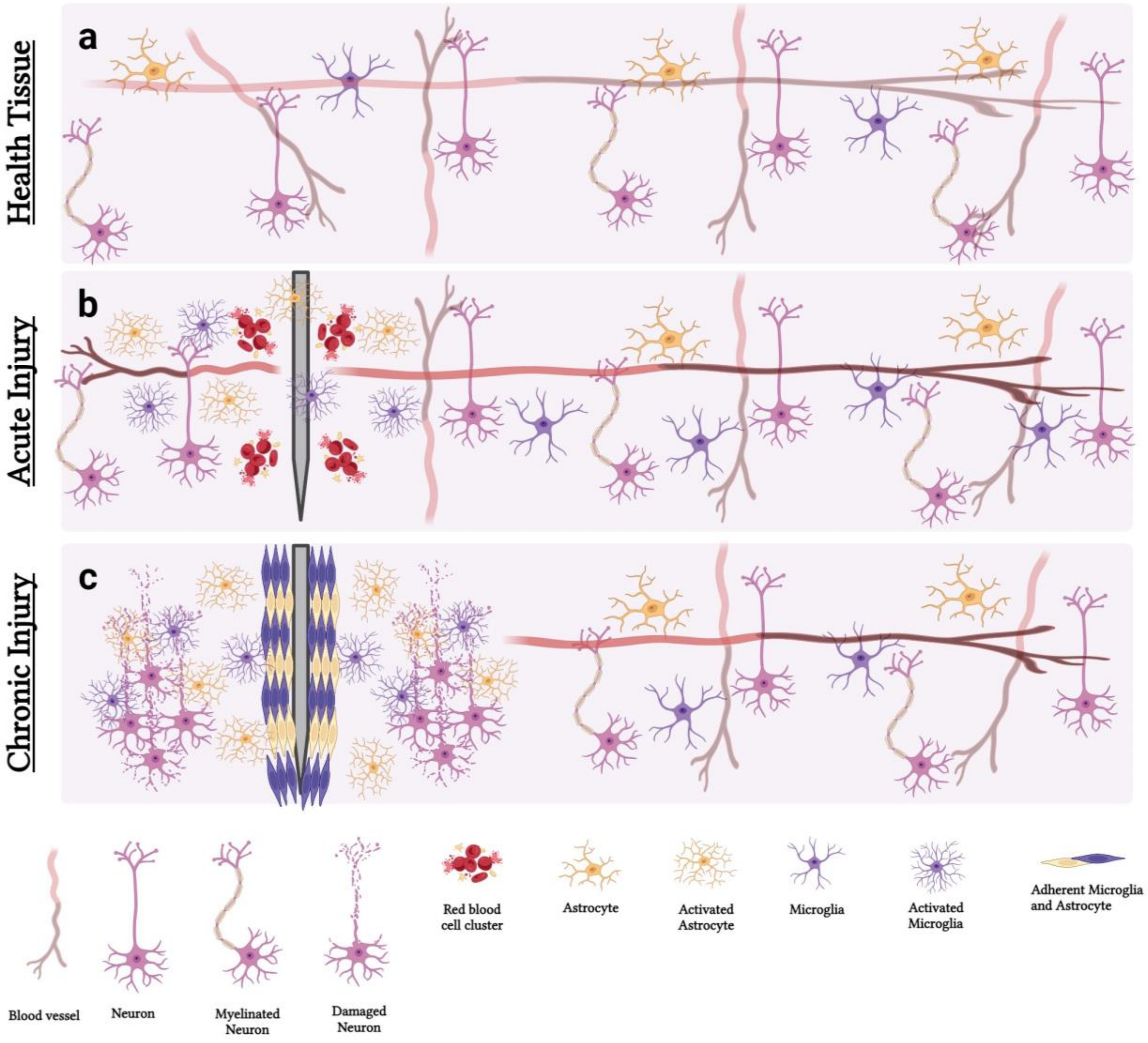

Fig.2 | Schematic representation of the FBR. (a) standard brain cellular arrangement. (b) The acute reaction is distinguished by the rupture of the blood-brain barrier and microvascular system, the activation of astrocyte and microglial cells, as well as the infiltration of blood-derived cells and proteins. (c) The chronic reaction causes an isomorphic glial scar to form, enclosing the implant surface. Created with BioRender.com

Advances in material science, including the development of bioactive coatings and flexible electrode arrays, have shown promises in reducing the foreign body response[36]. Additionally, strategies such as immunomodulation and anti-inflammatory interventions hold potential for enhancing device biocompatibility[37].

Among the huge amount of pharmaceutical approaches towards FBR reduction studied in latest years, one notable instance is the effective application of dexamethasone[38], a corticosteroid commonly used to interfere with fibroblast activation. This anti-inflammatory molecule has been applied in many studies with implantable electronic devices, resulting in a reduction of FBR in the brain[39,40]. Additional anti-inflammatory agents, such as rapamycin[41] and aspirin[42], have exhibited potential efficacy in mitigating inflammation.

1.3 IMPROVING BIOCOMPATIBILITY OF BMIs

As we have extensively explained previously (section 1.2), achieving long-term functionality and minimizing adverse immune responses are currently significant challenges in the field of BMIs. Among emerging strategies, both careful selection of biomaterials and tissue engineering emerge as promising approaches to improve the biocompatibility of BMIs.

Biomaterial selection plays a key role in minimizing immune responses by offering the creation of platforms with mechanical and chemical properties possibly similar to the extracellular matrix of the brain, while possibly endowing the implant with additional functionalities.

As for tissue engineering strategies, these involve seeding, cell ingrowth and incorporation of neural or stem cells on the surface of the BMI, promoting tissue integration and stability.

The integration of these approaches promises to develop BMIs, unlocking new possibilities for neuroprosthetics and their permanent maintenance by avoiding the need for repeated surgical interventions on the same individual, which are necessary in case of electrode failure as a result of glial scarring.

The following sections provide a detailed overview of the above strategies.

1.3.1 Organic electronic materials

The utilization of organic electronic materials has been extensively explored in various technological domains. Recently, there has been a growing interest in employing organic electroactive polymers, be them conductors or semiconductors, for various bioelectronic applications due to their peculiar mechanical and electrical proprieties[43].

Biological tissues are commonly constituted of carbon-based macromolecules and polymers that possess soft and elastic characteristics. Within these biological systems, communication is typically facilitated through a combination of electronic and ionic conduction. This distinctive features enable biotic tissues to exhibit mechanical and conduction properties that are comparable to those observed in organic (semi-)conductors[44].

When designing neural interfaces, especially in the cases of miniaturized electrodes, it is compulsory to envision strategies to reduce the electrode impedance. Such strategies often involve meso- and nano-structuration of the electrode surface, in order to increase surface area and equivalent interfacial capacitance. The utilization of metal deposition methods towards this purpose can result in adverse chemical surface interactions over extended time of employment[45]. Conversely, the application of conductive polymers (CPs) as electrode coatings succeeds in enhancing surface roughness and porosity, thus complying with the purpose of enhancing signal recording and stimulation, while remaining electrochemically safe. Because of their inherent porosity and mixed ionic-electronic conduction, conductive polymers produce excellent electrode-electrolyte interfaces. High charge injection limits and low impedances may be achieved by these devices, which have been effectively utilized for both stimulation and recording purposes[46]. The wide surface area that such materials expose to electrolytes enables unprecedentedly high equivalent capacitances per unit of projected area, with respect to standard metal electrodes, which can compensate the inevitable rise in electrode impedance subsequent to miniaturization (e.g. in deep brain recordings)[47].

Consequently, CP coating enhance interfaces’ ability to store charges, reducing both electrode polarization and heat generation when used for neurological stimulation[48,49]. An additional outcome of impedance reduction is, as obvious, the enhancement of SNR in the context of in vivo brain recording. Furthermore, the soft mechanical properties of these materials render them compatible with biological tissues, and they often exhibit minimal levels of biotoxicity.

In the following sub-sections, the CPs used in the context of this thesis are presented and discussed in detail.

1.3.1.1 PEDOT:PSS

Poly(3,4-ethylenedioxythiophene):poly(styrenesulfonate) (PEDOT:PSS) has garnered significant attention and undergone extensive research within the realm of organic electronics (Fig.3). The applications of this material encompass a wide range of uses, including its utilization as an active layer in solar cells and organic light-emitting diodes. It is also employed as a mixed ionic-electronic conductor in electrolyte-gated organic transistors and multielectrode arrays (MEAs). Additionally, it serves as a charge storage material in supercapacitors and as an antistatic layer in photo films and shielding coatings[50,51] . The attractiveness of this material stems from its notable figures of merit, including its high conductance and capacitance [52], stability, mixed ionic-electronic conduction [53], and potential for scalable production processes, facilitated by the availability of many commercial aqueous formulations[54]. In the context of bioelectronic and neuroelectronic applications, where organic electronic devices serve as intermediaries between biological signals and electronic hardware, the biocompatibility of conductive polymers must be ensured, particularly in cases where long-term applications are anticipated[43].

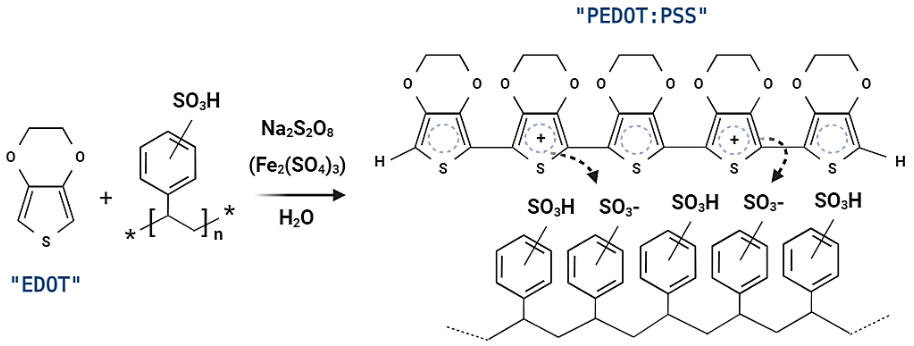

Fig.3 | Chemical synthesis and structure of PEDOT:PSS. Monomer polymerization in the presence of polystyrene sulfonic acid results in an aqueous PEDOT:PSS dispersion Created with BioRender.com

The performances of PEDOT:PSS are significantly influenced by the synthesis conditions and the doping state, enabling modification of its electrical and mechanical properties.

The oxidative polymerization of the 3,4-ethylenedioxythiophene (EDOT) monomer demands the presence of a counterion to ensure solubility of the product and to stabilize the otherwise unbalanced positive charges introduced upon polymerization (either chemical or electrochemical) in the PEDOT backbone. When PEDOT:PSS is chemically synthesized (as in Fig.3), it forms polymeric particles with positively charged PEDOT cores surrounded by poly-anionic PSS shells, the latter providing enough stability for PEDOT+ chains to be dispersed in water[55]. Conductive PEDOT:PSS films can also be grown on metal or on conductive oxide electrodes by dissolving monomeric EDOT in aqueous solution and applying galvanostatic (constant current) or potentiostatic (constant voltage) procedures in the presence of PSS, allowing mask-less coating[56]. Chemically polymerized PEDOT:PSS is now commercially available in aqueous dispersions with varying conductivity, viscosity, and transparency under the trade name Clevios^{TM}, which identifies a family of formulations that differ primarily on the basis of the PEDOT to PSS ratio; as a general trend, conductivity increases with this ratio[57].

When cast on commonly used substrates, such as glass or metals, PEDOT:PSS often exhibits relatively low levels of adhesion[58]. Hence, the use of silanes, such as (3-glycidyloxypropyl) trimethoxysilane (GOPS), is a typical practice to enhance the mechanical stability of coatings, while also partially enhancing their conductivity and biocompatibility[59] . Due to the mentioned factors, there is a strong need within the field of organic bioelectronics for alternative formulations of PEDOT that possess excellent conductivity, sufficient biocompatibility, and do not necessitate the use of supplementary dopants or additives.

1.3.1.2 PEDOT:Nafion

Nafion is a linear copolymer, synthesized through the combination of tetrafluoroethylene with either perfluorosulfonic acid or perfluorocarboxylic acid monomers.[60,61] The literature contains a limited number of reports regarding the use of PEDOT:Nafion in the field of biomedical device applications. Recent studies have investigated electrodeposited PEDOT:Nafion as electrode coating in neural recording and stimulation scenarios, suggesting that PEDOT:Nafion is comparable to PEDOT:PSS in terms of neural recording, electrochemical, morphological, and electrophysiological characteristics in vivo[62].

Furthermore, electrodeposited PEDOT:Nafion coatings result in interfaces with superior capacitance and ion exchange properties, when compared to electrodeposited PEDOT:PSS ones. PEDOT:Nafion is characterized by a a minimal polarization duration (<1ms) during electrical stimulation, leading to a charge injection limit that is approximately 80% greater than the one of PEDOT:PSS. Consequently, it is considered a promising option for both neural recording and stimulation applications[63] . In addition a study on a chemically synthesized formulation of PEDOT:Nafion that is water-based has been recently published. This formulation exhibits fast ion transport and demonstrates resistance to delamination, even without the use of adhesion promoters[64] . The successful integration of this formulation into the production of electrolyte-gated organic transistors (EGOTs) and neuromorphic devices has been made possible thanks to its compatibility with wet additive fabrication techniques such as spin coating or drop casting[64]

1.3.2 Tissue engineering

If tissues or organs have undergone significant damage or loss due to conditions such as cancer, congenital anomalies, or trauma, conventional pharmaceutical interventions may no longer be efficient. In such circumstances, the preferred approach for restoring the affected tissues or organs is the utilization of artificial organs/tissue or organ transplantation. Significant progress has been made in the field of biomedical engineering over the past three decades, leading to notable enhancements in artificial organ technology, resulting in the newborn scientific/technological field of tissue engineering.

Despite these advancements, there is still a need for further improvements in terms of biocompatibility and bio-functionality[65].

The contemporary field of organ transplantation is characterized by two primaries major challenges: namely, scarcity of available donor organs and immunological rejection.

The landscape of modern biomedical engineering is defined by a persistent pursuit for innovative technologies able to seamlessly integrate with biological systems, offering groundbreaking solutions to such longstanding challenges, encompassing medicine and biology. The first goal of tissue engineering is to effectively repair or substitute impaired tissues and organs within a living organism. However, it can also be utilized in the creation of miniature engineered tissue constructs that can function as *in vitro* models for diagnostic screening, drug and toxicology testing, fundamental investigations into tissue and cell behavior [66]. In the context of BMIs biocompatibility enhancement, such constructs can establish a biological barrier between the interface and the tissue[67]. One of the main *in vitro* tissue engineering processes concerns the manipulation of cells in a controlled laboratory environment, with the aim of replicating the functional characteristics of fully developed tissue structures outside of a living creature (e.g., within a laboratory dish prior to their transplantation into living organisms). An example of this is the development of engineered bladder tissues, where autologous urothelial and muscle cells derived from a bladder biopsy are expanded in culture dish to be subsequently seeded onto a biodegradable scaffold with a bladder-shaped structure, composed either of collagen alone or of a composite material consisting of collagen and polyglycolic acid, in order to be implanted into the same patient after 7 weeks. [68,69].

In parallel to this *ex vivo/in vitro* paradigm, the field tissue engineering can focus also on *in vivo* applications, aimed at developing the inherent regenerative capabilities of the body. This approach primarily involves the recruitment of endogenous stem cells and their interaction with implanted biomaterials and scaffolds. The tissues integrated into such artificial constructs are intentionally kept at a low level of functional maturity, in order to allow the acquisition of mature tissue only after the body's response and natural regeneration[69].Such ambitious goal is achieved by the synergic integration, in the implants, of three fundamental components: cells, scaffolds, and growth factors. Obviously, these elements and their means of integration can be arbitrarily varied, and their interplay can result in a wide spectrum of different therapeutic strategies, according to peculiar needs of the host tissue and/or of the target pathology.

In conjunction with their therapeutic utility, biohybrid devices enable us to probe the intricate interplay between biological processes and engineered systems. Indeed, by integrating living cells or tissues into synthetic devices, we gain unprecedented insights into cellular behavior, tissue responses, and disease mechanisms[70]. This synergy between biology and engineering empowers researchers to create dynamic *in vitro* models that faithfully replicate complex physiological environments, offering valuable tools for drug screening, disease modeling, and personalized medicine[71].

The science of tissue engineering has experienced significant advancements, resulting in the continuing creation of biological substitutes for various tissues within the human body. The development of tissue-engineered products, such as a kidney support system incorporating encapsulated urothelial cells, is used for treating individuals suffering from kidney failure[72]. Likewise, liver assist systems that involve enclosed hepatocytes have been employed in clinical settings to offer support to patients experiencing liver failure[73] and encapsulated pancreatic islets has been utilized as a therapeutic approach for managing diabetes[74]. Currently, researchers are engaged in the development of engineered cardiovascular tissues, specifically heart valves[75] and blood vessels[76]. For over a century the utilization of human amniotic membrane (AM) as a grafting substance has been practiced, either in its pristine or decellularized form. AM possesses more significant attributes for the treatment of corneal abnormalities, diabetic foot ulcers, and severe skin burns[77,78]. For instance, there has been a longstanding suggestion that the transplantation of non-preserved human AM in individuals with acute chemical eye burns could potentially mitigate surface inflammation, enhance patient comfort, and mitigate the severity of vascularization[79]. Furthermore, the utilization of autografts composed of amniotic tissue has been observed as a viable option for autologous grafting in several pediatric neurosurgical interventions, including the treatment of myelomeningocele. This approach has distinct advantages, as it eliminates the potential hazards associated with rejection, foreign-body reactions, and transfer of slow viral infection[80]. Human AM has shown promising therapeutic potential for re-epithelialization in the treatment of non-responsive venous ulcers. Additionally, it offers a cost-effective alternative to existing skin substitutes[81]. In recent times, there is a growing body of evidence indicating that human AM has the potential to serve as a financially viable wound dressing option in split-thickness skin grafts[82].

More recently, researchers have been trying to manipulate the nervous system through different processes. Among them, encapsulating genetically modified neural cells which secrete ciliary neurotrophic factor (CNTF)has been explored for the development of nerve guidance channels, focused on the purpose of regenerating peripheral nerves[83] and repairing the spinal cord[84].

Despite the numerous studies that have been conducted to explore regeneration across different types of tissues, several crucial factors remain essential to the success of these regenerative endeavors. As mentioned before, the three essential components in tissue engineering are the cell type, the scaffold, and the growth factors. This ensemble is generally referred to as the tissue engineering triad. Here follows a detailed description of the functions of each of them.

When designing a tissue engineering approach, the cell type must be carefully chosen to be capable of exerting reparative functions by forming a functional matrix. The scaffold must foster an optimal environment for cells to efficiently perform their functions. The primary role of bio reactive molecules such as cytokines and growth factors is to facilitate and promote cellular regeneration, thus enabling the formation of new tissue [77,78]

In the future, an increased availability of engineered “living” tissue or organ substitutes could significantly reduce the demand for organ replacement and dramatically expedite the development of new therapeutics that can cure patients with revivable organ failure, eliminating the need for organ allotransplantation altogether.

1.3.2.1 Neural biohybrid devices

The concept of biohybrid devices is a novel paradigm that stems from the tissue engineering know-how and unites the realms of biology and engineering, giving rise to transformative solutions that transcend the capabilities of traditional device technologies. Biohybrid devices can encompass a range of constructs, from tissue-engineered organs-on-chips[70] to cellular-based bioprinting technologies[85] seeking to reduce or even eliminate the foreign body reaction and increase communication and signal transduction across biotic/abiotic interfaces. Tissue regeneration approaches can be employed not just to repair damaged tissue, but also to establish a more natural relationship between the device and the target tissue.

In the context of biohybrid device design, it is essential to distinguish between two synergic approaches, respectively bio-integration and biomimicry. The concept of bio-integration refers to the interaction between biologic materials and synthetic systems through the design and development of devices that incorporate/release bioactive components, such as proteins or living cells, into/from artificial products. The concept of biomimicry refers to the development of novel synthetic materials that draw inspiration from naturally existing features. This is typically achieved by the replication of both the microstructure and macro-functionality observed in biological materials. Frequently referenced instances include the development of solar panels that draw inspiration from the intricate structure of butterfly wings[86].

The advancements of electronics designed to interact with the neural system led to the rise of two influential approaches for restoring neurological functions: neural interfaces and cell transplantation. Both procedures aim to restore functionality by either employing electrical stimulation or recording via implantable neural interfaces, or by performing cell transplantation to replace the impaired tissue. This concept has burgeoned into a dynamic and diverse field of research, blending principles from biology, materials science, and engineering.

The overall structure of a biohybrid interface can be distinct into two different contact surfaces, namely the electrode-cell interface and the cell-tissue one. If designed properly, a biologically active intermediate layer can reduce or eliminate the issue of device degradation at the interface caused by

FBR, because the host tissue only encounters the cell interface. The efficacy of a cell-tissue interface is subordinate upon the selection of the biologically active layer, as an inappropriate choice may result in an immune response comparable to graft rejection[87,88].One additional advantageous characteristic of biohybrid implants pertains to their capacity for seamless integration with the host tissue, due to cell expansion from the implantation site to the desired anatomical structures. This enables biohybrid devices to develop connections with numerous structures, so extending their impact beyond the immediate vicinity of the implant. Several investigations have demonstrated the expansion of neuronal cultures within the implant into a damaged peripheral nerve, leading to the reinnervation of several denervated muscles [89]. The necessity for brain implants that closely emulate and seamlessly integrate with neural tissue is underscored by recent advancements in implant design[90]. Biohybrid devices have the capability to include molecular signals, such as growth factors and guiding molecules, to stimulate and direct cell growth.

The idea of symbiosis (i.e., a harmonious coexistence of biological and synthetic components) underpins the Biohybrid Device concept. This coexistence opens a plethora of possibilities, enabling the development of responsive drug delivery systems that adapt to the body's needs[91], regenerative therapies that harness the innate regenerative potential of cells[92], and biosensors capable of real-time monitoring of physiological parameters[93].

Stieglitz et al. first defined such systems and used the term "biohybrid" to address this particular class of brain implants as starting point for subsequent development in the field [89] [94]. Subsequently, Green’s group researchers studied a construct made by conductive hydrogel with platinum electrodes to support neural progenitors and glia cell growth, evaluating their electrode performance and in vitro cell viability[95]. Furthermore, Cullen et al. advanced the concept of cell-seeded probes by introducing the “living electrode” concept [96]. The development of an electrode based on neurons with outgrowing axons that can be injected into the brain and act as signal transducers between the host tissue and an external electrical or optical neuromodulation device placed on the brain's surface is described in this study. The neuronal type seeded (glutamatergic, dopaminergic, and GABAergic) determines the aim of the construct, which can have an excitatory, inhibitory, or modulatory effect, depending on the type of synapse created with the host tissue.

A further approach has been described by De Faveri et al.[97]. In their study they used a Thomas-type wire electrode coated with poli-d-lysine and human fibrin hydrogel as first layer, subsequently sheathed with a primary culture of rat hippocampal neural (neurons) and glial (astrocyte) cells., showing that cell-based electrodes represent a biohybrid solution for enhancing performance as opposed to uncoated electrode. Their approach, based on the use of a compact layer of cells within a resorbable fibrin hydrogel has been demonstrated to regulate the biological response and encourage the integration of implanted electrodes, mitigating the risk of an immune response.

This advancement opens up possibilities for utilizing various biological sources to access all materials from the recipient patient, thereby replicating the characteristics of the host tissue.

1.3.2.2 Endothelialized biomaterial

Endothelialized biomaterials (EBs) are a specific subgroup of biomedical engineering products. These original constructs combine the versatility of synthetic materials with the intrinsic properties of the vascular endothelium, offering a promising solution to challenges in regenerative medicine, tissue engineering, and implantable medical devices.

The vascular endothelium is a single layer of endothelial cells lining blood vessels that plays a pivotal role in maintaining vascular homeostasis and ensuring the proper functioning of the circulatory system[98]. It acts as a selective barrier, regulating the exchange of nutrients and gases as well as mediating inflammatory responses and hemostasis. Endothelial dysfunction is a hallmark of numerous vascular diseases, including atherosclerosis and thrombosis, underscoring the importance of preserving and restoring endothelial integrity[99].

The presence of blood vessels in the host organism is frequently influenced by the inflammatory response, which can be attributed to both the vascular damage resulting from the implantation and the host's reaction to the foreign biomaterial. The surrounding tissue undergoes remodeling in response to the host's gradual acceptance of the implant. The process of reconciliation can vary depending on the type of implant material. It may involve several mechanisms such as remodeling and integration into the host tissue, deterioration, phagocytosis, removal by leukocytes (specifically macrophages), or isolation through the creation of a fibrotic capsule. The aforementioned activities necessitate the development of novel blood arteries to sustain the metabolic demands of inflammatory cells. The blood arteries also play a role in facilitating the infiltration of leukocytes and the clearing of the implant niche from waste materials, such as debris coming either from the tissue of from the implant.

The difficulties encountered in the application of tissue engineering as a means of blood vessel replacement are considerable and arise from the peculiar features that must be exhibited by a vascular tissue. These features involve the necessary attributes of having adequate strength and elasticity to endure the cyclic strain imposed by hemodynamics, the maintenance of a compliance level that is consistent with the surrounding native vessel, and a lumen lining that exhibits non-thrombogenic features. In contrast to engineering methods employed for other tissue substitutes, tissue-engineered blood vessels (TEBVs) necessitate rapid functionality upon implantation, as opposed to relying on in vivo remodeling over time[100].

An EB profits from the regenerative potential of endothelial cells to address these vascular challenges. The used biomaterials are engineered to interact harmoniously with host tissues, promoting endothelial cell adhesion, proliferation, and the formation of a functional vascular network[101]. Their integration enables improved tissue vascularization, reducing thrombogenicity, and enhancing biocompatibility of medical implants[102]. Moreover, EBs hold promise in the development of bioartificial organs and vascular grafts, which can be customized to match the specific needs of patients[103].

The design and fabrication of vascular-like constructs are guided by principles of biomimicry and precision engineering. Advanced techniques such as microfabrication, 3D bioprinting, and other tissue engineering techniques allow the creation of biomaterials that mimic the structural and functional properties of native vascular tissues[104] enabling their customization through the inclusion of features such as microfluidic channels, porous scaffolds, and bioactive coatings to facilitate endothelialization[105].

The methodologies employed in the field of tissue engineering for blood vessels attain to four main categories: i) the construction of the three distinct layers found in a typical blood vessel (tunica intima, tunica media and tunica externa)[106]; ii) the implementation of a supportive scaffold; iii) the assessment of the engineered blood vessel in a controlled laboratory environment; iv) the transplantation and subsequent examination of the blood vessel within a living organism.

Ideally, functional TEBVs should include characteristics such as non-thrombogenicity, non-immunogenicity, compatibility with high blood flow rates, and comparable viscoelasticity to native vessels[107–109]. Furthermore, it is required that the grafts consist of viable tissues capable of eventually assimilating into the host organism and achieving a state of indistinguishability from the native vessels.

The vascular tissue engineering field employs many strategies for the deployment of vascular-like construct (Fig.4). One potential approach involves utilizing scaffolds as substrates for cell seeding, both on the surface and within the material. Alternatively, the material might serve as a platform for bioactive agonists such as growth factors, cytokine and chemokine that regulate the host response and have demonstrated significant impacts on the capacity of tissue-engineered constructions to facilitate cellular development and differentiation both in laboratory settings (*in vitro*) and within living organisms (*in vivo*). For instance, the controlled release of soluble factors can be employed to promote the infiltration of host blood vessels[105].

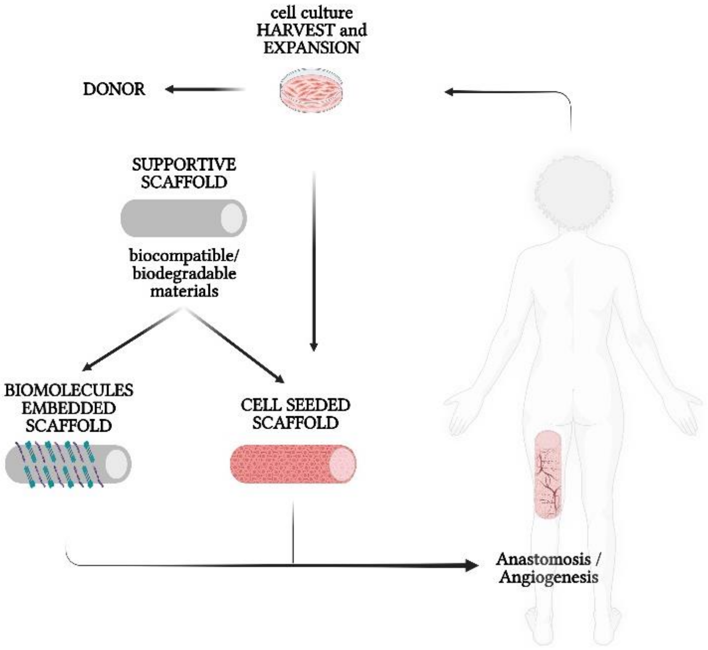

Figure 4 | vascular tissue engineering strategies. Graphical representation of strategies utilized in vascular tissue engineering field. Figure adapted from Sorrentino et., al 2011. Created with BioRender.com

Several ways for promoting endothelialization of implanted devices involve vasculogenesis, a process in which the endothelial cells (ECs) of the EB generate capillaries that then establish connections with the host's pre-existing vasculature through a process known as anastomosis. Nevertheless, a considerable number of implanted biomaterials demonstrate prompt vascularization via the process of angiogenesis, wherein new blood vessels emerge from the host's existing vasculature.

The establishment of long-lasting and effective blood vessels, nonetheless, continues to provide a significant challenge to date.

AIM AND STRUCTURE OF THE THESIS

This PhD thesis is centered on the investigation of neural devices, with a particular emphasis on two distinct but interconnected macro-areas, both of which have as their overarching objective the investigation of potential approaches to the improvement of neural device performance, integrability and stability: BIOCOMPATIBILITY and TISSUE ENGINEERING.

The relevance of the presented work is dual. On the one hand, it highlights the importance of material biocompatibility and explores novel conductive polymers that may be capable of improving electrical and functional characteristics, with a particular emphasis on how much biocompatible substrates can influence neuronal growth and targeting via topographic characterization and/or electrical cues; on the other hand, it addresses the problem of Foreign Body Reaction for intracortical electrodes by tissue engineering approach, achieving reduced inflammation via allogeneic microcirculation endothelial cell transplantation and developing novel strategies towards autologous tissue engineering in neural implants.

This conceptual duality is reflected by the chapter subdivision:

Chapters 2 and 3 are centered on in *vitro* investigations performed to assess the **biocompatibility of conductive organic materials** and their potential applications in the domain of spinal cord regeneration. In particular, they present an extensive investigation on PEDOT:Nafion biocompatibility and novel ways of guiding axon outgrowth with PEDOT:PSS coated surfaces, respectively.

Chapters 4 and 5 deal with **tissue engineering** techniques. In detail, Chapter 4 is centered on the in vivo evaluation of the benefits obtained by employing tissue engineering techniques to the reduction of inflammatory processes associated with intracortical implants, and Chapter 5 presents a new methodology of microcirculation endothelial isolation and cryopreservation from peri-tumor human fragment will be presented, with the goal of possibly facilitating future translational action. Chapters 2 to 5 report on the experimental activities and on their quantitative outcomes, while the conclusions arising from the overall experimental work are collectively discussed in Chapter 6.

Appendix 1 includes methodological details on all the experiments presented in Chapters 2-5.

BIBLIOGRAPHY

1. Fattahi, P., Yang, G., Kim, G. & Abidian, M. R. A Review of Organic and Inorganic Biomaterials for Neural Interfaces. Advanced Materials ***26****, 1846–1885 (2014).*

2. Yufik, Y. M. Brain Functional Architecture and Human Understanding. in Connectivity and Functional Specialization in the Brain (IntechOpen, 2021). doi:10.5772/intechopen.95594.

3. Kawala-Sterniuk, A. et al. Summary of over Fifty Years with Brain-Computer Interfaces—A Review. Brain Sci ***11****, 43 (2021).*

4. Peksa, J. & Mamchur, D. State-of-the-Art on Brain-Computer Interface Technology. Sensors ***23****, 6001 (2023).*

5. Hochberg, L. R. et al. Reach and grasp by people with tetraplegia using a neurally controlled robotic arm. Nature ***485****, 372–375 (2012).*

6. Krusienski, D. J. & Shih, J. J. Control of a brain–computer interface using stereotactic depth electrodes in and adjacent to the hippocampus. J. Neural Eng. ***8****, 025006 (2011).*

7. Lebedev, M. A. & Nicolelis, M. A. L. Brain–machine interfaces: past, present and future. Trends in Neurosciences ***29****, 536–546 (2006).*

8. Frey, J. et al. Past, Present, and Future of Deep Brain Stimulation: Hardware, Software, Imaging, Physiology and Novel Approaches. Front Neurol ***13****, 825178 (2022).*

9. Kim, T. H. et al. Long-Term Optical Access to an Estimated One Million Neurons in the Live Mouse Cortex. Cell Reports ***17****, 3385–3394 (2016).*

10. Tervo, D. G. R. et al. Behavioral Variability through Stochastic Choice and Its Gating by Anterior Cingulate Cortex. Cell ***159****, 21–32 (2014).*

11. Optical Deconstruction of Parkinsonian Neural Circuitry | Science. https://www.science.org/doi/full/10.1126/science.1167093.

12. Wichmann, T. & DeLong, M. R. Deep Brain Stimulation for Neurologic and Neuropsychiatric Disorders. Neuron ***52****, 197–204 (2006).*

13. McKee, C. T., Last, J. A., Russell, P. & Murphy, C. J. Indentation Versus Tensile Measurements of Young's Modulus for Soft Biological Tissues. Tissue Engineering Part B: Reviews ***17****, 155–164 (2011).*

14. Lind, G., Linsmeier, C. E., Thelin, J. & Schouenborg, J. Gelatine-embedded electrodes—a novel biocompatible vehicle allowing implantation of highly flexible microelectrodes. J. Neural Eng. 7, 046005 (2010).

15. Tien, L. W. et al. Silk as a Multifunctional Biomaterial Substrate for Reduced Glial Scarring around Brain-Penetrating Electrodes. Advanced Functional Materials ***23****, 3185–3193 (2013).*

16. Anderson, J. M., Rodriguez, A. & Chang, D. T. Foreign body reaction to biomaterials. Seminars in Immunology ***20****, 86–100 (2008).*

17. Lecomte, A. et al. Silk and PEG as means to stiffen a parylene probe for insertion in the brain: toward a double time-scale tool for local drug delivery. J. Micromech. Microeng. ***25****, 125003 (2015).*

18. Lewitus, D., Smith, K. L., Shain, W. & Kohn, J. Ultrafast resorbing polymers for use as carriers for cortical neural probes. Acta Biomaterialia 7, 2483–2491 (2011).

19. Aregueta-Robles, U. A., Woolley, A. J., Poole-Warren, L. A., Lovell, N. H. & Green, R. A. Organic electrode coatings for next-generation neural interfaces. Frontiers in Neuroengineering 7, (2014).

20. Polikov, V. S., Tresco, P. A. & Reichert, W. M. Response of brain tissue to chronically implanted neural electrodes. Journal of Neuroscience Methods ***148****, 1–18 (2005).*

21. Wang, Y., Vaddiraju, S., Gu, B., Papadimitrakopoulos, F. & Burgess, D. J. Foreign Body Reaction to Implantable Biosensors: Effects of Tissue Trauma and Implant Size. J Diabetes Sci Technol ***9****, 966–977 (2015).*

22. Lyck, R. & Engelhardt, B. Going Against the Tide – How Encephalitogenic T Cells Breach the Blood-Brain Barrier. Journal of Vascular Research ***49****, 497–509 (2012).*

23. Ballabh, P., Braun, A. & Nedergaard, M. The blood–brain barrier: an overview: Structure, regulation, and clinical implications. Neurobiology of Disease ***16****, 1–13 (2004).*

24. Fernández, E. et al. Acute human brain responses to intracortical microelectrode arrays: challenges and future prospects. Frontiers in Neuroengineering 7, (2014).

25. Karumbaiah, L. et al. Relationship between intracortical electrode design and chronic recording function. Biomaterials ***34****, 8061–8074 (2013).*

26. Vernadakis, A. GLIA-NEURON INTERCOMMUNICATIONS AND SYNAPTIC PLASTICITY. Progress in Neurobiology ***49****, 185–214 (1996).*

27. Block, M. L., Zecca, L. & Hong, J.-S. Microglia-mediated neurotoxicity: uncovering the molecular mechanisms. Nat Rev Neurosci ***8****, 57–69 (2007).*

28. Chao, C. C., Hu, S. & Peterson, P. K. Glia: The not so innocent bystanders. Journal of Neurovirology ***2****, 234–239 (1996).*

29. Leach, J., Achyuta, A. K. & Murthy, S. Bridging the divide between neuroprosthetic design, tissue engineering and neurobiology. Frontiers in Neuroengineering ***2****, (2010).*

30. Edell, D. J., Toi, V. V., McNeil, V. M. & Clark, L. D. Factors influencing the biocompatibility of insertable silicon microshafts in cerebral cortex. IEEE Transactions on Biomedical Engineering ***39****, 635–643 (1992).*

31. Röhl, C., Lucius, R. & Sievers, J. The effect of activated microglia on astrogliosis parameters in astrocyte cultures. Brain Research ***1129****, 43–52 (2007).*

32. Salatino, J. W., Ludwig, K. A., Kozai, T. D. Y. & Purcell, E. K. Glial responses to implanted electrodes in the brain. Nat Biomed Eng ***1****, 862–877 (2017).*

33. Polikov, V. S., Block, M. L., Fellous, J.-M., Hong, J.-S. & Reichert, W. M. In vitro model of glial scarring around neuroelectrodes chronically implanted in the CNS. Biomaterials ***27****, 5368–5376 (2006).*

34. Kumar, G. V. S. et al. Imaging of retained surgical items: A pictorial review including new innovations. Indian J Radiol Imaging ***27****, 354–361 (2017).*

35. Buzsáki, G. Large-scale recording of neuronal ensembles. Nat Neurosci ***7****, 446–451 (2004).*

36. Szarowski, D. H. et al. Brain responses to micro-machined silicon devices. Brain Research ***983****, 23–35 (2003).*

37. Kozai, T. D. Y., Vazquez, A. L., Weaver, C. L., Kim, S.-G. & Cui, X. T. In vivo two-photon microscopy reveals immediate microglial reaction to implantation of microelectrode through extension of processes. J. Neural Eng. ***9****, 066001 (2012).*

38. Mond, H. G., Helland, J. R., Stokes, K., Bornzin, G. A. & McVENES, R. The Electrode-Tissue Interface: The Revolutionary Role of Steroid-Elution. Pacing and Clinical Electrophysiology ***37****, 1232–1249 (2014).*

39. Zhong, Y. & Bellamkonda, R. V. Dexamethasone-coated neural probes elicit attenuated inflammatory response and neuronal loss compared to uncoated neural probes. Brain Research ***1148****, 15–27 (2007).*

40. Boehler, C. et al. Actively controlled release of Dexamethasone from neural microelectrodes in a chronic in vivo study. Biomaterials ***129****, 176–187 (2017).*

41. Takahashi, H., Wang, Y. & Grainger, D. W. Device-based local delivery of siRNA against mammalian target of rapamycin (mTOR) in a murine subcutaneous implant model to inhibit fibrous encapsulation. Journal of Controlled Release ***147****, 400–407 (2010).*

42. Malik, A. F. et al. Inflammasome components Asc and caspase-1 mediate biomaterial-induced inflammation and foreign body response. Proceedings of the National Academy of Sciences ***108****, 20095–20100 (2011).*

43. Simon, D. T., Gabrielsson, E. O., Tybrandt, K. & Berggren, M. Organic Bioelectronics: Bridging the Signaling Gap between Biology and Technology. Chem. Rev. ***116****, 13009–13041 (2016).*

44. Feron, K. et al. Organic Bioelectronics: Materials and Biocompatibility. International Journal of Molecular Sciences ***19****, 2382 (2018).*

45. Mandal, H. S. et al. Improved Poly(3,4-Ethylenedioxythiophene) (PEDOT) for Neural Stimulation. Neuromodulation: Technology at the Neural Interface ***18****, 657–663 (2015).*

46. Zheng, X. S., Tan, C., Castagnola, E. & Cui, X. T. Electrode Materials for Chronic Electrical Microstimulation. Adv Healthc Mater ***10****, e2100119 (2021).*

47. Gimsa, J. et al. Choosing electrodes for deep brain stimulation experiments–electrochemical considerations. Journal of Neuroscience Methods ***142****, 251–265 (2005).*

48. Cogan, S. F. Neural Stimulation and Recording Electrodes. Annual Review of Biomedical Engineering ***10****, 275–309 (2008).*

49. Green, R. & Abidian, M. R. Conducting Polymers for Neural Prosthetic and Neural Interface Applications. Advanced Materials ***27****, 7620–7637 (2015).*

50. Rivnay, J., Owens, R. M. & Malliaras, G. G. The Rise of Organic Bioelectronics. Chem. Mater. ***26****, 679–685 (2014).*

51. Di Lauro, M. et al. Tunable Short-Term Plasticity Response in Three-Terminal Organic Neuromorphic Devices. ACS Appl. Electron. Mater. ***2****, 1849–1854 (2020).*

*52. Bianchi, M. et al. Scaling of capacitance of PEDOT:PSS: volume vs. area. J. Mater. Chem. C **8**, 11252–11262 (2020).*

*53. Inal, S., Malliaras, G. G. & Rivnay, J. Benchmarking organic mixed conductors for transistors. Nat Commun **8**, 1767 (2017).*

*54. Stříteský, S. et al. Printing inks of electroactive polymer PEDOT:PSS: The study of biocompatibility, stability, and electrical properties. Journal of Biomedical Materials Research Part A **106**, 1121–1128 (2018).*

55. Sanchez-Sanchez, A., del Agua, I., Malliaras, G. G. & Mecerreyes, D. Chapter 6 - Conductive Poly(3,4-Ethylenedioxythiophene) (PEDOT)-Based Polymers and Their Applications in Bioelectronics. in Smart Polymers and their Applications (Second Edition) (eds. Aguilar, M. R. & San Román, J.) 191–218 (Woodhead Publishing, 2019). doi:10.1016/B978-0-08-102416-4.00006-5.

*56. Vomero, M. et al. Conformable polyimide-based μECoGs: Bringing the electrodes closer to the signal source. Biomaterials **255**, 120178 (2020).*

*57. Lipomi, D. J. et al. Electronic Properties of Transparent Conductive Films of PEDOT:PSS on Stretchable Substrates. Chem. Mater. **24**, 373–382 (2012).*

*58. Crispin, X. et al. The Origin of the High Conductivity of Poly(3,4-ethylenedioxythiophene)−Poly(styrenesulfonate) (PEDOT−PSS) Plastic Electrodes. Chem. Mater. **18**, 4354–4360 (2006).*

*59. Koutsouras, D. A. et al. Impedance Spectroscopy of Spin-Cast and Electrochemically Deposited PEDOT:PSS Films on Microfabricated Electrodes with Various Areas. ChemElectroChem **4**, 2321–2327 (2017).*

*60. Gerhardt, G. A., Oke, A. F., Nagy, G., Moghaddam, B. & Adams, R. N. Nafion-coated electrodes with high selectivity for CNS electrochemistry. Brain Research **290**, 390–395 (1984).*

*61. White, H. S., Leddy, J. & Bard, A. J. Polymer films on electrodes. 8. Investigation of charge-transport mechanisms in Nafion polymer modified electrodes. J. Am. Chem. Soc. **104**, 4811–4817 (1982).*

*62. Carli, S. et al. Electrodeposited PEDOT:Nafion Composite for Neural Recording and Stimulation. Advanced Healthcare Materials **8**, 1900765 (2019).*

*63. Carli, S. et al. Electrodeposited PEDOT:Nafion Composite for Neural Recording and Stimulation. Advanced Healthcare Materials **8**, 1900765 (2019).*

64. Carli, S. et al. Water-Based PEDOT:Nafion Dispersion for Organic Bioelectronics. ACS Appl. Mater. Interfaces ***12****, 29807–29817 (2020).*

65. Ikada, Y. Challenges in tissue engineering. J R Soc Interface ***3****, 589–601 (2006).*

66. Griffith, L. G. & Naughton, G. Tissue Engineering--Current Challenges and Expanding Opportunities. Science ***295****, 1009–1014 (2002).*

67. Green, R. et al. Living electrodes: Tissue engineering the neural interface. Conference proceedings : ... Annual International Conference of the IEEE Engineering in Medicine and Biology Society. IEEE Engineering in Medicine and Biology Society. Conference ***2013****, 6957–6960 (2013).*

68. Atala, A., Bauer, S. B., Soker, S., Yoo, J. J. & Retik, A. B. Tissue-engineered autologous bladders for patients needing cystoplasty. The Lancet ***367****, 1241–1246 (2006).*

69. Sengupta, D., Waldman, S. D. & Li, S. From In Vitro to In Situ Tissue Engineering. Ann Biomed Eng ***42****, 1537–1545 (2014).*

70. Huh, D. et al. Microfabrication of human organs-on-chips. Nat Protoc ***8****, 2135–2157 (2013).*

71. Kim, H. J., Huh, D., Hamilton, G. & Ingber, D. E. Human gut-on-a-chip inhabited by microbial flora that experiences intestinal peristalsis-like motions and flow. Lab Chip ***12****, 2165–2174 (2012).*

72. Chapekar, M. S. Tissue engineering: Challenges and opportunities. Journal of Biomedical Materials Research ***53****, 617–620 (2000).*

73. Gupta, V., Sengupta, M., Prakash, J. & Tripathy, B. C. Tissue Engineering and Artificial Organ. in Basic and Applied Aspects of Biotechnology (eds. Gupta, V., Sengupta, M., Prakash, J. & Tripathy, B. C.) 453–474 (Springer, 2017). doi:10.1007/978-981-10-0875-7_21.

74. Amer, L. D., Mahoney, M. J. & Bryant, S. J. Tissue Engineering Approaches to Cell-Based Type 1 Diabetes Therapy. Tissue Eng Part B Rev ***20****, 455–467 (2014).*

75. Fabiani, J.-N. et al. The autologous tissue cardiac valve: A new paradigm for heart valve replacement. The Annals of Thoracic Surgery ***60****, S189–S194 (1995).*

76. Huynh, T. et al. Remodeling of an acellular collagen graft into a physiologically responsive neovessel. Nat Biotechnol ***17****, 1083–1086 (1999).*

77. Wilshaw, S.-P., Kearney, J., Fisher, J. & Ingham, E. Biocompatibility and Potential of Acellular Human Amniotic Membrane to Support the Attachment and Proliferation of Allogeneic Cells. Tissue Engineering Part A ***14****, 463–472 (2008).*

78. Laurent, R., Nallet, A., Obert, L., Nicod, L. & Gindraux, F. Storage and qualification of viable intact human amniotic graft and technology transfer to a tissue bank. Cell Tissue Bank ***15****, 267–275 (2014).*

79. Uçakhan, Ö. Ö., Köklü, G. & Firat, E. Nonpreserved Human Amniotic Membrane Transplantation in Acute and Chronic Chemical Eye Injuries. Cornea ***21****, 169 (2002).*

80. Hasegawa, M., Fujisawa, H., Hayashi, Y. & Yamashita, J. Autologous amnion graft for repair of myelomeningocele: technical note and clinical implication. Journal of Clinical Neuroscience ***11****, 408–411 (2004).*

81. Gutiérrez-Moreno, S., Alsina-Gibert, M., Sampietro-Colom, L., Pedregosa-Fauste, S. & Ayala-Blanco, P. Cost-Benefit Analysis of Amniotic Membrane Transplantation for Venous Ulcers of the Legs That Are Refractory to Conventional Treatment. Actas Dermo-Sifiliográficas (English Edition) ***102****, 284–288 (2011).*

82. Loeffelbein, D. J. et al. Evaluation of Human Amniotic Membrane as a Wound Dressing for Split-Thickness Skin-Graft Donor Sites. BioMed Research International ***2014****, e572183 (2014).*

83. Borkenhagen, M., Stoll, R. C., Neuenschwander, P., Suter, U. W. & Aebischer, P. In vivo performance of a new biodegradable polyester urethane system used as a nerve guidance channel. Biomaterials ***19****, 2155–2165 (1998).*

84. Xu, X. M., Zhang, S.-X., Li, H., Aebischer, P. & Bunge, M. B. Regrowth of axons into the distal spinal cord through a Schwann-cell-seeded mini-channel implanted into hemisected adult rat spinal cord. European Journal of Neuroscience ***11****, 1723–1740 (1999).*

85. Chang, C. C., Boland, E. D., Williams, S. K. & Hoying, J. B. Direct-write bioprinting three-dimensional biohybrid systems for future regenerative therapies. Journal of Biomedical Materials Research Part B: Applied Biomaterials ***98B****, 160–170 (2011).*

86. Huang, Z. et al. Antireflective design of Si-based photovoltaics via biomimicking structures on black butterfly scales. Solar Energy ***204****, 738–747 (2020).*

87. Duncan, M. D. & Wilkes, D. S. Transplant-related Immunosuppression. Proc Am Thorac Soc ***2****, 449–455 (2005).*

88. Liu, X., Li, W., Fu, X. & Xu, Y. The Immunogenicity and Immune Tolerance of Pluripotent Stem Cell Derivatives. Frontiers in Immunology ***8****, (2017).*

89. Stieglitz, T., Ruf, H. H., Gross, M., Schuettler, M. & Meyer, J.-U. A biohybrid system to interface peripheral nerves after traumatic lesions: design of a high channel sieve electrode. Biosensors and Bioelectronics ***17****, 685–696 (2002).*

90. Yang, X. et al. Bioinspired neuron-like electronics. Nat. Mater. ***18****, 510–517 (2019).*

91. Raman, R. & Langer, R. Biohybrid Design Gets Personal: New Materials for Patient-Specific Therapy. Adv Mater ***32****, e1901969 (2020).*

92. Wu, R.-X. et al. Biomaterials for endogenous regenerative medicine: Coaxing stem cell homing and beyond. Applied Materials Today ***11****, 144–165 (2018).*

93. Jia, W. et al. Electrochemical Tattoo Biosensors for Real-Time Noninvasive Lactate Monitoring in Human Perspiration. Anal. Chem. ***85****, 6553–6560 (2013).*

94. Schwartz, A. B., Cui, X. T., Weber, D. J. & Moran, D. W. Brain-Controlled Interfaces: Movement Restoration with Neural Prosthetics. Neuron ***52****, 205–220 (2006).*

95. Goding, J. et al. A living electrode construct for incorporation of cells into bionic devices. MRS Communications 7, 487–495 (2017).

96. Serruya, M. D. et al. Engineered Axonal Tracts as "Living Electrodes" for Synaptic-Based Modulation of Neural Circuitry. Advanced Functional Materials ***28****, 1701183 (2018).*

97. De Faveri, S. et al. Bio-inspired hybrid microelectrodes: a hybrid solution to improve long-term performance of chronic intracortical implants. Frontiers in neuroengineering 7, 7 (2014).

98. Phenotypic Heterogeneity of the Endothelium | Circulation Research. https://www.ahajournals.org/doi/full/10.1161/01.RES.0000255691.76142.4a.

*99. S, X. et al. Endothelial Dysfunction in Atherosclerotic Cardiovascular Diseases and Beyond: From Mechanism to Pharmacotherapies. Pharmacological reviews 7****3****, (2021).*

100. Sorrentino, S. & Haller, H. Tissue Engineering of Blood Vessels: How to Make a Graft. in Tissue Engineering: From Lab to Clinic (eds. Pallua, N. & Suscheck, C. V.) 263–278 (Springer, 2011). doi:10.1007/978-3-642-02824-3_14.

101. Engineering Robust and Functional Vascular Networks In Vivo With Human Adult and Cord Blood–Derived Progenitor Cells | Circulation Research. https://www.ahajournals.org/doi/full/10.1161/CIRCRESAHA.108.178590.

*102. Ott, H. C. et al. Perfusion-decellularized matrix: using nature's platform to engineer a bioartificial heart. Nat Med **14**, 213–221 (2008).*

103. An engineered muscle flap for reconstruction of large soft tissue defects | PNAS. https://www.pnas.org/doi/abs/10.1073/pnas.1402679111.

*104. Zhang, Y. S. et al. Bioprinting 3D microfibrous scaffolds for engineering endothelialized myocardium and heart-on-a-chip. Biomaterials **110**, 45–59 (2016).*

*105. Khan, O. F. & Sefton, M. V. Endothelialized biomaterials for tissue engineering applications in vivo. Trends Biotechnol **29**, 379–387 (2011).*

106. Structure and Function of Blood Vessels | Anatomy and Physiology II. https://courses.lumenlearning.com/suny-ap2/chapter/structure-and-function-of-blood-vessels/.

*107. Heyligers, J. M. M., Arts, C. H. P., Verhagen, H. J. M., Groot, Ph. G. de & Moll, F. L. Improving Small-Diameter Vascular Grafts: From the Application of an Endothelial Cell Lining to the Construction of aTissue-Engineered Blood Vessel. Ann Vasc Surg **19**, 448–456 (2005).*

*108. Nerem, R. M. & Seliktar, D. Vascular Tissue Engineering. Annual Review of Biomedical Engineering **3**, 225–243 (2001).*

*109. Vara, D. S. et al. Cardiovascular tissue engineering: state of the art. Pathologie Biologie **53**, 599–612 (2005).*

2. Evaluation of the in vitro biocompatibility of PEDOT:Nafion coatings

This chapter presents a study on the biocompatibility of PEDOT:Nafion, with the aim of evaluating its potential as a viable alternative to PEDOT:PSS as conductive coating in BMIs.

This activity led to the publication of the article: “Guzzo, S. *et al.* Evaluation of the In Vitro Biocompatibility of PEDOT:Nafion Coatings. *Nanomaterials* **11**, 2022 (2021).”

Poly(3,4-ethylenedioxythiophene)-Nafion (PEDOT:Nafion) is emerging as a promising alternative to PEDOT-polystyrene sulfonate (PEDOT:PSS) in organic bioelectronics. However, the biocompatibility of PEDOT:Nafion has not been investigated to date, limiting its deployment toward in vivo applications such as neural recording and stimulation. In the present study, the in vitro cytotoxicity of PEDOT:Nafion coatings, obtained by a water-based PEDOT:Nafion formulation, was evaluated using a primary cell culture of rat fibroblasts. The surface of PEDOT:Nafion coating was characterized by Atomic Force Microscopy (AFM) and water contact angle measurements. Fibroblasts adhesion and morphology were investigated by scanning electron microscopy (SEM) and AFM measurements. Cell proliferation was assessed by fluorescence microscopy, while cell viability was quantified by 3-(4,5-Dimethylthiazol-2-yl)-2,5-Diphenyltetrazolium Bromide (MTT), lactate dehydrogenase (LDH) and neutral red assays. The results showed that PEDOT:Nafion coatings obtained by the water dispersion were not cytotoxic, making the latter a reliable alternative to PEDOT:PSS dispersion, especially in terms of chronic in vivo applications.

2.1 Surface characterization of PEDOT:Nafion Coatings

AFM images of the surface of the PEDOT:Nafion coating deposited by drop casting on glass substrate are shown in Figure 2.1. In Figure 2.1a, b, topography images of the conducting polymer coating acquired at relatively large scan size (20 x 20 and 5 x 5 μm^2) pointed out a poorly ordered and highly rough surface, typical of polymeric coatings deposited by direct casting techniques[1,2]. However, as can be observed in Figure 2.1c, on a smaller length scale, PEDOT:Nafion coating showed a nanostructured surface, featuring nanograins of the average size of ca. 30–50 nm, comparable to that of drop casted films of the most used water-based formulation of PEDOT:PSS (i.e., Clevios PH1000)[3]. It should be noted that the presence of a nanostructured surface is generally beneficial for bio-applications, as sub micrometer- and nanometer-sized features are well known to be highly effective in modulating actin cytoskeleton dynamics and cell-adhesion receptors, respectively[4,5]. Quantitative evolution of the RMS (σ) with the image scan size (L) is reported in Figure 2.1d. As previously reported for spun-coated PEDOT:PSS films[6], RMS data could be fitted with a power law fit $\sigma = \alpha L^{\beta}$, where α is the prefactor and $^{\beta}$ is the scaling exponent[7,8]. However, in this case, the absence of the horizontal upper cutoff within the investigated scan size range indicates that the casted PEDOT:Nafion coatings were highly rough, even at large length scales (i.e., >20 μm), the length scales that are of interest for single cell or cell population dynamics[4,9,10]. Finally, it can be noted that the roughness of PEDOT:Nafion coatings deposited by drop casting is much larger not only of that of PEDOT:PSS films realized by spin coating, as one may expect (only few nanometers at 15 x 15 μm^2 of scan size)[6], but also of that of electrodeposited PEDOT:Nafion coatings(ca. 70 nm at 15 x 15 μm^2 of scan size)[11].As a direct consequence of both the high surface roughness and of the hydrophobic polytetrafluoroethylene backbone featuring regularly spaced perfluorovinyl ether side chains of the Nafion polymer, the water contact angle of PEDOT:Nafion coatings resulted in being quite high (93°, see inset of Figure 2.1d), typical of a moderately hydrophobic material.

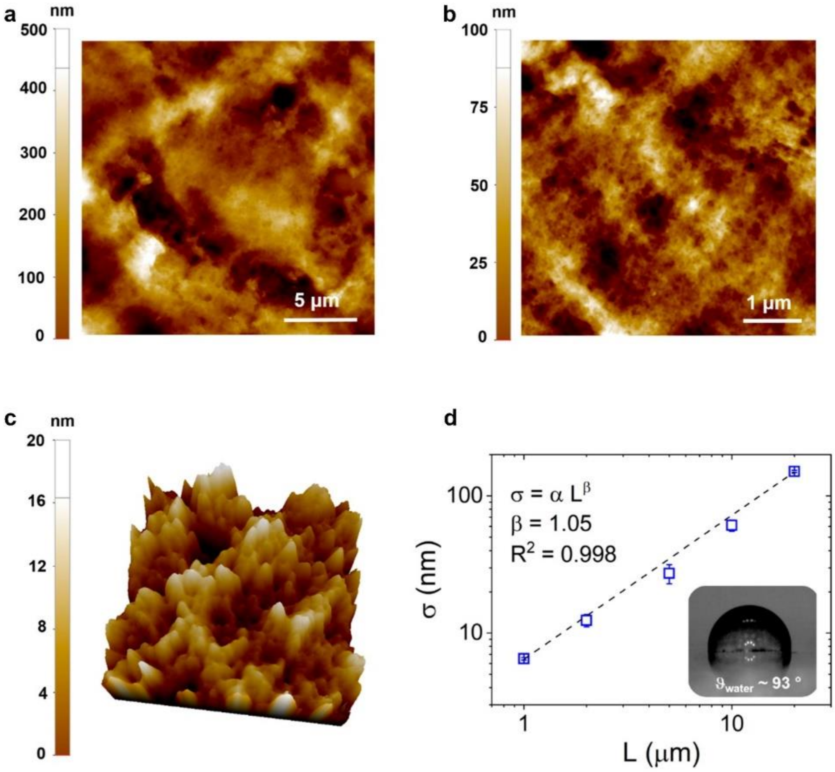

Figure 2.1 | Surface characterization of PEDOT:Nafion coatings. Two-dimensional (a,b) and three-dimensional (c) topography images of PEDOT:Nafion coatings acquired at different scale lengths. The lateral scan size is 1 μm in (c). (d) Plot of RMS (σ) vs. lateral scan size (L). The dashed dot size represents the best fit, according to the power law (σ = α Lß). Inset of (d): a representative image of a water droplet on the PEDOT:Nafion coating

2.2 Cell adhesion and proliferation on PEDOT:Nafion

The morphology of fibroblasts adhered on PEDOT:Nafion coating and on the glass control substrate at 12 h after seeding was initially evaluated by SEM analysis (Fig. 2.2). Fibroblasts adhered on the control glass showed a rounded shape, few intracellular connections and limited coverage of the substrate, indicating that, at 12 h from seeding, cells are still in an initial stage of adhesion (Figure 2.2a, b). By contrast, fibroblasts adhered on PEDOT:Nafion coating showed a flattened morphology, extended intracellular connections, full coverage of the substrate and well-developed filopodia, suggesting a more advanced stage of adhesion compared to cells on glass (Fig.2.2c,d).

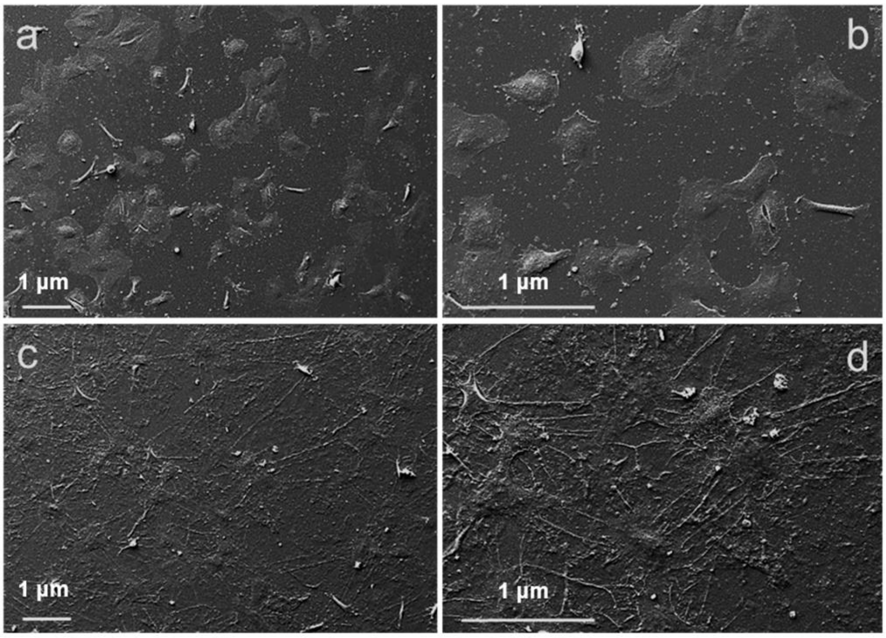

Figure 2.2 | SEM investigation of primary fibroblasts adhesion on glass control and on PEDOT:Nafion. Morphology of cells seeded on control glass (a,b) and PEDOT:Nafion coatings (c,d) at 12 h after seeding at a density of 1 x 10^4 cells/cm^2.Panels (b,d) magnified images from (a,c), respectively

Further insights regarding cell adhesion could be obtained by AFM analysis (Fig. 2.3). Interestingly, topography images pointed out the presence of the cell cortex (Fig. 2.3a), as previously reported by scanning force microscopy studies[12,13]. The cell cortex, also called actin cortex, is a thin and dense network of actomyosin under the plasma present in most mammalian cells[14]. The main role of the actin cortex is to guide cell shape changes required for cell adhesion, migration, division, and tissue morphogenesis. Therefore, an abundant presence of this structure suggests that the cell is in an active growth phase and is still adapting its morphology to the substrate[14,15]. Furthermore, AFM images of fibroblasts seeded on glass also revealed the presence of areas accumulating numerous round-shaped membranous vesicles and an underlying mat of less dense actin filament than the actin cortex (Fig. 2.3b). According to the literature, it is, therefore, possible to assume that these vesicles are zones of active production of the actin cortex[16]. Finally, yet observed by SEM analysis, adherent fibroblasts on glass were characterized by the presence of bare lamellipodia, with only initial or even absent filopodia (Fig. 2.3c). In contrast, no obvious cell cortex could be identified in the fibroblasts adhered on the PEDOT:Nafion coatings at 12 h form seeding (Fig. 2.3d,e). This observation, together the presence of well-developed filopodia compared to cells adhered on glass, suggested that cells seeded on PEDOT:Nafion were in a more advanced state of adhesion than cells on glass substrate at the selected experimental time point.

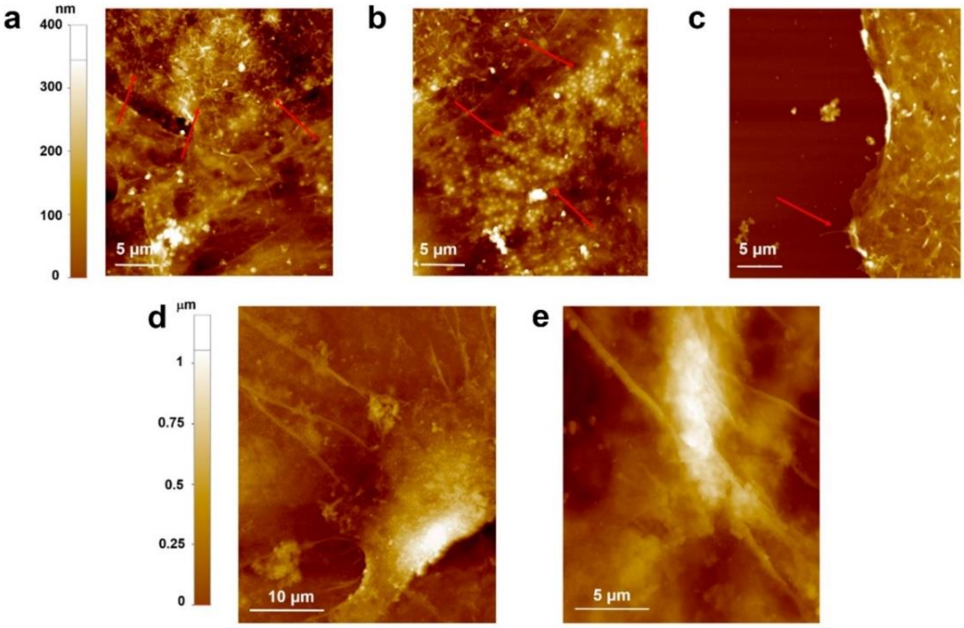

Figure 2.3 | AFM characterization of fibroblasts adhered to glass substrate and PEDOT:Nafion. AFM topography images of primary rat fibroblasts after 12 h from seeding on control glass (a–c) and PEDOT:Nafion (d,e) substrates. In (a,b), the actin filaments of the cell cortex and the round membranous vesicles (indicated by red arrows) are shown, respectively. In (c), a detail of a typical cell lamellipodium characterized only by small and rare filopodia (marked by the arrow) is shown. In (d,e), two different well-adhered fibroblasts on PEDOT:Nafion coating and showing well-developed filopodia are shown.

It is widely reported that micro/nano roughness and hydrophilicity/hydrophobicity can strongly influence cell adhesion and proliferation[7,17,18]. Indeed, coatings exhibiting a rough surface texture are expected to improve cell adhesion and spreading compared to smooth ones[19,20]. This can be attributed to the larger surface area offered by rough coatings, which promotes protein adhesion, the latter being the first event after the implantation of any material in the human body[17]. In this view, the combined large scale and nanoscale roughness showed by the PEDOT:Nafion coating strongly promoted the adhesion of the fibroblasts compared to the smooth glass substrate. Regarding surface wettability, moderate or highly hydrophilic surfaces are expected to promote cell adhesion and proliferation compared to highly hydrophobic surfaces[10,17,21]. Therefore, the rather large hydrophobicity of the PEDOT:Nafion (contact angle of ~93°), would be expected to discourage cell adhesion compared, for instance, to the moderately hydrophilic surface of the control (contact angle of ~39°, data not shown). However, this is not the case, as fibroblasts adhered more rapidly on PEDOT:Nafion coating than on the control. It can be therefore concluded that the much higher micro/nano roughness of casted PEDOT:Nafion (RMS on a 5 x 5 µm scale ~ 20 nm) compared to glass (RMS on a 5 x 5 µm scale ~ 0.2 nm)was instrumental in promoting fibroblast adhesion on the conductive polymer. The results of the proliferation assays are reported in Figure 2.4. Fluorescence images showed that fibroblasts grew rapidly on the PEDOT:Nafion coating, reaching complete confluence after 5 days (Fig. 2.4a,b), similarly to what observed for fibroblasts seeded on the control group . Quantitative proliferation data obtained from cell nuclei counting indicated no statistical differences between proliferation of cell on both experimental and control groups at the selected time points (Fig. 2.4c).

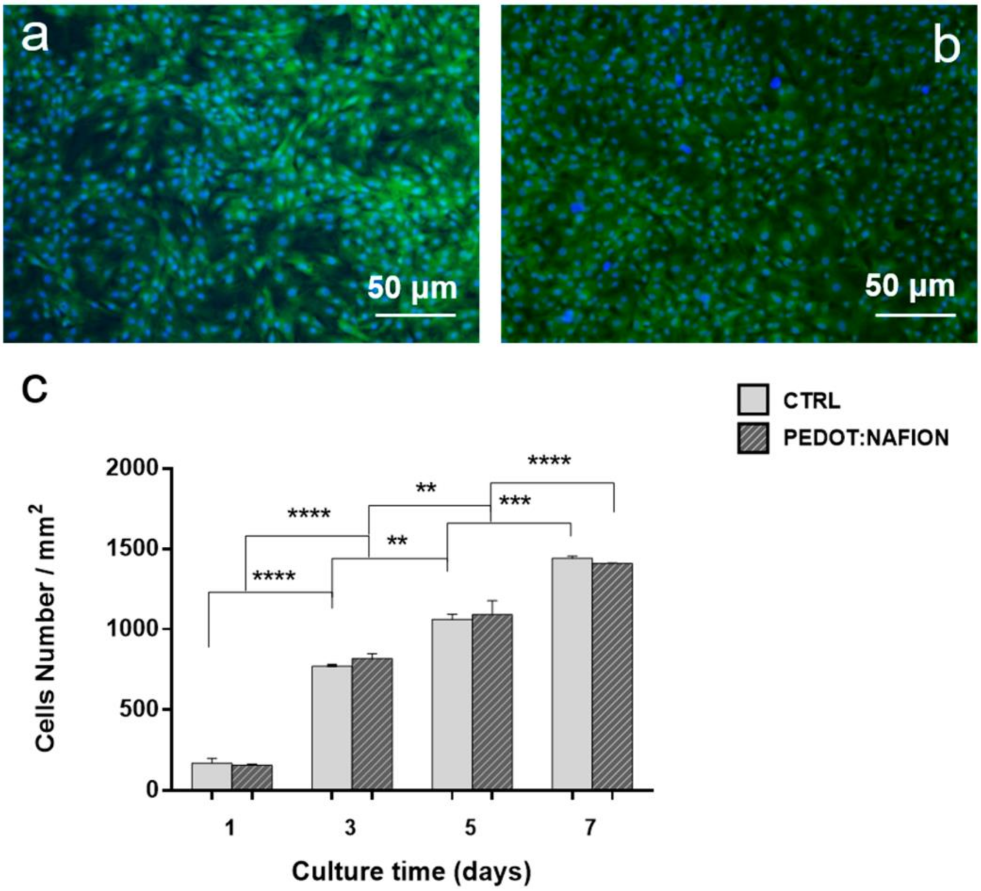

Figure 2.4 | Cells proliferation on PEDOT:Nafion. Fluorescence images of primary rat fibroblasts stained with FDA (green)and Hoechst (blue) after 5 days from seeding on glass control (a) and PEDOT:Nafion coating (b); cell density (c) at different time points ($p < 0.01$, *** $p < 0.001$, **** $p < 0.0001$).**

2.3 Evaluation of Cell Viability on PEDOT:Nafion

MTT, lactate dehydrogenase (LDH) and neutral red assays were performed at 1 and7 days in order to assess the mitochondrial redox activity, plasma membrane integrity and lysosomal activity, respectively, of fibroblasts seeded on PEDOT:Nafion coatings (Fig. 2.5). Mitochondrial redox activity was assessed by reduction of tetrazolium salt solution to formazan precipitate, which is impermeable to cell membranes and accumulates in viable cells, by mitochondrial succinate dehydrogenase in complex II[22,23]. As can be observed in Figure 2.5a, whereas cells viability was similar at day 1, cells cultured on PEDOT:Nafion showed higher viability than those proliferated on control at 7 days after seeding.

The LDH leakage test is based on the measurement of the release into the extracellular medium of the LDH enzyme (which converts lactate to pyruvate with subsequent reduction of NAD to NADH) after the disruption of the cell membrane[22,24]. The results of the assay indicated that LDH activity was similar for both the experimental and the control groups at day 1 and 7 (Fig.2.5b). In addition, LDH release increased for both groups from1 to 7, likely due to initial degradation of the plasma membrane once the cells reached the confluence phase. Cell density has been reported as a crucial factor in altering tests for cell viability, toxicity, and apoptosis[25]. At confluence, probably reached at 7 days, fibroblasts had stopped dividing due to cell crowding, shape change and growth factors depletion. Considering that 7 days is quite a long period of incubation time, cells with a rapid proliferation rate such as rat fibroblasts should be seeded at the lowest density compatible with their growth so that confluence cannot be reached before the assay endpoint. In this regard, each assay showed different sensitivity, with LDH leakage being the most sensitive in detecting detrimental effects of cell confluence at 7 days compared to the neutral red and the MTT assay, as already observed elsewhere[26]. However, similar results obtained for the PEDOT:Nafion coatings and the control substrate at each experimental time point support the conclusion that the fibroblasts are expressing normal functionality.

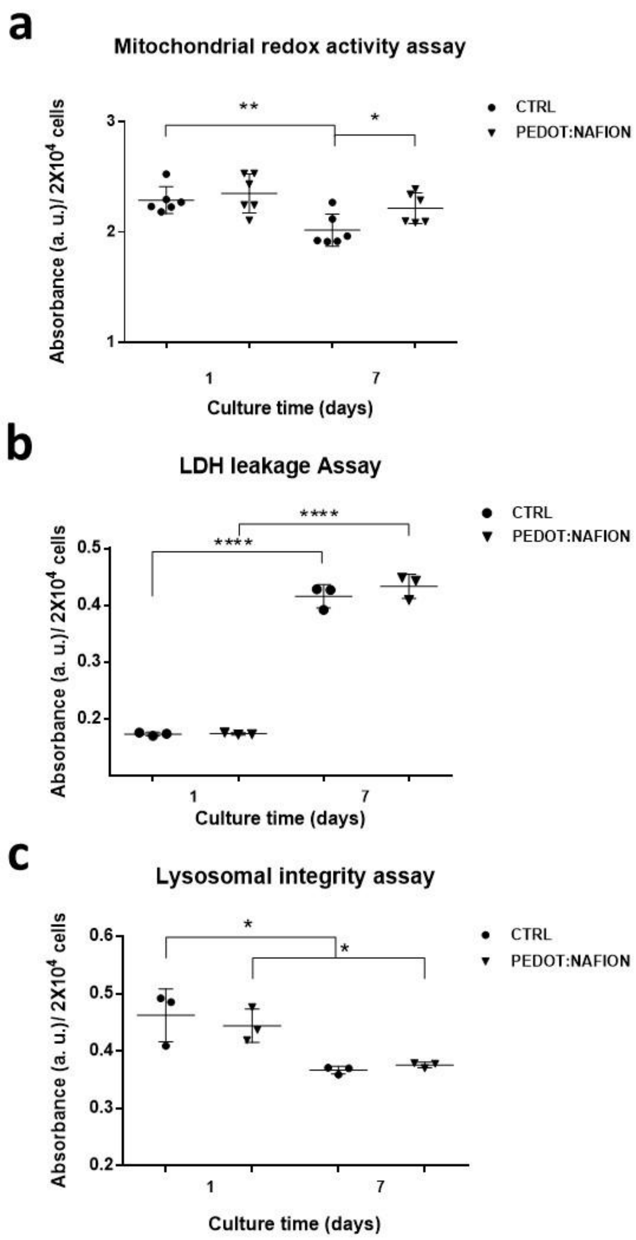

Figure 2.5 | Evaluation of fibroblasts viability on PEDOT:Nafion coating. Cytotoxicity of the PEDOT: Nafion coating was evaluated by MTT (a), LDH (b) and neutral red assay (c) at 1 day and 7 days after seeding (* $p < 0.05$, ** $p < 0.01$, **** $p < 0.0001$).

The neutral red cytotoxicity assay is a chemosensitivity test for cell viability based on the retention of a weakly cationic dye by the lysosomes of intact cells. Thus, the amount of released/retained dye is a direct marker of cell viability[27]. As can be observed in Figure 2.5c, no difference was found between the viability of fibroblasts grown on PEDOT:Nafion coatings and control substrate. Like what observed in the LDH assay, cell viability slightly decreased from 1 to 7 days, likely due to the achievement of the confluence stage. Taken together, the results of the MTT, LDH and neutral red assays indicate the PEDOT:Nafion were not cytotoxic under the investigated conditions.

BIBLIOGRAPHY

1. Li, H. et al. Preventing the coffee-ring effect and aggregate sedimentation by in situ gelation of monodisperse materials. Chemical Science ***9****, 7596–7605 (2018).*

2. Arnaud, D. et al. Fabrication of Large-scale Drop-cast Films of π-conjugated Polymers with Floating-film Transfer Method. Transactions of the Materials Research Society of Japan ***38****, 305–308 (2013).*

3. Carli, S. et al. Water-Based PEDOT:Nafion Dispersion for Organic Bioelectronics. ACS Appl. Mater. Interfaces ***12****, 29807–29817 (2020).*

4. Miyoshi, H. & Adachi, T. Topography Design Concept of a Tissue Engineering Scaffold for Controlling Cell Function and Fate Through Actin Cytoskeletal Modulation. Tissue Engineering Part B: Reviews ***20****, 609–627 (2014).*

5. Biscarini, F. et al. Unconventional Multi-Scale Patterning of Titanium Dioxide: A New Tool for the Investigation of Cell–Topography Interactions. Advanced Engineering Materials ***14****, B208–B215 (2012).*

6. Bianchi, M. et al. Scaling of capacitance of PEDOT:PSS: volume vs. area. J. Mater. Chem. C ***8****, 11252–11262 (2020).*

7. Palasantzas, G. & Krim, J. Effect of the form of the height-height correlation function on diffuse x-ray scattering from a self-affine surface. Phys. Rev. B ***48****, 2873–2877 (1993).*

8. Gambardella, A. et al. Nanostructured Ag thin films deposited by pulsed electron ablation. Applied Surface Science ***475****, 917–925 (2019).*

9. Chen, C. S., Mrksich, M., Huang, S., Whitesides, G. M. & Ingber, D. E. Geometric Control of Cell Life and Death. Science ***276****, 1425–1428 (1997).*

10. Ventre, M., Valle, F., Bianchi, M., Biscarini, F. & Netti, P. A. Cell Fluidics: Producing Cellular Streams on Micropatterned Synthetic Surfaces. Langmuir ***28****, 714–721 (2012).*

11. Carli, S. et al. Electrodeposited PEDOT:Nafion Composite for Neural Recording and Stimulation. Advanced Healthcare Materials ***8****, 1900765 (2019).*

12. Eghiaian, F., Rigato, A. & Scheuring, S. Structural, Mechanical, and Dynamical Variability of the Actin Cortex in Living Cells. Biophysical Journal ***108****, 1330–1340 (2015).*

13. Kronlage, C., Schäfer-Herte, M., Böning, D., Oberleithner, H. & Fels, J. Feeling for Filaments: Quantification of the Cortical Actin Web in Live Vascular Endothelium. Biophysical Journal ***109****, 687–698 (2015).*

14. Chugh, P. & Paluch, E. K. The actin cortex at a glance. Journal of Cell Science ***131****, jcs186254 (2018).*

15. Pegrum, S. M. & Maroudas, N. G. Early events in fibroblast adhesion to glass: An electron microscopic study. Experimental Cell Research ***96****, 416–422 (1975).*

16. Henson, J. H. et al. The ultrastructural organization of actin and myosin II filaments in the contractile ring: new support for an old model of cytokinesis. MBoC ***28****, 613–623 (2017).*

17. Cai, S. et al. Recent advance in surface modification for regulating cell adhesion and behaviors. Nanotechnology Reviews ***9****, 971–989 (2020).*

18. Bianchi, M. et al. Osteogenic Differentiation of hDPSCs on Biogenic Bone Apatite Thin Films. Stem Cells International ***2017****, e3579283 (2017).*

19. Klymov, A., Prodanov, L., Lamers, E., A Jansen, J. & Frank Walboomers, X. Understanding the role of nano-topography on the surface of a bone-implant. Biomaterials Science ***1****, 135–151 (2013).*

20. Zareidoost, A., Yousefpour, M., Ghaseme, B. & Amanzadeh, A. The relationship of surface roughness and cell response of chemical surface modification of titanium. J Mater Sci: Mater Med ***23****, 1479–1488 (2012).*

21. Valle, F. et al. Stable Non-Covalent Large Area Patterning of Inert Teflon-AF Surface: A New Approach to Multiscale Cell Guidance. Advanced Engineering Materials ***12****, B185–B191 (2010).*

22. Serrano, M. C. et al. In vitro biocompatibility assessment of poly(ε-caprolactone) films using L929 mouse fibroblasts. Biomaterials ***25****, 5603–5611 (2004).*

23. Hatefi, Y. The Mitochondrial Electron Transport and Oxidative Phosphorylation System. Annual Review of Biochemistry ***54****, 1015–1069 (1985).*

24. Liao, C., Li, Y. & Tjong, S. C. Graphene Nanomaterials: Synthesis, Biocompatibility, and Cytotoxicity. International Journal of Molecular Sciences ***19****, 3564 (2018).*

25. Metsios, A. et al. Cytotoxic and anticancer effects of the triorganotin compound [(C6H5)3Sn(cmbzt)]: An in vitro, ex vivo and in vivo study. European Journal of Pharmaceutical Sciences ***47****, 490–496 (2012).*

26. Fotakis, G. & Timbrell, J. A. In vitro cytotoxicity assays: Comparison of LDH, neutral red, MTT and protein assay in hepatoma cell lines following exposure to cadmium chloride. Toxicology Letters ***160****, 171–177 (2006).*

27. Repetto, G., del Peso, A. & Zurita, J. L. Neutral red uptake assay for the estimation of cell viability/cytotoxicity. Nat Protoc ***3****, 1125–1131 (2008).*

3. Synergy of nanotopography and electrical conductivity of PEDOT:PSS for enhanced neuronal development

This chapter presents the application of a PEDOT:PSS nanomodulated substrate, which combines both topographical and electrical stimuli, with the aim of facilitating neuronal development and promoting the sprouting of neurites.

This activity led to the publication of the article: "Bianchi, M. *et al.* Synergy of nanotopography and electrical conductivity of PEDOT:PSS for enhanced neuronal development. *ACP Applied Materials and Interfaces* ***15****, 51, 59224–59235 (2023).*

Biomaterials able to promote neuronal development and neurite outgrowth are highly desired in neural tissue engineering for the repair of damaged or disrupted neural tissue and restoring axonal connection. For this purpose, the use of either electroactive or micro- and nanostructured materials has been separately investigated. Here, the use of a nanomodulated conductive polymeric substrate, that exhibit instructive topographical and electrical cues at the same time, was investigated for the first time. In particular, poly(3,4-ethylendioxithiophene) poly(styrene sulphonate) (PEDOT:PSS) thin films (NanoPEDOT) featuring grooves with sizes comparable with those of neuronal neurites, were fabricated by electrochemical polymerization of PEDOT:PSS on a nanomodulated polycarbonate template. The ability of NanoPEDOT to support neuronal development and direct neurite outgrowth was demonstrated by assessing cell viability and proliferation, expression of neuronal markers, average neurite length and direction of neuroblastoma N2A cells induced to differentiate on this novel support. In addition to the beneficial effect of the nanogrooved topography, a 30% increase was shown in the average length of neurites when differentiating cells were subjected to an electrical stimulation of a few microamperes for six hours. The results reported here suggest a favorable effect on neuronal development of the synergistic combination of nanotopography and electrical stimulation. supporting the use of NanoPEDOT in neural tissue engineering to promote physical and functional reconnection of impaired neural networks.

3.1 NanoPEDOT substrates

Highly homogenous nanomodulated PEDOT:PSS (NanoPEDOT) substrates were obtained via the simple fabrication process sketched in Figure 3.1a. Nanomodulated PC (NanoPC) substrates featuring sub-micron nanogrooves or unmodulated PC (FlatPC) substrates were used as templates for the electrodeposition of the PEDOT:PSS layer, after the PC substrate was sputtered with a gold thin film.

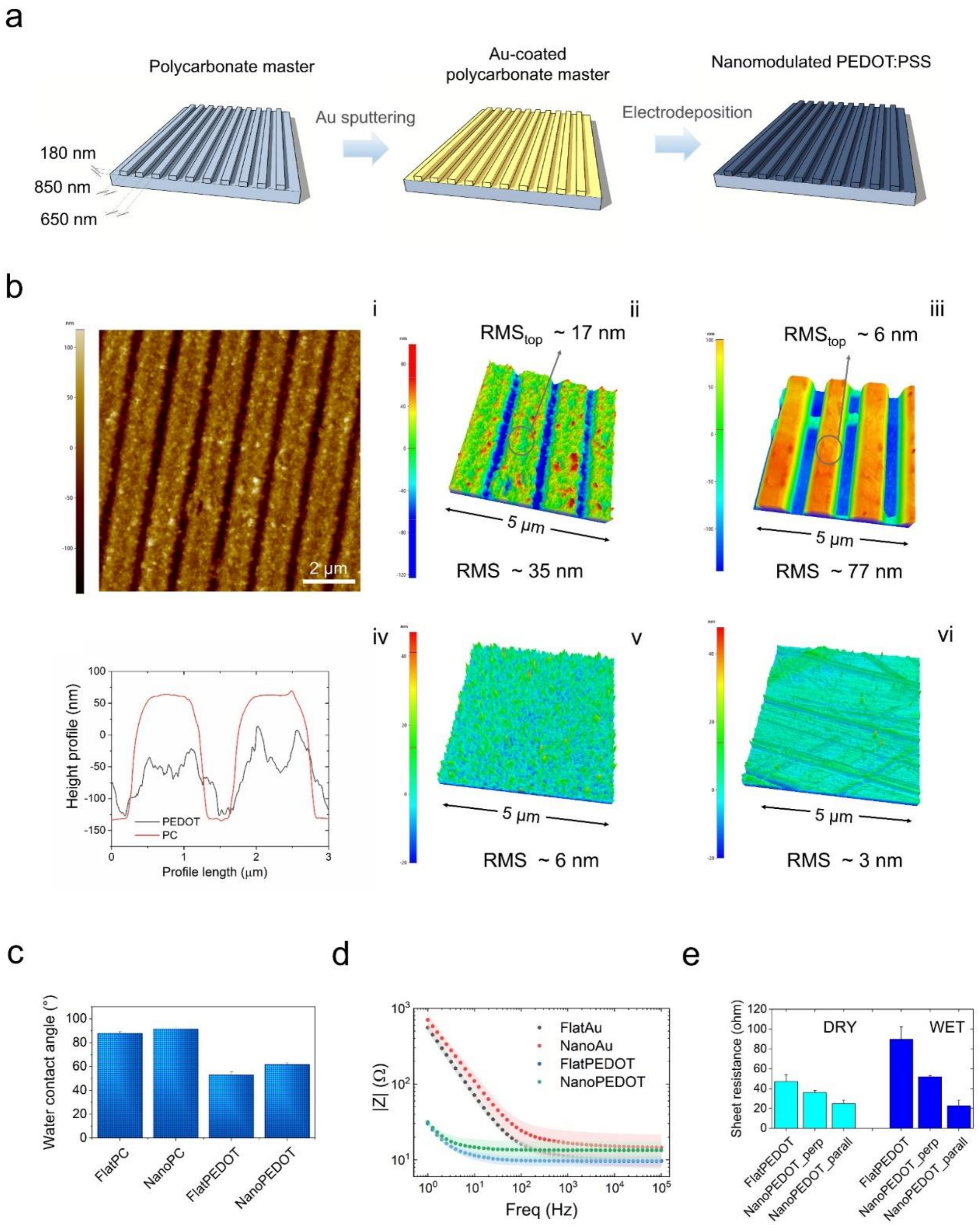

Figure 3.1 | Fabrication and characterization of the NanoPEDOT. a) Sketch of the fabrication process, encompassing metallization of a nanomodulated polycarbonate substrate and subsequent PEDOT:PSS electrodeposition. b) AFM analysis of the substrates investigated in this study: 2D topography image (i) and 3D rendering (ii) of NanoPEDOT; 3D topography of NanoPC (iii), height profiles NanoPEDOT and NanoPC (iv); 3D rendering of FlatPEDOT (v) and FlatPC (vi). c) Water contact angle and (d) EIS spectra of the investigated samples. e) Sheet resistance under dry and wet conditions of FlatPEDOT and NanoPEDOT.

We opted for the deposition of a very thin and homogenous layer of PEDOT:PSS (~ 50 nm), in order to limit the concealing of the underlying substrate topography, which is the effector instrumental for guiding cell differentiation. As local topography at micro- and nanoscale is a well-established key parameter affecting reversible and unreversible protein adhesion before and after cell attachment[1–3], surface RMS was preliminarily assessed by AFM analysis (Fig. **3.**1b). The surface of ridges in the NanoPEDOT (Fig. 3.1b_i) appeared rougher compared to that of NanoPC, being characterized by the presence of nanosized grains (lateral size 20 ÷ 50 nm), typical of electrodeposited PEDOT:PSS thin films[4,5]. Such granular morphology led to a considerable RMS increase on the top of the ridges for NanoPEDOT (RMS ~ 17 nm, Figure 3.1b_ ii) compared to NanoPC (RMS ~ 6 nm, Fig. 3.1b_ iii). However, as the conductive polymer was deposited not only on the top of the ridges but even in the patterned grooves, both an average decrease of the groove depth (from 180 nm of NanoPC to ~ 75-120 nm for NanoPEDOT) and an average increase of the ridge size (from 850 nm of NanoPC to ~ 950-1000 nm for NanoPEDOT) were observed. Overall, the deposition of the PEDOT:PSS thin layer reduced the roughness of the samples compared to that of bare nanomodulated polycarbonate, despite the former was endowed with a locally larger (nano) roughness. As expected, the unmodulated samples (FlatPEDOT and FlatPC) showed much lower RMS values, being in the order of a few nanometers (Fig. 3.1b_v-vi). Surface wettability is another surface property capable to promote or not cell adhesion on a given material[6,7]. In this study, PEDOT:PSS-coated samples (being nanomodulated or not) resulted moderately more hydrophilic than the corresponding uncoated substrates (Figure **3.**1c), likely due to the electrostatic nature of the conducting polymer which favors the adhesion and spreading of water molecule on its surface compared to the mildly polar polycarbonate surface[8]. As expected by the higher RMS values, nanomodulated surfaces (PEDOT or PC) were found to be slightly more hydrophobic than the corresponding flat samples.

3.2 Electrochemical and electrical characterization

The impedance spectra of gold-coated and PEDOT:PSS-coated polycarbonate substrates are shown in Figure 1d. The deposition of the thin PEDOT:PSS layer enabled a two-orders-of-magnitude impedance drop compared to the respective gold-coated PC substrates in the low-frequency region, with |Z| values dropping from ~ 700 ohm to ~ 30 ohm at 1 Hz. Being typical of PEDOT coatings, such a notable reduction was accompanied by a large broadening of the frequency independent region, with the cutoff frequency shifting from 10^2 ÷ 10^3 ohm to below 10 ohm, which suggests optimal charge transport between the underlying gold layer and the upper PEDOT film[8,9]. However, the similar impedance behavior for PEDOT-coated and uncoated gold substrate in the high frequency region, indicated that in this domain the resistive behavior was overshadowed by the resistance of the gold film, likely due to the very low thickness of the conductive polymer layer. Finally, no statistical differences were detected between the impedance of nanomodulated and flat substrates. Results of in-plane sheet resistance analysis obtained from four-point probe electrical measurements for NanoPEDOT and FlatPEDOT are reported in Figure **3.1e**. Sheet resistance values, in line with literature ones[10,11], were higher for FlatPEDOT than those of NanoPEDOT, both in air or under wet conditions. In particular, sheet resistance measured along the main pattern direction resulted slightly lower than the one measured perpendicular to the grooves. We speculate that the reason for these results could lie in a preferential charge transport pathway for charge carriers on the nanomodulated film (especially when current is measured along the same direction of the grooves) compared to the isotropic one. Finally, measurements carried out on samples soaked in water highlighted higher sheet resistance values for FlatPEDOT and NanoPEDOT_perp, whereas the conductivity of the NanoPEDOT_paral seemed not affected by the presence of the liquid medium.

3.3 Effect of nanomodulated PEDOT:PSS on neural cell viability and differentiation

N2A cells were induced to differentiate on NanoPEDOT and on the other investigated groups (FlatPEDOT, NanoPC and FlatPC) including a control one (petri dish). Cell viability, proliferation, and neurite outgrowth upon the presence of the PEDOT layer and/or the nanotopography were addressed (Fig. 3.2 and Fig. 3.3). The viability of N2A cells was generally increased from DIV1 to DIV6 and was maximum for cells differentiating on NanoPEDOT compared to the other groups, similarly to what observed on the control group (Figure 3.2a).

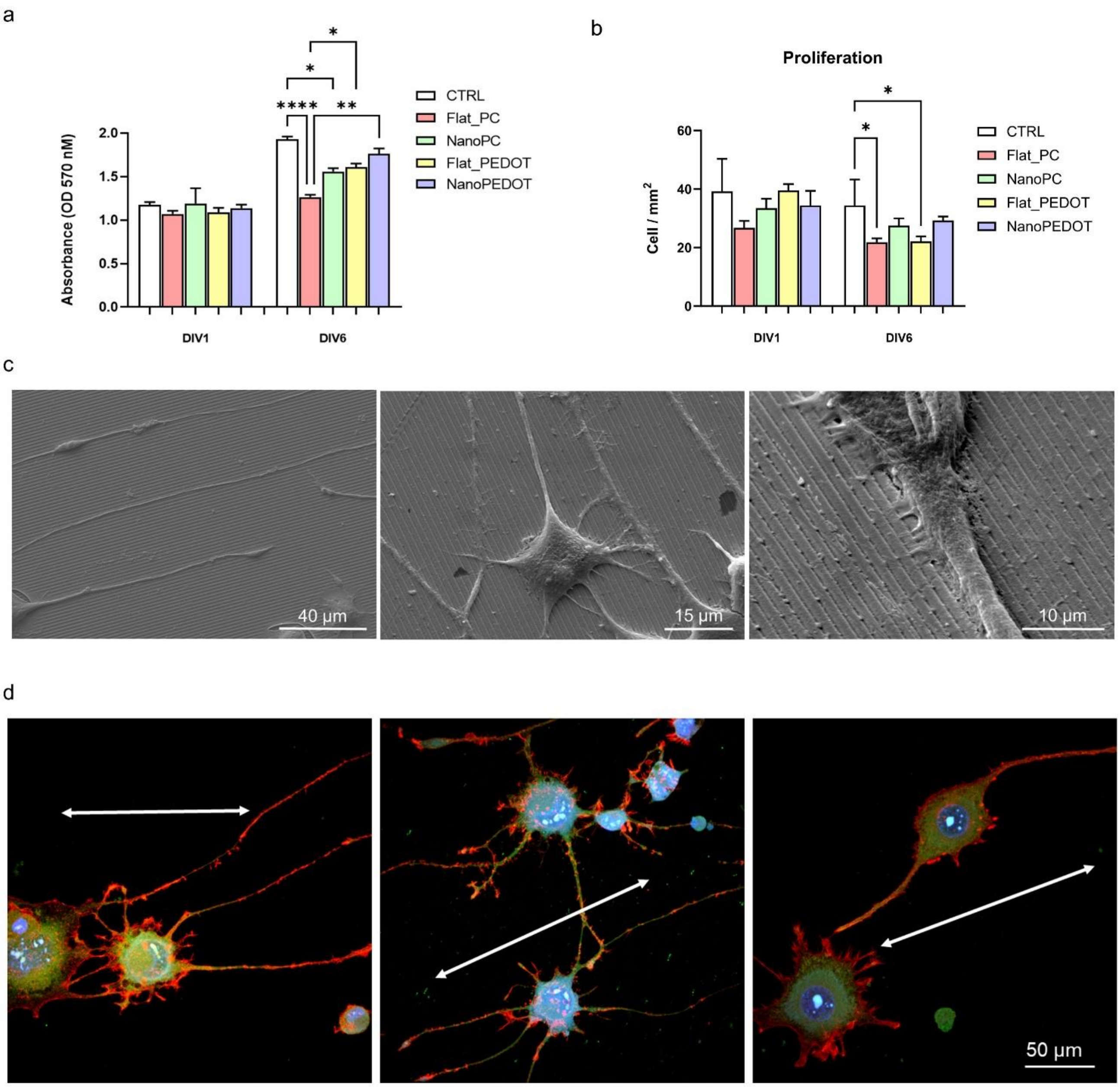

Figure 3.2 | Evaluation of N2A cell differentiation on NanoPEDOT. Results from a) MTT and b) proliferation tests. *, **, **** refer to $p < 0.05$, $p < 0.01$ and $p < 0.001$, respectively. c) Scanning electron microscopy (c) and immunofluorescence (d) images of N2A cells at DIV 6 on NanoPEDOT. In d), the following neuronal markers are shown: β-III Tubulin (green), Intracellular F-Acting (red) and Hoechst 33342 (blue); the double-ended arrows are a guide-for-the-eye to show the main direction of the pattern compared to the direction of the axons.

Slightly higher viability was steadily observed for cells differentiating on nanomodulated samples compared to flat ones, to be ascribed to the positive effect of the higher local surface roughness and area on cell behavior. Due to the intrinsic low biocompatibility of polycarbonate compared to the other investigated groups, those based on PC showed markedly lower viability. As expected, the proliferation-differentiation switchover medium causes a reduction in the trend of cell proliferation over the time (Figure 3.2b). Indeed, the proliferation-differentiation switches are caused by serum depletion combined with atRA addiction. As is common knowledge, serum contains lipoprotein and peptide growth factors that encourage cell proliferation; however, serum withdrawal results in a temporary restriction in the availability of cells. Furthermore, the typical role of atRA is to stop proliferation in order to act as a differentiation-inducing agent[12].

Representative SEM images of N2A cells differentiating on NanoPEDOT are shown in Figure 3.2c. As can be observed, the cells' axons and longest neurites grow following the main direction of the pattern, while shorter neurites and minor filopodia sprout from neurons' soma and grow along all directions, ensuring a tight anchoring to the substrate. In general, cell axons and longest neurites were found to accurately follow the longitudinal pattern, whereas shorter or minor filopodia sprouted from a neuron-like star-shaped soma to provide better cell anchoring to the substate. On the contrary, a randomly distributed outgrowth of neurites and axons was found, as expected, on unmodulated PEDOT:PSS substrate. Immunofluorescence analysis confirmed the advanced degree of differentiation of N2A cells cultured on NanoPEDOT into neurons by spotting the high expression of typical neuronal markers such as β-III Tubulin, clearly appreciable both in minor (small neurites and filopodia) and longer (axons) cell protrusions (Fig. 3.2d). More immature expression of neuronal markers was instead found at the same experimental time on cells differentiating on the other investigated samples. Average direction of cell neurites is reported in Figure 3a. Independently from the substrates surface chemistry, the presence of the pattern establishes a preferred growth direction (polarization) for neurites unlike the unmodulated surfaces. These data confirm what previously reported about the effect of nanosized grooved on neurite outgrowth direction[13,14]. However, for NanoPEDOT it can be noticed that a not negligible population of relatively short neurite is oriented almost perpendicular to the longitudinal pattern direction. Such phenomenon, termed as "neural bridge", has been already reported in literature for similar patterns[13,15] and, in this work, can be ascribed to the extensive presence of sprouting processes firmly attaching the cell to the PEDOT:PSS layer. This finding, together with the observation of a significantly larger neurite length developed by cells on NanoPEDOT compared to the other substrates and FlatPEDOT in particular (+ 25% at DIV6, Figure 3b), only confirms how much the growth and differentiation of cells is promoted on this nanostructured conductive polymeric layer. At DIV6, neurites of cells grown on NanoPEDOT were found to be ≈ 25% longer than those of cells cultured on FlatPEDOT (Figure 3.3b**)**. In contrast, no significant effect on neurite elongation was observed in cells cultured on NanoPC compared to FlatPC. Hence, it is possible to state that the nanostructured PEDOT:PSS substrate strongly promotes both the growth and the differentiation of N2A cells.

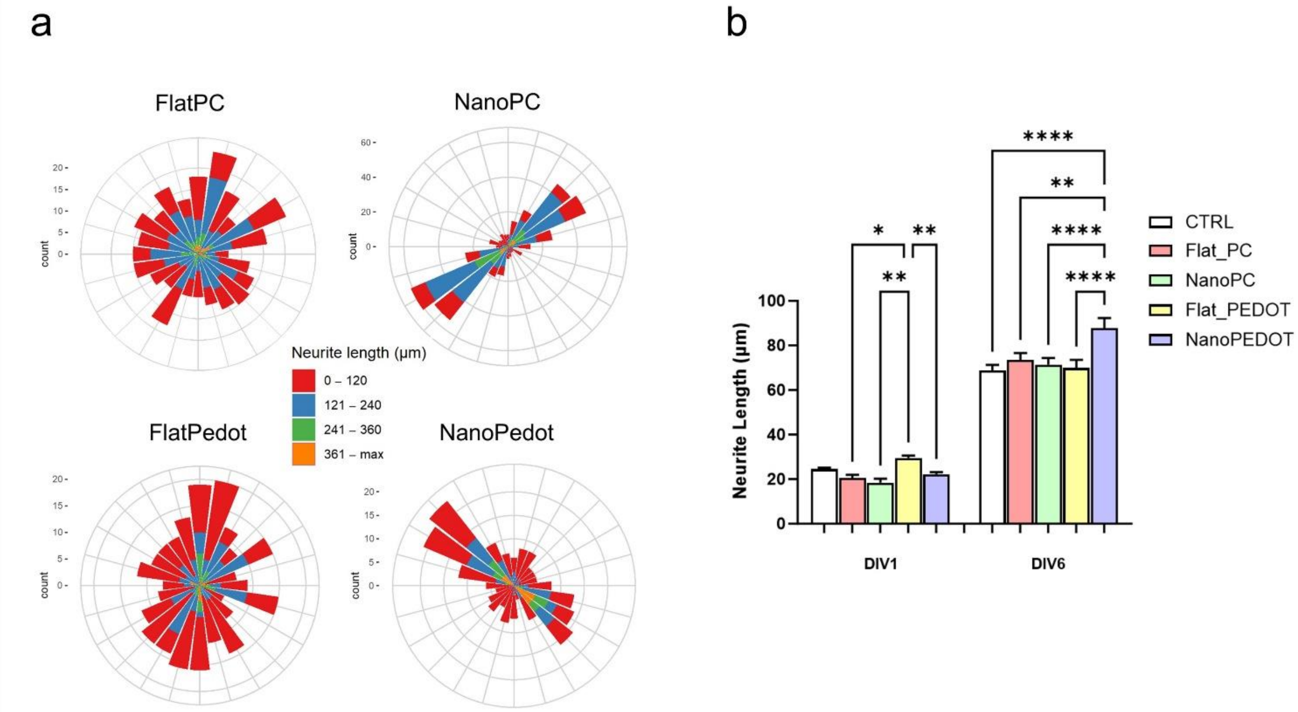

Figure 3.3 | Analysis of cell neurite polarization. a) Polar plots showing the angular distribution of neurites with respect to the main pattern direction (indicated by the dotted line) at DIV 6. Each sector corresponds to a range of 15° deg. (b) Average neurite length per cell at DIV1 and DIV6.

The optimal affinity of cells for PEDOT:PSS has been reported in a number of papers and is commonly attributed to its surface charge, rather than to its relatively rough and soft surface[16,17]. In particular, proposed models for PEDOT:PSS microstructure, encompassing the presence of larger, negatively charged, PSS shells wrapping around smaller, positively charged, PEDOT domains[18,19], well account for an overall negative surface charge of the polymer which has been postulated as fostering fast and stable accommodation of adhesion proteins and, in turn, cell spreading and colonization of the substrate[16]. Overall, our data support the hypothesis that combination of nanotopography and local nano-roughness with the particularly well suited surface chemistry of PEDOT:PSS, synergistically cooperate into promoting neuronal polarization and accelerating neurite development, especially if compared to unmodulated PEDOT:PSS (FlatPEDOT) or uncharged nanomodulated (NanoPC) substrates.

3.4 AFM analysis of neurites

AFM is an invaluable tool in biophysics to simultaneously get qualitative and quantitative topographical information compared to optical or electronic microscopy at the micro- and nanoscale[20,21]. Here, we investigated by AFM the characteristic dimensions of sprouted neurites and their intimate interaction with the nanotopography of the conductive substrate (Figure 3.4). We investigated cells at an advanced differentiation stage (DIV 6) in order to be sure to identify developed axons (as observed from optical and scanning electron microscopy), other than minor neurites (i.e., dendrites). We excluded from this analysis the extremely short processes close to the cell soma. By focusing on sample areas showing several protrusions from different cells such as the one reported in Figure 3.4a, we were able to spot the presence of a distinct population of relatively large processes with later size of (1.3 ± 1) µm (Figure 3.4b_i-ii). Being the latter the larger size found in the sample, in good agreement with previous optical and AFM investigations[22–24], it was quite easy to assign this population to that of mature axons. This fact hints that geometrical matching between axonal diameter and pitch dimension (≈ 1.5 µm) played a pivotal role into directing neurite growth on this kind of pattern. Average size of smaller neurites was instead found to fall under a broader distribution curve ranging approximately from 0.7 µm to 1.1 µm (Figure 3.4c). We assigned this more heterogeneous population to both dendrites and immature axons, being at this stage impossible to distinguish between the two.

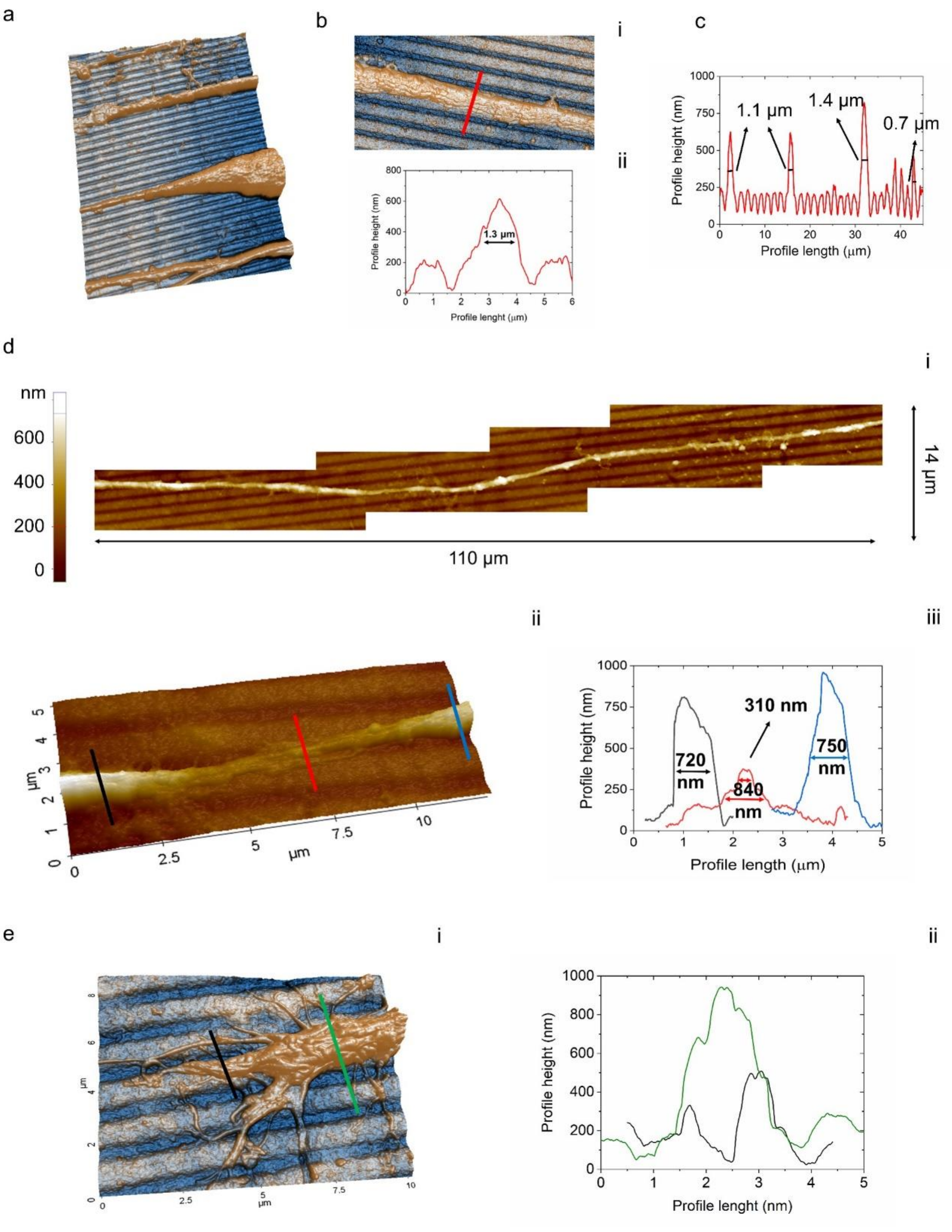

Figure 3.4 | AFM analysis of neurite morphology on NanoPEDOT (DIV6). a) (45 µm x 30 µm) 3D topography image of parallel neurites from different cells. b) (20 µm x 10 µm) topography image (i) and height profile (ii) of a portion of axon. c) line profile from a), showing the presence of both axonal and smaller neurite processes. d) combination of four different AFM scans (i) enabling to follow one single neurite up to more than 100 mm of length; (ii) detail from (i) showing the squeezing of the neurite inside the nanogroove and (iii) relative height profiles. e) 3D rendering (i) and relative height profiles (ii) of a growth cone.

Interestingly, AFM analysis allowed us also to spot a quite uncommon behavior of cell protrusions such as the one shown in Figure 3.4d. Here, the topography of an average size neurite, acquired by moving the scan area along the direction of the neurite for a total length of 110 µm and stitching the AFM images together, is shown (Figure 3.4d_i). As it can be appreciated, the neurite follows the direction of the grooves quite conformally even though its diameter (≈ 0.75 µm) does not match the size of the ridge (1.0 ÷ 1.1 µm) or the groove (0.4 ÷ 0.5 µm). Even more interestingly, the neurite was found to squeeze(deform) in several places in the scanned area to be able to allocate itself within the depth of the groove (Figure 3.4d_ii-iii). Taken together, AFM data corroborate the high suitability of the selected pattern dimensions for the alignment and direction of both axonal and smaller neurites.

3.5 Analysis of growth cones on NanoPEDOT

Growth cones can be found on the distal part of a growing neurite; they are structures that continuously change their morphology for the purpose of probing the surroundings and determining the direction of growth of the neurite which, in the absence of instructional cues, proceed along a relatively straight path[25]. Growth cone direction hence relies on tireless synthesis and disruption of actin filaments that constitute the major portion of the filopodia, the latter being continuously expanded and retracted.. Remarkably, the growth of the cone does not just proceed along the main direction guided by the nanotopography, as one may expect. It is instead the result of a sort of "trial and error" process, aimed to span around the surrounding environment on a ≥180° spectrum. The fact that the axon keeps on growing on the main pattern direction rather than jumping from one lane to another or even changing direction can be ascribed to the establishment of privileged tensional forces between the cell and the nanogrooved substrate along the main pattern direction, as previously reported for other nanomodulated/nanopatterned systems[26–28]. The presence of a chemical gradients can be speculated to lead to the decision to make a neurite abandon the main direction pattern, cross the nanogrooves and create a synaptic connection with the nearby neurite from another cell. Along with axons, dendrites, soma and synapses, also growth cones have been subject of investigation with AFM, even if the literature in this field is still at this infancy[24,29–31]. A 3D AFM image of a growth cone of an axon developing along the NanoPEDOT is shown in Figure 4e_i together with some profiles tracked on different areas of the cone (Figure 3.4e_ii). AFM analysis allowed to spot several small diameter (200 ÷ 300 nm) filopodia appointed to span the surroundings and search for the preferred way to further trigger the axonal growth. The fact that the larger cone terminal bundle (~ 600 nm of diameter) is on the top of the ridge and in the frontal part of the cone, together with the presence of bundles of microtubules infiltrating the growth cone (typical of an active cone[31]) leads us to postulate that the axon investigated in this image will likely keep on growing along that direction during the subsequent growth phase.

3.6 Evaluation of neurite length upon electrical stimulation

To evaluate the advantage of handling a tailored nanomodulated surface and the possibility to electrically stimulate neural cells at the same time, we applied the stimulation protocol showed in Figure 3.5a to N2A cells cultured on both NanoPEDOT and FlatPEDOT. Cells underwent static mild electrical stimulation (≈ 15 μA) for a short period of time (6h) during their differentiation process. At the end of the stimulation period, cells were let to further differentiate for additional 18h. Notably, we found a remarkable +33% increase of the average neurite length for cell differentiating on NanoPEDOT when cells were electrically stimulated compared to non-stimulated ones, supporting the hypothesis of beneficial effects of stimulation on neuronal polarization, as previously demonstrated by others using different substrate materials or cell types[,33]. Even more interestingly, under stimulation, cells were found to sprout significantly longer (+24%) neurites when cultured on NanoPEDOT than on FlatPEDOT, clearly underlying the beneficial effect of the coupled approach (i.e., nanotopography and electrical stimulation).

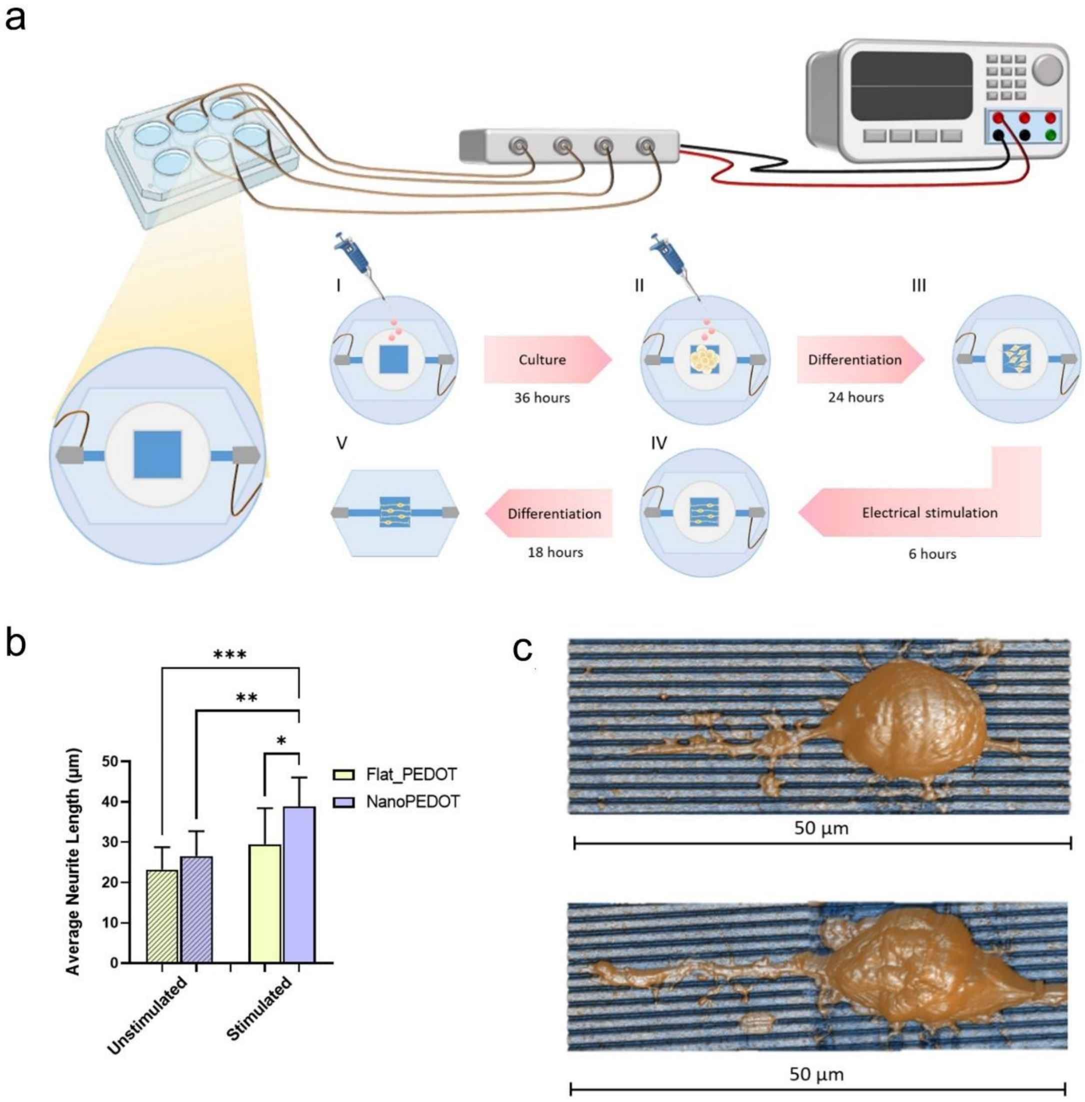

Figure 3.5 | Electrical stimulation of neural cells on nanoPEDOT. a) Sketch of the setup used for the electrical stimulation experiment. b) Average neurite length of N2A differentiating on NanoPEDOT and FlatPEDOT with and without electrical stimulation. c) Representative AFM image of neurites sprouted from stimulated (top) and non-stimulated (bottom) N2A cells on NanoPEDOT.

Finally, it should be noted that data concerning neurite length obtained from the stimulation experiments cannot be directly overlapped with those shown in Figure 3.3, mainly due to different protocol used (especially regarding the different experimental time at which neurite length was evaluated). However, it can be inferred, without fear of falling into overly speculative deductions, that coupling the effect of nanomodulation with that of electrical stimulation leads to net increase in average neurite length compared with the two decoupled single approaches. Thus, we conclude that the effects, viz. nanopatterned grooves and electrical stimulation act synergically to produce a larger elongation of aligned neurites on the surface, with formation of synaptic contacts and enhanced spreading of the soma of the neuronal cells.

1. Hallab, N. J., Bundy, K. J., O'Connor, K., Clark, R. & Moses, R. L. Cell adhesion to biomaterials: correlations between surface charge, surface roughness, adsorbed protein, and cell morphology. J Long Term Eff Med Implants ***5****, 209–231 (1995).*

2. Ventre, M., Valle, F., Bianchi, M., Biscarini, F. & Netti, P. A. Cell Fluidics: Producing Cellular Streams on Micropatterned Synthetic Surfaces. Langmuir ***28****, 714–721 (2012).*

3. Boi, M. et al. Tough and adhesive nanostructured calcium phosphate thin films deposited by the pulsed plasma deposition method. RSC Adv. ***5****, 78561–78571 (2015).*

4. Carli, S. et al. Multifunctionally-doped PEDOT for organic electrochemical transistors. Frontiers in Materials ***9****, (2022).*

5. Guzzo, S. et al. Evaluation of the In Vitro Biocompatibility of PEDOT:Nafion Coatings. Nanomaterials ***11****, 2022 (2021).*

6. Valle, F. et al. Stable Non-Covalent Large Area Patterning of Inert Teflon-AF Surface: A New Approach to Multiscale Cell Guidance. Advanced Engineering Materials ***12****, B185–B191 (2010).*

7. Tian, Y., Yan, S., Song, C., Wang, C. & Chen, J. Research on the influence of Micro-morphology on the hydrophobicity of material surface. Colloid and Interface Science Communications ***46****, 100556 (2022).*

8. Lu, B. et al. Pure PEDOT:PSS hydrogels. Nat Commun ***10****, 1043 (2019).*

9. Kayinamura, Y. P., Ovadia, M., Zavitz, D. & Rubinson, J. F. Investigation of Near Ohmic Behavior for Poly(3,4-ethylenedioxythiophene): A Model Consistent with Systematic Variations in Polymerization Conditions. ACS Appl. Mater. Interfaces ***2****, 2653–2662 (2010).*

10. Kim, Y., Yoo, S. & Kim, J.-H. Water-Based Highly Stretchable PEDOT:PSS/Nonionic WPU Transparent Electrode. Polymers ***14****, 949 (2022).*

11. Kim, S., Kim, S. Y., Chung, M. H., Kim, J. & Kim, J. H. A one-step roll-to-roll process of stable AgNW/PEDOT:PSS solution using imidazole as a mild base for highly conductive and transparent films: optimizations and mechanisms. J. Mater. Chem. C ***3****, 5859–5868 (2015).*

12. Janesick, A., Wu, S. C. & Blumberg, B. Retinoic acid signaling and neuronal differentiation. Cell. Mol. Life Sci. ***72****, 1559–1576 (2015).*

13. Simitzi, C., Ranella, A. & Stratakis, E. Controlling the morphology and outgrowth of nerve and neuroglial cells: The effect of surface topography. Acta Biomaterialia ***51****, 21–52 (2017).*

14. Marcus, M. et al. Interactions of Neurons with Physical Environments. Advanced Healthcare Materials ***6****, 1700267 (2017).*

15. Goldner, J. S., Bruder, J. M., Li, G., Gazzola, D. & Hoffman-Kim, D. Neurite bridging across micropatterned grooves. Biomaterials ***27****, 460–472 (2006).*

16. Sordini, L. et al. Effect of Electrical Stimulation Conditions on Neural Stem Cells Differentiation on Cross-Linked PEDOT:PSS Films. Frontiers in Bioengineering and Biotechnology ***9****, (2021).*

17. Serafin, A. et al. Electroconductive PEDOT nanoparticle integrated scaffolds for spinal cord tissue repair. Biomater Res ***26****, 63 (2022).*

18. Gueye, M. N., Carella, A., Faure-Vincent, J., Demadrille, R. & Simonato, J.-P. Progress in understanding structure and transport properties of PEDOT-based materials: A critical review. Progress in Materials Science ***108****, 100616 (2020).*

19. Posudievsky, O. Yu., Konoshchuk, N. V., Shkavro, A. G., Koshechko, V. G. & Pokhodenko, V. D. Structure and electronic properties of poly(3,4-ethylenedioxythiophene) poly(styrene sulfonate) prepared under ultrasonic irradiation. Synthetic Metals ***195****, 335–339 (2014).*

20. Alessandrini, A. & Facci, P. AFM: a versatile tool in biophysics. Meas. Sci. Technol. ***16****, R65 (2005).*

21. Tonazzini, I. et al. Multiscale Morphology of Organic Semiconductor Thin Films Controls the Adhesion and Viability of Human Neural Cells. Biophysical Journal ***98****, 2804–2812 (2010).*

22. Ungureanu, A.-A. et al. Amyloid beta oligomers induce neuronal elasticity changes in age-dependent manner: a force spectroscopy study on living hippocampal neurons. Sci Rep ***6****, 25841 (2016).*

23. Sun, L. et al. The Nanoscale Observation of the Three-Dimensional Structures of Neurosynapses, Membranous Conjunctions Between Cultured Hippocampal Neurons and Their Significance in the Development of Epilepsy. Mol Neurobiol ***53****, 7137–7157 (2016).*

24. Laishram, J. et al. A morphological analysis of growth cones of DRG neurons combining Atomic Force and Confocal Microscopy. Journal of Structural Biology ***168****, 366–377 (2009).*

25. Anava, S., Greenbaum, A., Jacob, E. B., Hanein, Y. & Ayali, A. The Regulative Role of Neurite Mechanical Tension in Network Development. Biophysical Journal **96**, 1661–1670 (2009).

26. Rape, A. D., Guo, W. & Wang, Y. The regulation of traction force in relation to cell shape and focal adhesions. Biomaterials **32**, 2043–2051 (2011).

27. Kim, K. A., Vellampatti, S. & Kim, B. C. Characterization of Integrin Molecular Tension of Human Breast Cancer Cells on Anisotropic Nanopatterns. Frontiers in Molecular Biosciences **9**, (2022).

28. Geiger, B., Spatz, J. P. & Bershadsky, A. D. Environmental sensing through focal adhesions. Nat Rev Mol Cell Biol **10**, 21–33 (2009).

29. Grzywa, E. L., Lee, A. C., Lee, G. U. & Suter, D. M. High-resolution analysis of neuronal growth cone morphology by comparative atomic force and optical microscopy. Journal of Neurobiology **66**, 1529–1543 (2006).

30. Yunxu, S., Danying, L., Yanfang, R., Dong, H. & Wanyun, M. Three-dimensional structural changes in living hippocampal neurons imaged using magnetic AC mode atomic force microscopy. Journal of Electron Microscopy **55**, 165–172 (2006).

31. Xiong, Y., Lee, A. C., Suter, D. M. & Lee, G. U. Topography and Nanomechanics of Live Neuronal Growth Cones Analyzed by Atomic Force Microscopy. Biophysical Journal **96**, 5060–5072 (2009).

32. Electrical stimulation alters protein adsorption and nerve cell interactions with electrically conducting biomaterials**期刊界** All Journals **搜尽天下**杂志 传播学术成果 专业期刊搜索 **期刊信息化** 学术搜索. http://cnjournals.com/view_abstract.aspx?aid=EB8EC62E1421F4BE95B7A5FFA0EB9140&jid=7D8485F5338640D563B554D7DC0D3E60&pcid=A9DB1C13C87CE289EA38239A9433C9DC&yid=14E7EF987E4155E6.

33. Pires, F., Ferreira, Q., Rodrigues, C. A. V., Morgado, J. & Ferreira, F. C. Neural stem cell differentiation by electrical stimulation using a cross-linked PEDOT substrate: Expanding the use of biocompatible conjugated conductive polymers for neural tissue engineering. Biochimica et Biophysica Acta (BBA) - General Subjects **1850**, 1158–1168 (2015).

4. Brain Microvascular endothelial cells as coating for deep-brain electrodes: a “Biohybrid device” to minimize Foreign Body Reaction

This chapter presents a preliminary investigation using allogenic cerebral microvascular endothelial cells to coat an intracortical device, with the aim of evaluating the foreign body reaction by means of histological assessments within a two-week period after implantation.

In the field of tissue engineering of neural devices, a vast majority of design strategies involve the use of neuronal and non-neuronal cells, specifically microglia and astrocytes. In contrast, in this work we employed primary endothelial cells derived from allogenic brain microvasculature of rats. The aim is achieving electrode encapsulation by means of a vessel-like arrangement, in order "disguise" the microwire-electrode as a microcapillary, thus reducing the resulting Foreign Body Reaction.

As introduced in Chapter 1, brain microvascular endothelial cells (BMECs) are responsible for the formation of monolayers that play a crucial role in the functioning of the blood-brain-barrier (BBB). These BMECs, along with pericytes, smooth muscle cells, astrocytic end feet, and circulating blood cells, collectively form the neurovascular unit (NVU)[1]. NVU serves as a crucial interface that governs the regulated and precise exchange of fluids, chemicals, and cells between the cerebral blood vessels and the central nervous system (CNS)[2]. A disruption or impairment of NVU has the potential to initiate and/or exacerbate a range of disorders affecting the CNS, including ischemic stroke, HIV encephalopathy, multiple sclerosis, Alzheimer's disease, and Parkinson's disease[3,4]. For these reasons, the neural tissue exhibits a significant degree of vascularity, and the objective of this bio-hybrid approach is to emulate such physiological features of the host tissue, by creating a durable vascular-like layer on prosthetic devices. The purpose of this coating is to preserve vascular hemostasis, reduce thrombogenicity, and enhance the biocompatibility of the implant.

The aforementioned methodology exhibits potential as a viable alternative for reducing foreign body response (FBR), addressing the limitations linked to intracortical implants, and establishing a novel trajectory in the progression of biomimetic neuroprosthetics with enhanced biological integration. The following preliminary investigation hints at the validity of this approach, both in terms of cell adhesion to the implant and of foreign body reaction.

4.1 brain microvascular endothelial cells harvesting and device coating

As a result of the isolation process detailed in Appendix 1, rat brain microvascular endothelial cells (BMECs) and accompanying cells aggregate together, creating conglomerates that are suspended in the cell culture medium (see Figure 4.1a, day 0). The administration of puromycin results in the preferential enrichment of BMECs due to their heightened expression of efflux transporters, mainly P-glycoprotein. Consequently, this enhanced expression endows BMECs in the culture with a relative resistance to toxic substances. In contrast, other cells are significantly more prone to experiencing cytotoxicity induced by puromycin[5]. During the puromycin selection process, it is observed that contaminating cells undergo apoptotic death, whereas BMECs initiate attachment to the cell culture plates covered with collagen IV and fibronectin. By the fifth day, the proliferation reaches a density of approximately 60 - 70%.

The cells exhibit a distinctive morphology defined by a spindle-shaped semblance arranging themselves into a monolayer characterized by dense packing, longitudinal alignment, and non-overlapping contact inhibition (Figure 4.1b, day 5) establishing highly impermeable monolayers that are coupled by the presence of tight junction proteins. Through the implementation of puromycin selection, a remarkable level of purity, reaching up to 99%, is achieved for BMECs.

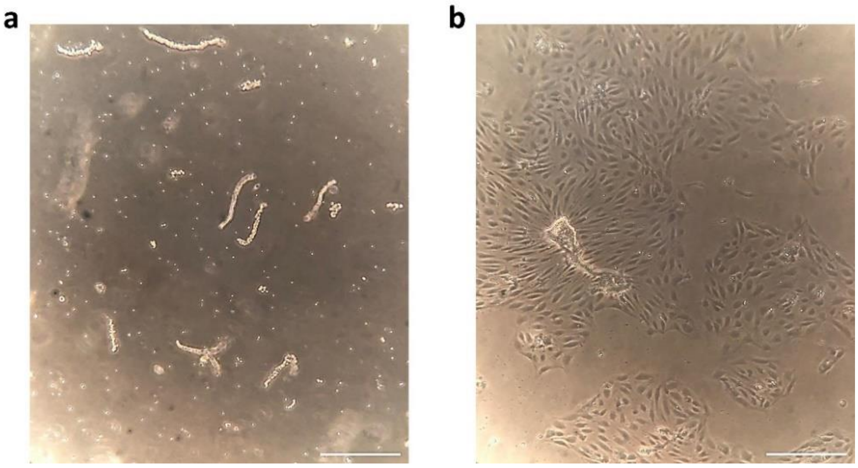

Figure.4.1 | Morphological representation of rat BMECs. (a) Day 0 of isolated rBMECs . (b) Day 5 of isolated rBMECs after culture purification with puromycin. 200 µm scale bar applied.

4.2 Device cell adhesion evaluation

Intracortical devices have been coated by BMECs using a dip coating technique, detailed in Appendix 1. Such technique has been chosen for its versatility, in order to be suitable for various device shapes. In particular, two family of probes have been tissue-engineered with BMECS: namely, the Neuronexus A-style probe (Figure 4.2a, characterized by a planar shape, from https://www.neuronexus.com/products/electrodearrays) and the Thomas type wire electrode (Fig.4.2b, distinguished by its cylindrical shape, from https://www.thomasrecording.com/single-electrodes-for-thomas-manipulators). Both electrode types were coated and subsequently assessed for cellular adhesion. A mold consisting of a mixture of 0.6 percent agarose and PBS, called "brain phantom", was used to mimic the mechanical properties of the brain. [6]. This model was utilized to recreate the process of implantation and assess the detachment of cells upon mechanical stress. This evaluation was performed by coating the device with live fluorescent staining Calcein AM and propidium iodide (PI) to verify, at the same time, the viability of adherent cells.

In particular, calcein AM staining has been used because a disparity in fluorescence intensity between the device pre-insertion and the device post insertion would indicate significant detachment of living cells. (Fig.4.2c, d, e). The results indicate a non-statistically significant difference in fluorescence upon the insertion/extraction process (Fig.4.2c) and total absence of PI-positive cells (non-vital ones), suggesting that, after implantation, the cells surrounding the device remain adherent and vital, despite the contrast force exerted by the brain against the pressure of the implant (buckling force, introduced in chapter 1). The absence of PI-positive cells demonstrates also that the timing of cell culture and the selected probe-coating methodology are suitable for proper cell proliferation.

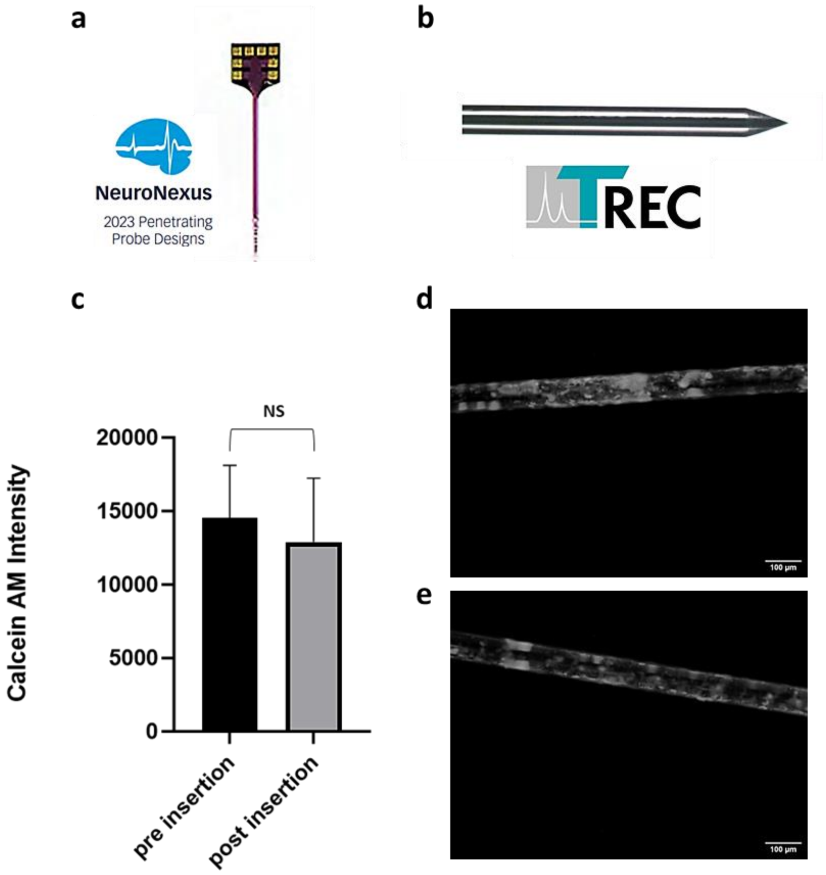

Figure 4.2 | Intracortical device type and delamination evaluation. (a) planar shape Neuronexus A-style probe. (b) cylindrical shape Thomas type wire probe. (c) Histogram showing non-significant difference in Calcein AM intensity between "pre insertion" and "post insertion" conditions (d-e) Exemplary rBMECs-coated Thomas-type wire stained with Calcein AM before (d) and after (e) insertion in "brain phantom".

4.3 Histology

Neural electrodes operate by capturing the electrical signals that are exchanged across neurons, and their efficacy is greatly influenced by factors such as the quantity and proximity of neighboring neuronal cell bodies. For this reason, in order to evaluate a posteriori via histological assessment the effectiveness of a neural interface, it is critical to quantify and localize different cell-types in the implant niche.

Animals that underwent implantation of the tissue-engineered neural probes were sacrified after two weeks from the implant, and histological preparations have been obtained with the procedures described in Appendix 1. In particular, brain slices were subjected to staining with NeuN and NF200 in order to detect any variation of neuron number and axon density, respectively, in close proximity to the location of electrode implantation (Fig 4.3).

In the case of BMEC-coated devices, it is possible to observe a substantially higher concentration of neurons in the vicinity of the implants with respect to uncoated ones. (Fig.4.3b, c). As one moves in a radial direction from the site, it can be observed that the density of neurons in the tissues of cell-coated samples remains higher until approximately 60 µm away from the electrode. However, beyond this distance, no significant variations in neuron density can be observed between the experimental (BMEC-coated) and control (uncoated) groups. The NF200 staining results revealed no statistically significant changes between the groups, suggesting a uniformity in axonal density surrounding the implants (Fig.4.3d, e).

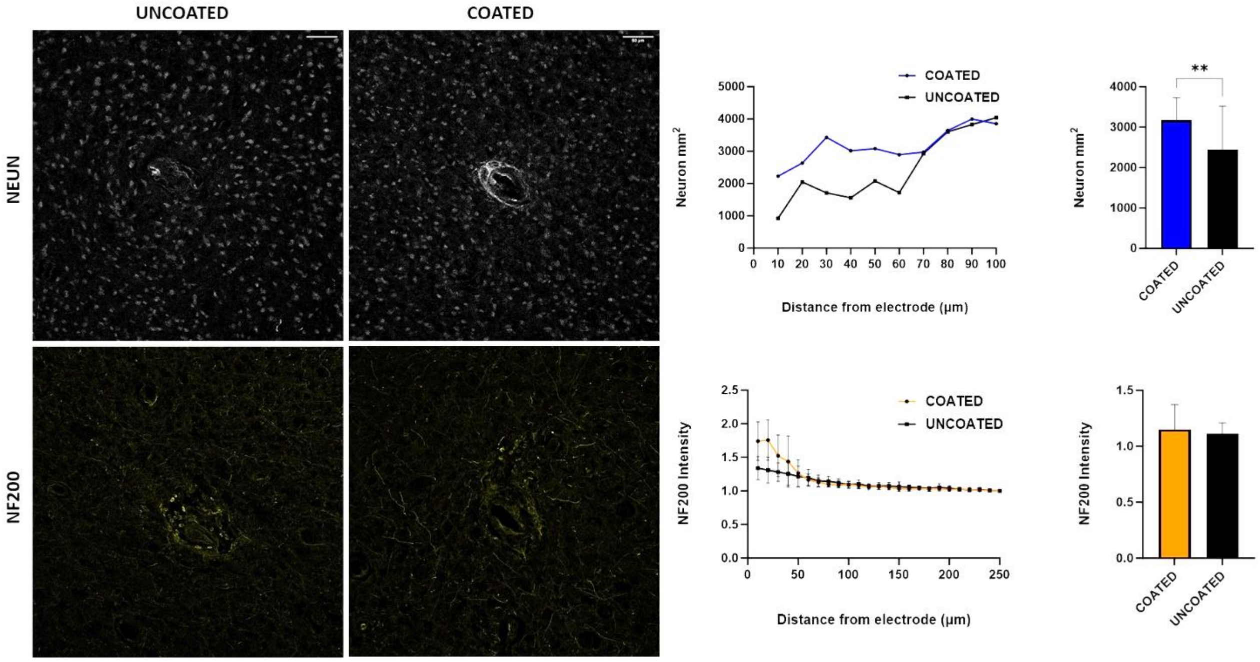

Figure.4.3 | Neuron density close to the electrode site is preserved by rBMECs device coating. (a) NeuN (neurons) and NF200 (axons) staining representative images for the groups of control and BMEC-coated devices. (b)Number of neurons per square micrometer (¼m) as a function of the distance from the implant center is shown. (c) Histogram showing the neuron density average in coated and uncoated devices, with statistically significant difference. (d) NF200 intensity as a function of distance from electrode, normalized to image corners. (e) A histogram showing the normalized NF200 intensity average. (: $p < 0.01$, two-way ANOVA).**

The validation of the viability of neurons next to electrodes in a BMEC-coated device implant, in comparison to the control group was, in parallel, performed via Caspase-3 quantification (Figures 4.4a). Caspase-3 serves as a reliable indication of apoptotic cell death, specifically in the context of neuronal mortality. Its presence aids in identifying the potential decline of healthy neurons resulting from inflammation. The manual quantification of Caspase-3, described in Appendix 1, demonstrated diminished apoptosis for the BMEC-coated device group compared to the control devices, in a distance range from the site of implantation comparable with that highlighted by NeuN staining. However, it is important to note that this difference did not reach statistical significance, likely due to the limited number of caspase-3 positive cells and to the small dimension of the sample (Figure 4.4b).

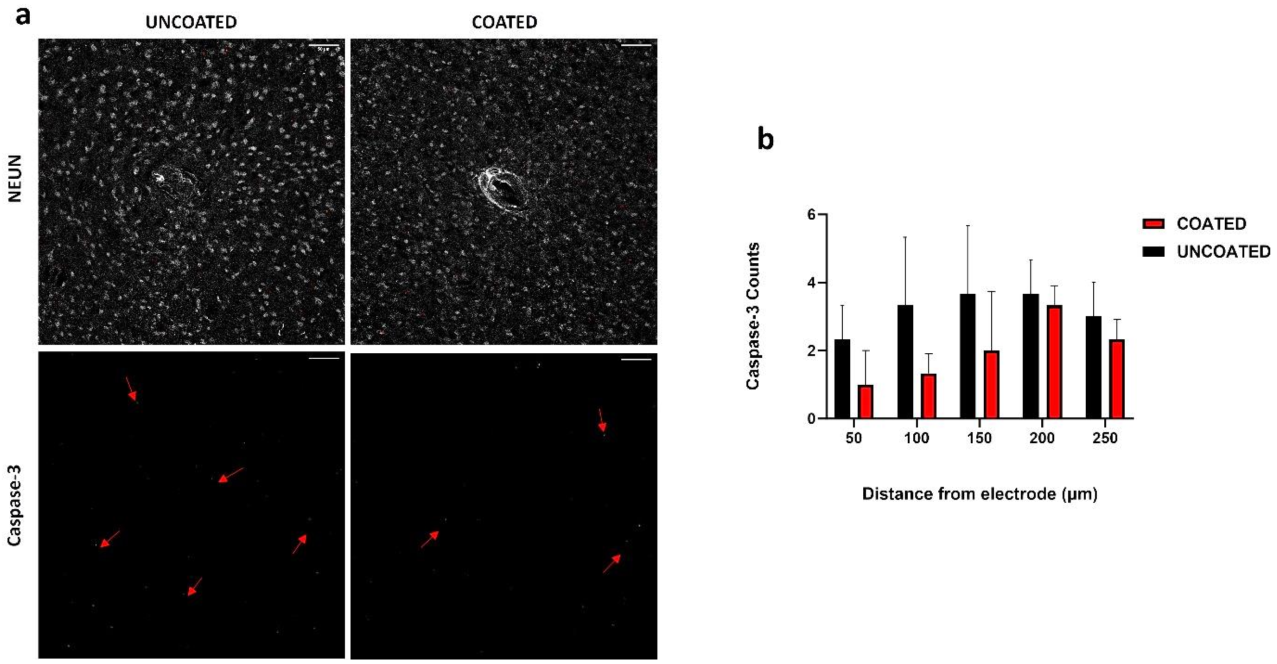

Figure 4.4 | Caspase-3 expression is reduced by rBMECs device coating. (a) Caspase-3 (apoptosis marker) staining representative images for the groups of control and cell-coated devices. Areas expressing Caspase-3 are shown by red arrows. Caspase-3 (green) and NeuN (grey) overlay to show neuron death. (b) The two groups' Caspase-3 numbers at various distances from the electrode center (n.s.Two-way ANOVA).

An additional investigation was conducted to assess the degree of astrocytic and microglial encapsulation of the electrodes. The quantification of reactive astrocytes was carried on using GFAP staining, whereas the assessment of the inflammatory reaction after implantation was accomplished by Iba-1 stains (Figures 4.5a). The staining with GFAP demonstrated a higher intensity (i.e., a higher density of reactive astrocytes) in the case of control uncoated devices, as opposed to the group of tissue-engineered devices. The variation of GFAP intensity exhibits a peak in proximity to the electrode location, followed by a gradual decrease (Fig. 4.5b, c). The Iba-1 staining intensity was employed to assess and compare the microglial response to the implanted probes, showing an increase in the expression of Iba-1. For the engineered device, the staining intensity of Iba-1 exhibits a notable reduction with respect to the uncoated one. Furthermore, when considering the entire population of microglia, it is possible to observe a reduction in the case of BMEC-coated probes with respect to uncoated ones (Figure 4.5d, e).

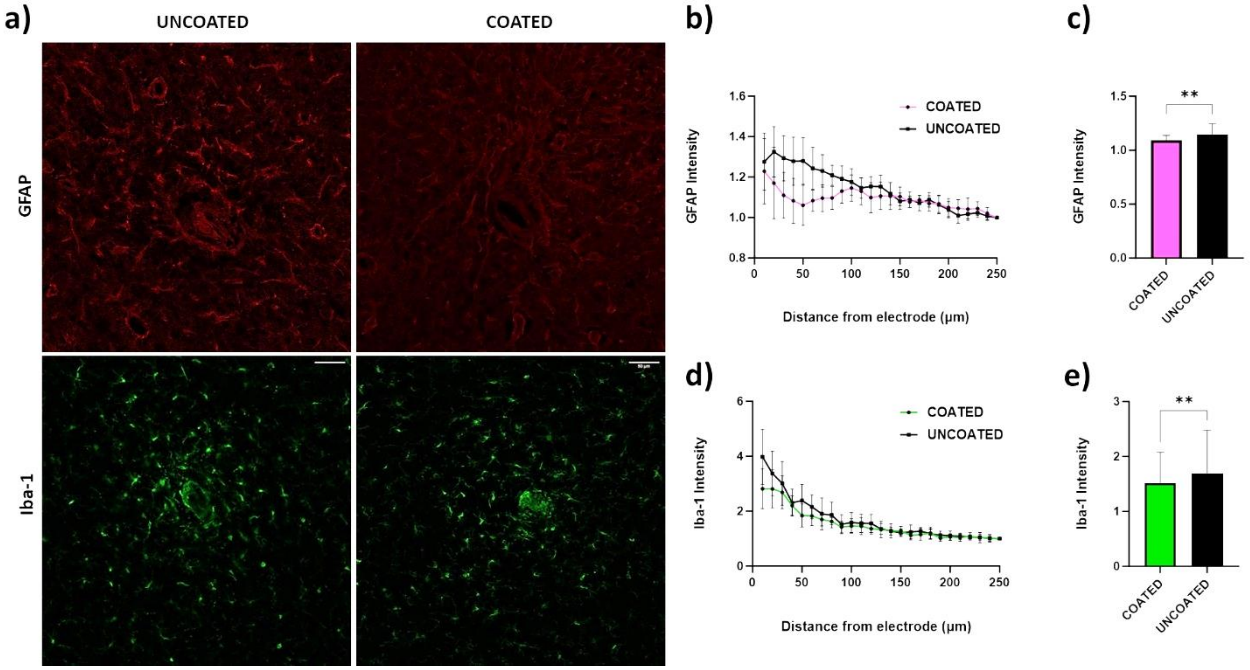

Figure 4.5 | Astrocytic and microglial activation close to the electrode is inhibited by the device coating of rBMECs. (A) GFAP (astrocytes) and Iba-1 (microglia) staining representative photos of the control and cell-coated device groups. (b) GFAP intensity plotted against distance from electrode center, normalized to image corners. (c) A bar graph showing the average normalized GFAP intensity. (d) Iba-1 intensity normalized to image corners plotted against electrode center distance. (c) Bar graph showing the average normalized Iba-1 intensity. (: p < 0.01, Two-way ANOVA).**

1. Neuwelt, E. A. et al. Engaging neuroscience to advance translational research in brain barrier biology. Nat Rev Neurosci 12, 169–182 (2011).

2. Ohtsuki, S. & Terasaki, T. Contribution of Carrier-Mediated Transport Systems to the Blood–Brain Barrier as a Supporting and Protecting Interface for the Brain; Importance for CNS Drug Discovery and Development. Pharm Res 24, 1745–1758 (2007).

3. Bittner, S. et al. Endothelial TWIK-related potassium channel-1 (TREK1) regulates immune-cell trafficking into the CNS. Nat Med 19, 1161–1165 (2013).

4. Kleinschnitz, C. et al. Glucocorticoid Insensitivity at the Hypoxic Blood–Brain Barrier Can Be Reversed by Inhibition of the Proteasome. Stroke 42, 1081–1089 (2011).

5. Perrière, N. et al. Puromycin-based purification of rat brain capillary endothelial cell cultures. Effect on the expression of blood–brain barrier-specific properties. Journal of Neurochemistry 93, 279–289 (2005).

6. Pomfret, R., Miranpuri, G. & Sillay, K. The Substitute Brain and the Potential of the Gel Model. Ann Neurosci 20, 118–122 (2013).

5. B-estradiol 17-acetate enhances the in vitro vitality of endothelial cells isolated from the brain of patients subjected to neurosurgery

This chapter presents a study conducted to introduce a novel methodology that improve the *in vitro* viability of human cerebral microvascular endothelial cells (hBMECs) isolated from brain samples, as cryopreserved autologous cells for biomimetic therapeutic applications.

This activity led to the publication of the article: “Guzzo, S., De Bonis, P., Pavan, B. & Fadiga, L. β-Estradiol 17-acetate enhances the in vitro vitality of endothelial cells isolated from the brain of patients subjected to neurosurgery. *Neural Regeneration Research* **18**, 389 (2023).

In the current landscape of endothelial cell isolation for building *in vitro* models of the blood-brain barrier, our work moves towards reproducing the features of the neurovascular unit to achieve glial compliance through an innovative biomimetic coating technology for brain chronic implants. We hypothesized that the autologous origin of human brain microvascular endothelial cells (hBMECs) is the first requirement for the suitable coating to prevent the glial inflammatory response triggered by foreign neuroprosthetics. Therefore, this study established a new procedure to preserve the *in vitro* viability of hBMECs isolated from gray and white matter specimens taken from neurosurgery patients. Culturing adult hBMECs is generally considered a challenging task due to the difficult survival *ex vivo* and progressive reduction in proliferation of these cells. The addition of 10 nM β-estradiol 17-acetate to the hBMEC culture medium was found to be an essential and discriminating factor promoting adhesion and proliferation both after isolation and thawing, supporting the well-known protective role played by estrogens on microvessels. In particular, β-estradiol 17-acetate was critical for both freshly isolated and thawed female-derived hBMECs, while it was not necessary for freshly isolated male-derived hBMECs; however, it did counteract the decay in the viability of the latter after thawing. The tumor-free hBMECs were thus cultured for up to 2 months and their growth efficiency was assessed before and after two periods of cryopreservation. Despite the thermal stress, the hBMECs remained viable and suitable for re-freezing and storage for several months. This approach increasing *in vitro* viability of hBMECs opens new perspectives for the use of cryopreserved autologous hBMECs as biomimetic therapeutic tools, offering the potential to avoid additional surgical sampling for each patient.

5.1 Primary endothelial cell cultures from neurosurgical resections of GM and WM of adult or older adult patients

Samples after recruitment consisted of cortical GM and subcortical WM specimens collected from five female patients (F1-F2-F3-F4-F5) and five male patients (M1-M2-M3-M4-M5), all aged 55–75 years old. For clinical reasons, resected peritumoral specimens of both WM and GM could not always be removed in useful sizes from each patient, therefore both WM and GM were resected from M2 and M4, while only GM specimens were taken from M1, and only WM specimens were removed from all female patients and the male M5 patient (Table 1).

Table 1 | Patient recruitment and classification and tumor type and grade

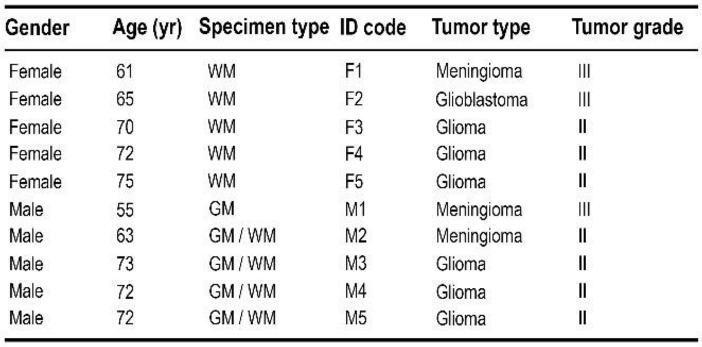

Gender	Age (yr)	Specimen type	ID code	Tumor type	Tumor grade
Female	61	WM	F1	Meningioma	III
Female	65	WM	F2	Glioblastoma	III
Female	70	WM	F3	Glioma	II
Female	72	WM	F4	Glioma	II
Female	75	WM	F5	Glioma	II
Male	55	GM	M1	Meningioma	III
Male	63	GM / WM	M2	Meningioma	II
Male	73	GM / WM	M3	Glioma	II
Male	72	GM / WM	M4	Glioma	II
Male	72	GM / WM	M5	Glioma	II

Upon first plating, GM-derived hBMECs isolated from male patients M1 to M4 spontaneously adhered to the substrate and showed rounded cell clusters associated with the residues of capillary fragments and scattered single cells and debris. These endothelial cells displayed morphological characteristics with typical swirling patterns and whorls and no evident vacuoles, highlighting their overall health. No giant cells or spreading and non-contrasted cells (sign of degeneration) appeared during any growth steps after isolation (see the phase contrast images in Figure 5.1a). After 1–3 days of culture, cells sprouted from clusters and elongated; after 20 days, confluent colonies of hBMECs isolated from GM of all four male patients were observed. Cultures of WM-derived hBMECs from male patients M2-M adhered and proliferated but showed lower cell density at confluence compared with GM-derived hBMECs ($P < 0.001$), even if belonging to the same patient, as reported by the growth curves of Figure 5.1c.

In contrast, resections of WM from female patients F1, F2 and F3 did not provide adherent or growing cultures, independently of their age, because the addition of β-estradiol 17-acetate to the culture medium of the deriving hBMECs had not yet been considered. In fact, when 10 nM β-estradiol 17 acetate was further added to the growth medium after 2 days in culture, WM-derived hBMECs from patients F4 and F5 interestingly showed strong adhesion and growth capacity significantly exceeding that of GM-derived male hBMECs ($P < 0.001$) after 10 days in culture (Figure 5.1c). Therefore, following the addition of β-estradiol 17-acetate, F4- and F5-derived WM-hBMECs displayed a swirling pattern similar to the GM-hBMECs isolated from male patients (see the phase contrast images in Fig. 5.1b), achieving a significant increase in cell number 13 days after isolation ($P < 0.001$) and confluent colonies after 22 days (Fig. 5.1b). Notably, subcultures of F4- and F5-derived WM-hBMECs treated with the same concentration of DMSO as a vehicle (0.0001%) or with hormone at the concentrations lower than 10 nM failed to adhere or lose their growth behavior compared with 10 nM estrogen-treated endothelial cells. Consequently, these cells were discarded as waste. Therefore, 10 nM has shown the lowest effective concentration of β-estradiol 17-acetate that can stimulate endothelial cell growth in vitro, as also observed in our previous study on dose-dependent release of PGE2 induced by estrogen in human amnion-derived WISH cells[1]. Consequently, a 10 nM concentration of β-estradiol 17-acetate was used to maintain the viability of both male and female WM- and GM-derived hBMECs in culture.

The addition of 10 nM β-estradiol 17-acetate to the growth medium of hBMECs after fresh isolation from WM of male patients M4 and M5 induced a significant increase in cell density after 20 days ($P < 0.05$) compared with the untreated male WM-hBMECs (Figure 5.1a and c), and clearly never reached the responsiveness to the hormone exhibited by the female WM-hBMECs nor by the male GM-hBMECs after thawing (see below). Finally, it is noteworthy that in all the hBMEC cultures described above, once confluence was reached, contact inhibition of their proliferation without formation of post-confluent multilayer foci was observed, as a fundamental behavior of normal endothelial cells.

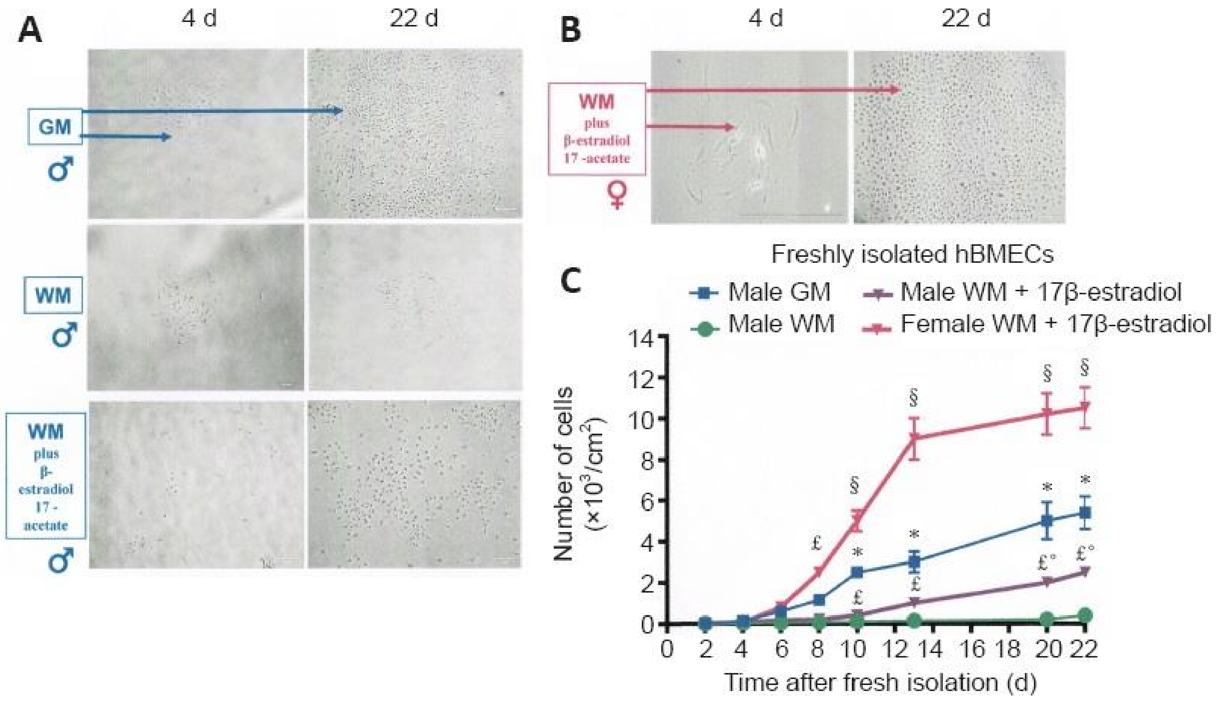

Figure 5.1 | Effects of donor's gender, tissue source and 10 nM β-estradiol 17-acetate on hBMECs recovery and growth after fresh isolation from neurosurgical specimens. Representative phase contrast images of morphology and density of female WM-derived hBMECs spiked with 10 nM β-estradiol 17-acetate, after 4 and 22 days in culture from isolation. Scale bars: 20 µm. (B) Representative phase contrast images of male GM-derived hBMECs in the absence of 10 nM β-estradiol 17-acetate, and male WM-derived hBMECs in the absence and presence of 10 nM β-estradiol 17-acetate, after 4 and 22 days in culture from isolation. Scale bar: 20 µm. (C) Comparison between growth curves of GM-derived hBMECs freshly isolated from male patients M1-M4 in the absence of 10 nM β-estradiol 17-acetate (blue squares) and WM-derived hBMECs freshly isolated from male patients M2-M5 in the absence (green circles) and presence of 10 nM β-estradiol 17-acetate (violet triangles) and WM-derived hBMECs isolated from female patients F4 and F5 and spiked with 10 nM β-estradiol 17-acetate (dark pink triangles). Each

independent culture was related to GM-derived hBMECs (n = 4) and to WM-derived hBMECs (n = 4) obtained from male patients, and to WM-derived hBMECs (n = 2) obtained from female patients. Each point represents the mean ± SEM of four experiments from individual cell preparations obtained from each donor. Effects of days of culture, gender and/or estrogen treatment on growth curves were analyzed by two-way analysis of variance followed by the Tukey's multiple comparisons test. *P = 0.001 for male GM-hBMECs vs. male WM-hBMECs; °P = 0.05 for male WM-hBMECs vs. male β-estradiol 17-acetate-treated WM-hBMECs; §P = 0.001 for female β-estradiol 17-acetate-treated WM-hBMECs vs. male GM-hBMECs; £P = 0.01 for female β-estradiol 17-acetate-treated WM-hBMECs vs. male β-estradiol 17-acetate-treated WM-hBMECs. GM: Gray matter; hBMECs: Human cerebral microvascular endothelial cells; WM: white matter.

5.2 Effects of cryopreservation on WM-derived hBMECs isolated from female patients and exposed to β-estradiol 17-acetate

F4–F5-WM-hBMECs, treated with β-estradiol 17-acetate, were cryopreserved at –80°C for 1 month. Then they were thawed and seeded in growth medium spiked again with 10 nM β-estradiol 17-acetate. β-Estradiol 17-acetate induced a complete recovery of viability of F4–F5-WM-hBMECs and sustained their proliferation until the thirty-third day of culture with routine splitting every 8 days (Fig. 5.2a). Then F4–F5-WM-hBMECs were immediately harvested for subsequent freezing stages. In particular, withdrawal of β-estradiol 17-acetate from the growth medium in separate dishes of F4–F5-WM-hBMECs at the first split 12 days post-thawing decreased their proliferation rate and adhesion to the substrate (Fig. 5.2c). No recovery was induced by a new addition of the hormone after 4 days of estrogenic starvation (Fig. 2c inserted panel).

5.3 β-Estradiol 17-acetate restores viability and proliferation of male GM-derived hBMECs after thawing

Unlike female WM-derived hBMECs, which adhered and grew to the confluence only in the presence of β-estradiol 17-acetate, cultures of patients M1–M4 GM-derived hBMEC never exposed to the estrogen hormone after fresh isolation grew sufficiently and were thus cryopreserved in freezing medium. However, after thawing and seeding, all the hBMECs deriving from the corresponding patients M1 to M4 showed rapid decreases in adhesion to the substrate and proliferation rate with progressive weakening and loss in culture. Therefore, in order to verify a possible estrogen sensitivity of male hBMECs as far as recovery from freezing is concerned, frozen aliquots of patients M1–M4

GM-derived hBMECs were thawed and seeded in a growth medium added with 10 nM β-estradiol 17-acetate during 32 days of routine subculture. Interestingly, a huge response to estrogens by male GM-derived hBEMCs in terms of viability, cell density at confluence and proliferation rate (Fig.5.2b) were observed, with a complete recovery occurring even faster than the one observed in hBMECs from female patients, although not statistically different (*P* > 0.05). Withdrawal of β-estradiol 17-acetate from the growth medium in separate dishes of M1-M4-GM-derived hBMECs at the first split 4 days post-thawing induced a fully reversible slow viability reduction (Fig. **5.**2c) when hormone was added back to the culture medium after 8 days of estrogenic starvation.

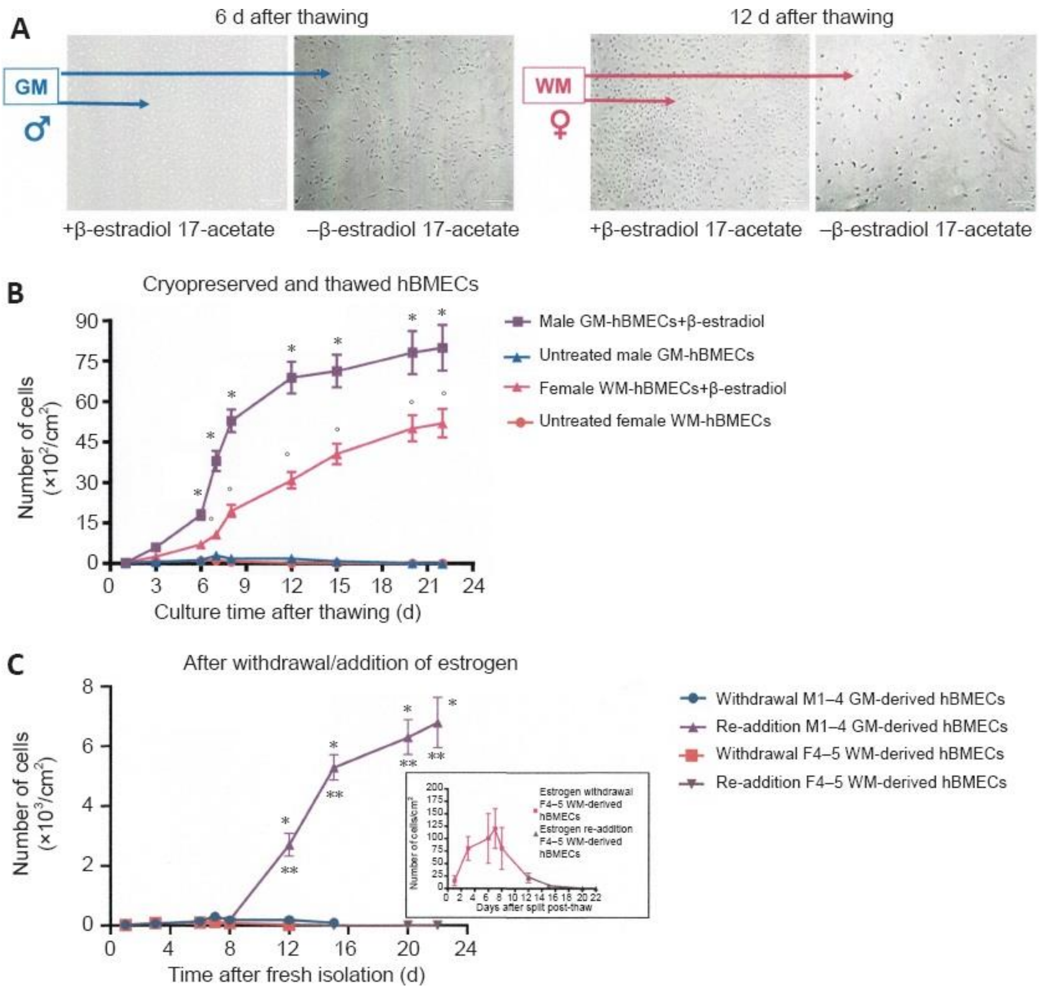

Figure 5.2 | Effect of donor's gender, tissue source and 10 nM β-estradiol 17-acetate on hBMECs recovery and growth after thawing from cryopreservation and splitting. (A) Representative phase contrast images of morphology and density of male GM-derived hBMECs and of female WM-derived hBMECs subcultured for 6 days and 12 days, respectively, after thawing from cryopreservation both in the presence and in the absence of 10 nM β-estradiol 17-acetate. Scale bars: 20 μm. (B) Comparison between growth curves related to GM-derived hBMECs isolated from male patients M1-M4, thawed and subcultured in the absence (blue triangles) and in the presence (violet squares) of 10 nM β-estradiol 17-acetate, and growth curves related to WM-derived hBMECs isolated from female patients F4–F5, thawed and subcultured in the presence (pink triangles) and in the absence (red circles) of 10 nM β-estradiol 17-acetate. (C) Effects of withdrawal (blue circles) and new addition (violet triangles) of 10 nM β-estradiol 17-acetate on recovery and growth after thawing of GM-derived hBMECs isolated

from male patients M1-M5 and effects of withdrawal of 10 nM β-estradiol 17-acetate on recovery and growth after thawing of WM-derived hBMECs isolated from female patients F4–F5, each subcultured after thawing. The inserted graph represents the magnification of the failed recovery after withdrawal and re-addition of 10 nM β-estradiol 17-acetate in WM-derived hBMECs from female patients F4–F5. Each point represents the mean ± SEM of four experiments from individual cell preparations obtained from each donor. Effects of thawing, gender and/or estrogen treatment on growth curves were analyzed by two-way analysis of variance (P = 0.0001) followed by the Tukey's multiple comparisons test. (B) Male GM-derived hBMECs with estrogen vs. male GM-derived hBMECs without estrogen, *P = 0.0001; female WM-derived HBMECs with estrogen vs. female WM-derived hBMECs without estrogen, °P = 0.0001. (C) Male GM-derived hBMECs withdrawal of estrogen vs. male GM-derived hBMECs re-addition of estrogen, *P = 0.0002; male GM-derived hBMECs re-addition of estrogen vs. female WM-derived hBMECs readdition of estrogen, **P = 0.0007. GM: Gray matter; hBMECs: Human cerebral microvascular endothelial cells; WM: white matter.

5.4 Recovery in endothelial cell viability

As shown in Figure **5.**3, after thawing and splitting, the yield from male GM-derived hBMECs was 8 to 9 × 10^5 live cells/mL and 5 to 6 × 10^4 dead cells/ mL resulting in a viability of 93 ± 4% by the trypan blue dye exclusion assay. The yield from male WM-derived hBMECs was 6 to 7 × 10^5 live cells/mL and 1 to 1.2 × 10^4 dead cells/mL, resulting in a viability of 84 ± 2%. The yield of female WM-derived hBMECs was 6 to 7 × 10^5 live cells/mL and 0.8 to 1 × 10^4 dead cells/mL with a viability of 88 ± 3%. There were no statistically significant differences in the number of live cells yielded by WM- *versus* GM-derived hBMECs ($P = 0.1035$).

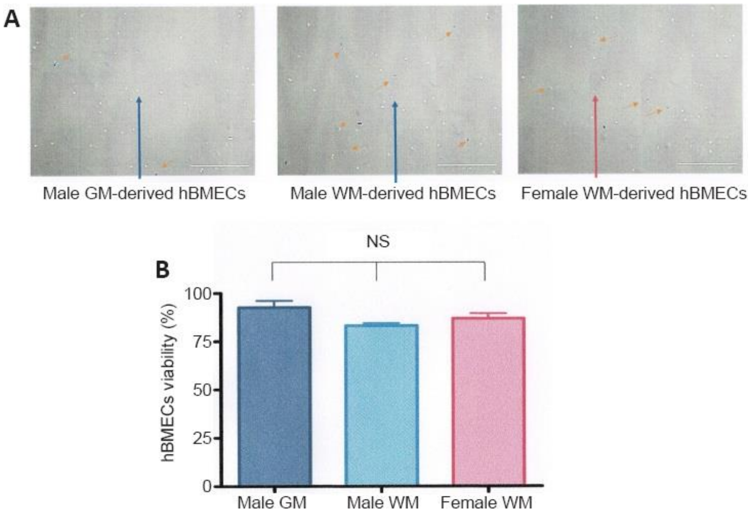

Figure 5.3 | Cell viability. (A) Phase contrast images of bright fields of the hemocytometer and (B) quantification of the live/dead trypan blue exclusion assay, referred to male GM- and WM-derived hBMECs and female WM-derived hBMECs, each of them splitted after thawing. Red arrows indicate dead cells. Scale bar = 50 µm. No statistical differences (NS) in viability resulted from one-way analysis of variance (P = 0.1035) followed by

Bonferroni's multiple comparisons test, performed on three aliquots of cells deriving from three independent cultures (n = 3) of each male GM- and WM-derived hBMECs and female WM-derived hBMECs, respectively. GM: Gray matter; hBMECs: Human cerebral microvascular endothelial cells; WM: white matter

5.5 WM- and GM-derived hBMECs express surface constitutive but not tumoral endothelial markers

Both female and male patient WM- and GM-derived hBMECs (freshly isolated and after thawing) were stained by immunofluorescence for specific surface antigen marker of different endothelial tumor entities. Immunofluorescence staining of all markers was merged with the nuclear Hoechst dye and compared to their staining in brain endothelial hCMEC/D3 cells activated with 10 ng/mL TNF-α used as positive control[2]. All the cultured hBMECs before and after thawing (Fig. 5.4a) showed a detectable expression of PECAM-1 or CD31, which is regarded as the best constitutive endothelial marker. No statistically significant difference (*P* = 0.9999) in CD31 expression was observed if all types of hBMECs were compared each to other, whereas highly significant differences were observed in comparison with the positive control, as shown in the immunofluorescence quantification (Fig. 5.4b). Both female WM- and male GM-derived hBMECs were stained for cluster of differentiation 54 (CD54) or ICAM-1 (Fig. 5.4c), a 90 kDa member of the immunoglobulin superfamily, which was constitutively expressed in both brain microvascular endothelial cells and umbilical vein endothelial cells[3], but it was also normally activated in aged endothelial tissue[4]. TNF -alpha activated hCMEC/D3 cells were a valuable positive control for CD54 marker (Figure 5.4c), showing a fluorescence intensity 1.5-fold higher than female WM-derived hBMECs (*P* = 0.0004) and 1.8-fold higher than GM-derived-hBMECs (*P* = 0.0001), whereas CD54 fluorescence intensity was 1.3-fold higher in female WM-derived hBMECs than GM-derived-hBMECs (*P* = 0.0167). All the cultured hBMECs showed negativity for glycoprotein E-selectin (CD62E), a cell adhesion molecule (CAM), expressed on brain tumor endothelium[5,6], whereas TNF-α activated hCMEC/D3 cells were positive for control of CD62E staining (Figure 5.4d), confirming the upregulation of CD62E in hCMEC/D3 cells and cancer cells in response to a TNF-α inflammatory stimulus, as reported by other authors[2,7,8].

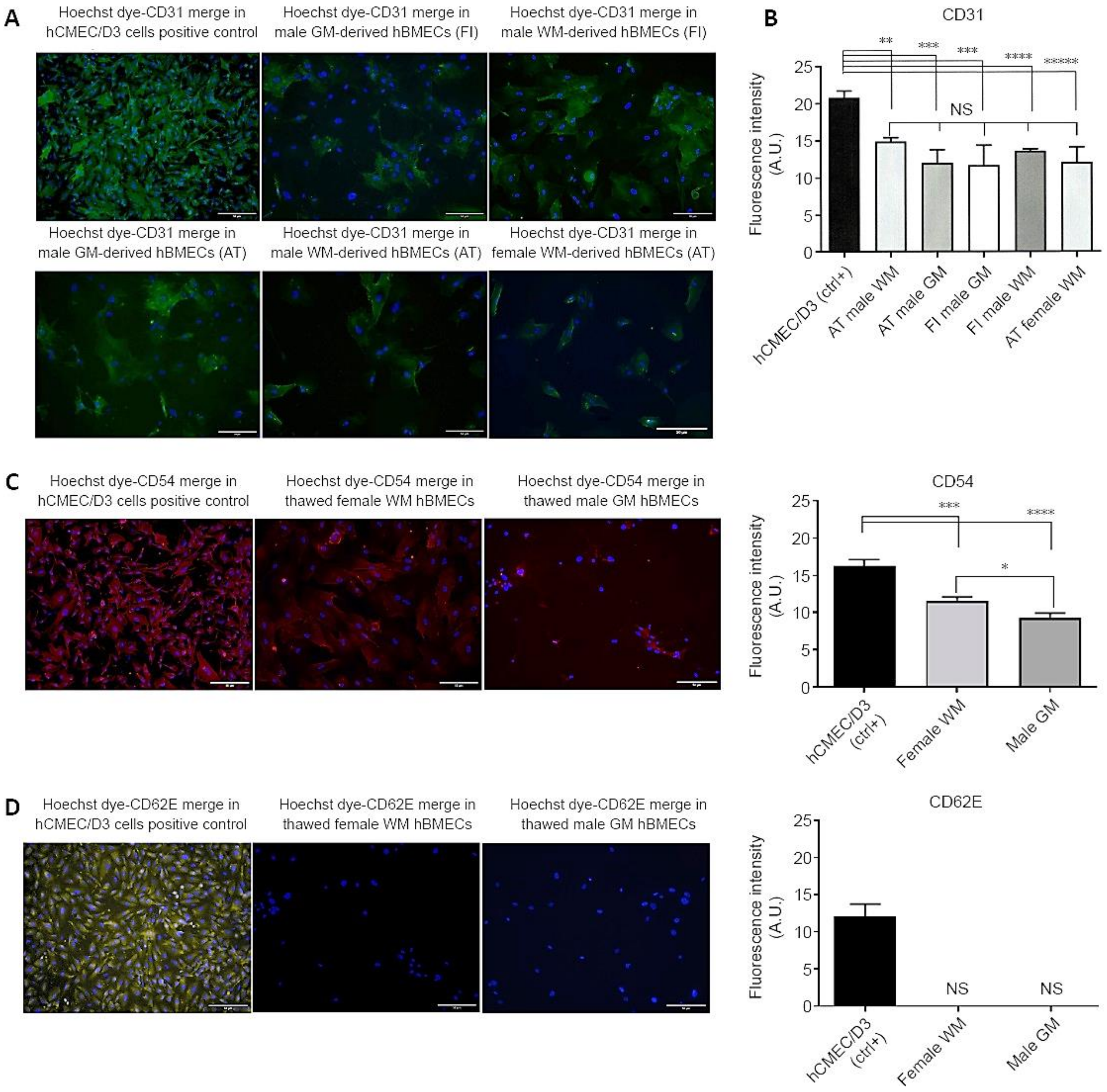

Figure 5.4 | Visualization and quantification of immunofluorescence staining of CD31, CD54 and CD62E markers in representative cultures of male GM- and WM-derived hBMECs and female WM-derived hBMECs. (A) Constitutive expression of the endothelial marker CD31 or PECAM-1 was shown for all the types of hBMECs both after fresh isolation and after thawing from cryopreservation. TNF-α activated hCMEC/D3 cells were used as positive control for staining of CD31. CD31 primary antibody was stained in green by fluorochrome-conjugated goat anti-mouse secondary antibody Alexa Fluor 488 and nuclei were stained by the blue Hoechst 33342 dye. (B) Immunofluorescence intensity quantification (in arbitrary units; A.U.) of CD31-stained hBMECs in comparison to the TNF-α activated hCMEC/D3 cells, CD31 positive control. Scale bars: 50 µm. **P = 0.0075, ***P = 0.0002, ****P = 0.0016, *****P = 0.0003. (C) CD54 or ICAM-1 exhibited a low expression in male GM-derived hBMECs and female WM-derived hBMECs compared with the positive control TNF-α activated hCMEC/D3 cells, as shown by fluorescence intensity quantification. CD54 primary antibody was stained in red by fluorochrome-conjugated goat anti-mouse secondary antibody Alexa Fluor 633 and nuclei were stained by the blue Hoechst 33342 dye. Scale bars: 50 µm. *P = 0.0167, ***P = 0.0004, ****P = 0.00001. (D) CD62E or E-Selectin was clearly seen as being negative both for male GM-derived hBMECs and female WM-derived hBMECs in comparison with the TNF-α activated hCMEC/ D3 cells, as shown by fluorescence intensity quantification. CD62-E primary antibody was stained in orange-yellow by fluorochrome-conjugated goat anti-mouse secondary antibody Alexa Fluor 568 and nuclei were stained by the blue Hoechst 33342 dye. All the endothelial markers were merged with the nuclear Hoechst 33342 dye. Scale bars: 50 µm. Each point represents the mean ± SEM of four experiments from individual cell preparations obtained from each donor. Significance was calculated by one-way analysis of variance followed

by Dunnet’s post hoc test, comparing each marker staining in hBMECs with its staining in hCMECs/D3 positive control. AT: After thawing; FI: Fresh isolation; GM: gray matter; hBMECs: Human cerebral microvascular endothelial cells; WM: white matter.

1. *Pavan, B., Biondi, C., Ferretti, M. E., Lunghi, L. & Paganetto, G. 17β-Estradiol Modulates Prostaglandin E2 Release from Human Amnion-Derived WISH Cells1. Biology of Reproduction **64**, 1677–1681 (2001).*

2. *Weksler, B. B. et al. Blood-brain barrier-specific properties of a human adult brain endothelial cell line. The FASEB Journal **19**, 1872–1874 (2005).*

3. *Huber, J. D., Campos, C. R., Mark, K. S. & Davis, T. P. Alterations in blood-brain barrier ICAM-1 expression and brain microglial activation after λ-carrageenan-induced inflammatory pain. American Journal of Physiology-Heart and Circulatory Physiology **290**, H732–H740 (2006).*

4. *Goncharov, N. V. et al. Markers of Endothelial Cells in Normal and Pathological Conditions. Biochem. Moscow Suppl. Ser. A **14**, 167–183 (2020).*

5. *Miebach, S. et al. Isolation and Culture of Microvascular Endothelial Cells from Gliomas of Different WHO Grades. J Neurooncol 7**6**, 39–48 (2006).*

6. *Jassam, S. A. et al. CD15s/CD62E Interaction Mediates the Adhesion of Non-Small Cell Lung Cancer Cells on Brain Endothelial Cells: Implications for Cerebral Metastasis. International Journal of Molecular Sciences **18**, 1474 (2017).*

7. *Jassam, S. A. et al. TNF-α enhancement of CD62E mediates adhesion of non–small cell lung cancer cells to brain endothelium via CD15 in lung-brain metastasis. Neuro-Oncology **18**, 679–690 (2016).*

8. *Dunst, J., Kamena, F. & Matuschewski, K. Cytokines and Chemokines in Cerebral Malaria Pathogenesis. Frontiers in Cellular and Infection Microbiology 7, (2017).*

CONCLUSIONS and PERSPECTIVES

This thesis addresses the field of neural interfaces, focusing on two main approaches aimed at improving device long/mid-term stability and performances: the evaluation of novel biocompatible conductive organic materials as electrode coatings and the application of tissue engineering techniques to reduce inflammatory tissue response after implantation.

Concerning the first approach, this thesis encompasses the evaluation of a newly synthetized water-dispersion of PEDOT:Nafion as a biocompatible conductive material and the investigation of PEDOT:PSS nanomodulated substrate for stimulation and polarization of neurites. The results obtained in these studies indicate, respectively, that PEDOT:Nafion substrates are non-cytotoxic and support adhesion and proliferation of fibroblasts on their surface, promoted by the multiscale roughness of the material itself. Moreover, they demonstrate that, on nano-modulated PEDOT:PSS substrates, the length of neurites can be increased by electrical stimulation, and the polarization of neurites can be spatially directed and accelerated by the nanostructured topography, underscoring the importance of the synergistic integration between topographic and electrical cues enabled by functional active material coatings in neural interfaces.

Regarding the second approach, this thesis presents the first investigation of a brain endothelial cells-based tissue engineering approach aimed at mitigating the foreign-body reaction upon deep-brain probe implantation. This task is addressed from a dual perspective: on the one hand, the foreign body reaction to tissue-engineered neural probes has been evaluated in animal models and, on the other hand, a novel protocol for increasing the cell viability of human autologous brain microvascular endothelial cells has been demonstrated. The results showed respectively that biohybrid constructs consisting of allogenic endothelial cells have an inhibitory impact on microglial encapsulation and astrocytic activation, thereby maintaining the density of neurons in the acute setting and demonstrating neuroprotective properties in sub-chronical scenarios (i.e., two weeks after implantation). Additionally, complete recovery of viable autologous human brain microvascular endothelial cells, either freshly isolated or cryopreserved from surgical sampling has been assessed.

This thesis supports the proneness of both proposed approaches to undergo further investigation for in vivo applications, particularly in chronic conditions.

PEDOT:Nafion has been demonstrated as a viable alternative to the widely used PEDOT:PSS in neural interfaces. Additionally, the results obtained with nanomodulated PEDOT:PSS substrates can be further developed either integrating such coatings with advanced functionalities onto biodegradable scaffolds for transient electronics (e.g. in the treatment of partial spinal cord injury) or by designing PEDOT:PSS/PEDOT:Nafion composites, coupling the high conductivity of PEDOT:PSS with the high charge injection limit of PEDOT:Nafion, herein demonstrated. A follow-up study is also needed to evaluate the electrochemical features of the biohybrid constructs stemming from the tissue engineering approaches and to establish the relationship between optimal recording quality and mitigation of tissue inflammation, also in chronic scenarios.

In conclusion, the (bio-)technological routes developed in this thesis show promising potential for improving the electrical integration at the interface between neurons and electrodes, thus contributing to the lasting effectiveness of neural prostheses and providing growingly refined tools for translational neuroscience and neurotechnology.

Appendix 1

Sections referring to the published paper reported in Chapter 2.
https://doi.org/10.3390/nano11082022

Synthesis of PEDOT:Nafion and Coating Fabrication

PEDOT:Nafion water dispersion was synthesized according to previously reported protocol[1]. The obtained water dispersion of PEDOT:Nafion (1 mL) was diluted with water (5 mL), and the mixture was sonicated at room temperature for 15 min. This treatment is necessary to reduce the aggregates in order to give an optimal deposition of PEDOT:Nafion. Subsequently, coatings were fabricated by drop casting 30 µL of the PEDOT:Nafion dispersion with a pipette on borosilicate glass slides (1X1 cm^2, thickness ~ 1 mm, average root mean square (RMS) roughness: (0.21±0.02) nm, Thermo Fisher Scientific, Milan, Italy) previously cleaned with an isopropyl alcohol, ethanol and water (1:1:1 vol%) solution and dried with N_2. Subsequently, coatings were annealed at 120° C for 40 min.

Surface Characterization of PEDOT:Nafion Coatings

Surface topography of PEDOT:Nafion coatings was investigated by atomic force microscopy (AFM). Images were acquired using a Park XE7 AFM System (Park Systems, Suwon, Korea) operating in tapping mode in air at room temperature. Premounted silicon cantilevers were used (OMCL-AC160TS, tip curvature radius ~ 7 nm, k ~ 26 N/m and Al backside coating, Olympus, Tokyo, Japan). The RMS was extracted from several topography images acquired at different scan size, i.e., from 1x1 μm^2 to 10 _ 10 μm^2, using the XEI Software (XEI, version 4.3; Park Systems, Suwon, Korea, 2016). All images were previously flattened using a 2nd order regression in x direction and a 1st order regression in Y direction. All values are reported as mean ± standard deviation. Wettability of PEDOT:Nafion coatings was investigated by a home-built water contact angle measurement unit. The value of the contact angle was obtained by averaging several measurements of the left and right contact angle of the water drop taken on different areas of the samples by using the ImageJ free software (https://imagej.nih.gov/).

Isolation and Culture of Primary Rat Fibroblasts

Fibroblasts were isolated from tail of Long–Evans rat (Charles River Laboratories, Lecco, Italy) during routine surgery and the seeded for culture. Experiments were performed in compliance with the guidelines established by the European Communities Council (Directive 2010/63/EU, Italian Legislative Decree n. 26, 4 March 2014), and the protocol was approved by the Ethics Committee for animal research of the University of Ferrara and by the Italian Ministry of Health (protocol n. 989/2020-PR, date 15 October 2020). Briefly, specimens (~1 cm) from scarification of the tail tip were obtained after skin sterilization with 70% v/v ethanol/water. Specimens were further washed in phosphate buffer saline (PBS, pH 7.4) and minced by scissors. Homogenate tissue was transferred into a sterile conical bottom tube and digested by an enzymatic mixture of 5 mg/mL Dispase and 200 UI/mL Collagenase in an orbital shaker at 200 rpm for 90 min at 37° C. Digested homogenate was ground through a 70 µm cell strainer using a 10 mL syringe plunger. Cells were washed out of the strainer by means of Advance Dulbecco's modified Eagle's medium (DMEM), containing 10% v/v Fetal Bovine Serum (FBS), 200 µg/mL L-glutamine, 200 µg/mL penicillin/streptomycin and 250 µg/mL Amphotericin B, and cultured in petri dishes of a surface area of 100 x 20 mm^2 in an atmosphere of 5% CO2 and at 37 _C. Growth medium was changed every 3 days, and at confluence, the cells were trypsinized and harvested for biocompatibility assay. All the reagents for cell culture were purchased from Thermo Fisher Scientific (Milan, Italy).

Cells Culture on PEDOT:Nafion Coatings

Before cellular studies, PEDOT:Nafion coatings were sterilized in 70%v/v ethanol/water solution and dried under laminar flow hood. Then, cells were seeded at a density of 1x 10^4 cells per well on the PEDOT:Nafion coatings put in a 24-well culture plate (Corning® Costar® TC-Treated Multiple Well Plates, Merck Life Science S.r.l., Milan, Italy) and grown in 0.5 mL of complete DMEM for the selected experimental times (see below). Bare plastic dishes (Corning® Costar® TC-Treated Multiple Well Plates, Merck Life Science S.r.l., Milan, Italy) were used as control, unless otherwise specified. We preferred not to include here the PEDOT:PSS dispersion as control group, as the main aim was to collect preliminary evidence on the biocompatibility of conductive coatings obtained from a novel PEDOT:Nafion dispersion rather than compare the latter with a PEDOT:SS dispersion. In addition, different water-based PEDOT:PSS formulations are available, containing additives that can dramatically (positively or negatively) alter the final outcome, hindering a true comparison between different materials[2].

Evaluation of Cell Adhesion by Scanning Electron Microscopy (SEM) and AFM Investigations

Scanning electron microscopy (SEM) was used to qualitatively evaluate morphology of fibroblasts seeded on either PEDOT:Nafion coatings. Before analysis, samples were fixed in 2.5% glutaraldehyde in 0.1 M phosphate buffer (pH 7.4, Merck Life Science S.r.l., Milan, Italy), postfixed in 2% osmium tetroxide in the same buffer, dehydrated in an ascending series of alcohols and dried with hexamethyldisilazane. Samples were then mounted on a metal holder and gold coated (~15 nm) with a Q150RS magnetron sputter (QuorumTech, London, UK). A SEM ZEISS EVO40 XVP (Carl Zeiss NTS GmbH, Oberkochen, Germany) was used, operating at 20 kV acceleration voltage. Circular glass microcoverslips (uncoated glass slides, Waldemar Knittel Glasbearbeitungs GmbH, Braunschweig, Germany) were used as control. Cells attached to the respective substrate were rinsed twice with PBS and fixed with 3% glutaraldehyde in PBS for 45 min. After washing with PBS, dehydration was performed by slow water replacement using series of ethanol/water solution (30%, 50%, 70%, 90%) for 15 min with final dehydration in absolute ethanol for 30 min. AFM was used to gain additional insights about cells adhesion on PEDOT:Nafion coatings and glass substrate. However, for this purpose, no imaging flattening was carried out to preserve correct imaging of cell morphology.

Cell Viability and Proliferation

To evaluate cell proliferation, 2 x 10^4 cells were seeded on PEDOT:Nafion coating and on control group. Fibroblasts viability was analyzed after 1, 3, 5 and 7 days in culture by staining with fluorescein diacetate (15 µg/mL FDA, green), propidium iodide (5 µg/mL PI, red) and Hoechst 33342 (10 µg/mL, blue) dissolved in 1x Ringer–Locke solution and incubation of 10 min at room temperature. Green and red fluorescent cells stain live and dead cells, respectively, and blue stains cell nuclei. After incubation, samples were washed twice with 1x Ringer–Locke solution, and their staining was acquired using an OlympusBX51 fluorescent microscope (MBF Bioscience, Williston, VT, USA) equipped with X-Cite120 fluorescence illumination system (EXFO, Quebec, QC, Canada) and a color digital camera (MBF Bioscience, Williston, VT, USA).

Mitochondrial Function Studies

3-(4,5-Dimethyl-Thiazol-2-yl)-2,5-Diphenyltetrazolium Bromide (MTT) assay (Thermo Fisher Scientific, Milan, Italy) was used to evaluate the reduction-oxidation status of living cells and mitochondrial activity, reflecting cell survival due to the formation of formazan. The absorbance at

560 nm is a measure of the amount of red formazan dye produced by the reduction of yellow tetrazolium salt. The latter is converted by the tetrazolium ring cleavage by succinate dehydrogenase within the mitochondria[3]. Cells were seeded at a density of 2 x 10^4 cells/well in 24-well plates over PEDOT:Nafion coatings and tested after1 day and 7 days. After these times, 100 µL of MTT solution (5 mg/mL in PBS) were added to each sample and incubated for 4 h at 37°C under a CO_2 (5%) atmosphere. The medium was aspirated and 100 µL of dimethylsulfoxide (DMSO) were added to each well for 45 min at 37°C upon a plate shaker. Each sample were transferred in a 96-well plate to read the absorbance at 560 nm using a multimode plate reader spectrophotometer (VICTOR X4, PerkinElmer, Waltham, MA, USA).

Lactate Dehydrogenase (LDH) Measurement

Cells were seeded at a density of 2 x 10^4 cells/well in 24-well plates over PEDOT:Nafion coatings and assayed after 1 day and 7 days. LDH activity was measured CyQUANT™ LDH Cytotoxicity Assay Kit (Thermo Fisher Scientific, Milan, Italy) at 490 nm absorbance, according to the manufacturer's protocol. The absorbance at 490 nm of the amount of red formazan dye is produced by the reduction of yellow tetrazolium salt. In this assay, the formation of formazan is mediated by NADH during the conversion of lactate to pyruvate[4]. Medium from each experimental condition was transferred into a 96-wellplate in triplicate and incubated with the reaction mixture at room temperature for 30 min. The cytotoxicity of PEDOT:Nafion was calculated as: % Cytotoxicity = [(Compound-treated LDH activity − Spontaneous LDH activity)/(Maximum LDH activity − Spontaneous LDH activity)] x 100.

Neutral Red Uptake Assay

Cells were seeded at a density of 2 x 10^4 cells/well in 24-well plates over PEDOT:Nafion coatings and assayed after 1 day and 7 days. Each sample was rinsed with PBS, and 100 µL of 100 µg/mL neutral red solution dissolved in culture medium containing 5% FBS were added to each well. After a 3 h of incubation at 37 °C, neutral red solution was removed, and dye extraction was performed by adding 100 µL of 1% v/v acetic acid in50% v/v ethanol/water solution into each well. The plates were gently shaken for 10 min, and the absorbance was measured at 540 nm. The absorbance at 490 nm is a measure of the amount of red formazan dye produced by the reduction of yellow tetrazolium salt. In this assay, the formation of formazan is mediated by NADH during the conversion of lactate to pyruvate[5].

Section referring to the paper reported in Chapter 3 (in press).

Fabrication of the nanomodulated PEDOT:PSS substrate

Nanomodulated and flat PEDOT:PSS substrates were obtained by electrochemical deposition of PEDOT:PSS on the front and rear part, respectively, of a commercial polycarbonate (PC) compact disk (CD; pitch 1.5 µm, groove width ~ 650 nm, ridge width ~ 850 nm, ridge height ~ 180 nm) upon metallization of the latter. Briefly, after peeling off the CD protective layer, the antistatic layer on the front part was removed by abundant rinsing in ethanol followed by 15 minutes of sonication in (1:1 v/v) ethanol:milliQ water solution. A thin gold film (~30 nm) was then deposited on the surface of the by means plasma sputtering operating in argon using a 99.99% pure gold target (pressure ≈ 10^{-1} bar, time: 3 min, average current: 18 mA). For the electrochemical deposition of PEDOT:PSS, a solution of 0.01 M EDOT ethylenedioxythiophene (EDOT, Sigma Aldrich, MO, USA) and 0.8% w/w poly(sodium 4-styrenesulfonate) (NaPSS, Sigma Aldrich, MO, USA) was prepared. A large-area platinum mesh (30x15 mm^2) and a standard $Hg|Hg_2Cl_2$ electrode were used as counter electrode and reference electrodes, respectively; the metalized PC substrates (flat or nanomodulated) were used as working electrode and contacted with silver conductive paste. The electrochemical polymerization was obtained by chronocoulometry method, to allow a fine control of the amount of deposited charge (75 mC cm^{-2}) and therefore on the final thickness of the PEDOT:PSS layer (~50 nm).

Atomic Force Microscopy (AFM) analysis

The surface topography of the gold-sputtered and the electrodeposited PEDOT:PSS on either flat or nanomodulated PC substrates were investigated by AFM using a Park XE7 AFM system (Park System, Suwon, Republic of Korea) operated in tapping mode in air and at room temperature. Pre-mounted silicon cantilever with Al backside reflective coating and typical tip curvature radius ca. 7nm, elastic constant ca 26 Nm^{-1} and resonance frequency ca. 300 Hz (OMCL-AC160TS, Olympus Micro Cantilevers, Tokyo, Japan) were used. The line profile root-mean-square roughness (RMS) of the different substrate and the thickness of the PEDOT:PSS coating were analyzed by both the Park System XEI software (Park System, Suwon, Korea) and Gwyddion freeware (version 2.61 http://gwyddion.net/).

Electrochemical Characterization

Electrochemical properties of both flat and nanomodulated PEDOT:PSS substrates were evaluated by electrochemical impedance spectroscopy (EIS). EIS measurements in the range 1-10^5 Hz were performed in saline solution (NaCl, 0.15 M) in a three electrode cell using standard Ag|AgCl (3 M KCl) as reference electrode, a large area platinum mesh (30x15 mm^2) as counter electrode and the substrate itself as working electrode.

Electrical characterization

Four-point probe measurements were used to extract sheet resistance values of both flat and nanomodulated PEDOT:PSS substrates[6]. Briefly, four blunt stainless-steel probes were placed in contact with the sample surface at the vertices of a 1x1 cm^2 delimited area. A constant value of current (0.1 mA) was forced for 10 seconds and then raised to the desired value of 0.5 mA using a two channel source-measure unit (Keysight, CA, United States). Measurements were performed both in normal and hydrated condition which was obtained by soaking the sample in milliQ water for one hour. Resistance (R) was extracted from Ohm's law and used to calculate the sheet resistance (Rs) as shown by the following equation[7]:

$$Rs = \frac{(R * \pi)}{ln2}$$

Contact angle measurement

Water contact angle values were measured for all the substrates using a home-build contact angle measurement unit to collect images and ImageJ freeware (Rasband, W.S., ImageJ, U.S. National Institutes of Health, Bethesda, Maryland, USA, https://imagej.nih.gov/ij/, 1997-2018)[8] to extract the angle value (averaged over different areas of at least three different samples for group).

N2A cell culture

In order to evaluate the capability of nanomodulated PEDOT:PSS substrates to support neural cell growth and promote differentiation, we used a mouse Neuro2a (N2A) neuroblastoma cell line (Tema Ricerca, Bologna, Italy) as cell model, being a well-established line for studies of axon growth, neural differentiation and future strategies for the treatments of nerve injuries. Before cellular studies, all substrates were sterilized in 70% *v/v* ethanol/water solution for 30 minutes, dried under laminar flow hood and rinsed twice with sterile phosphate buffer saline (PBS pH 7.4). N2a cells were seeded at a density of 1 x 10^4 cells/well on flat or nanomodulated PC and PEDOT:PSS-coated PC substrates put in 6-well culture plates (Corning® Costar® TC-Treated Multiple Well Plates, Merck Life Science S.r.l., Milan, Italy). Bi-phasic silicon rubber (Silicone RPRO 30) squared pools (1cm x1cm) were fabricated on the surface to confine cells on the substrates. Cells were grown in 1mL of Dulbecco's modified Eagle's medium (DMEM), containing 10% *v/v* fetal bovine serum (FBS), 200 μg/mL L-glutamine, 200 μg/mL penicillin/streptomycin. N2A culture wells were incubated at 37°C with 5% CO_2 and at approximately 90% relative humidity for 36h.

N2A cell viability

Through the generation of formazan as a result of a reduction oxidation process, the 3-(4,5-Dimethyl-Thiazol-2-yl)-2,5-Diphenyltetrazolium Bromide (MTT) assay (Thermo Fisher Scientific, Milan, Italy) was utilized to assess mitochondrial activity. In a brief, cells were seeded onto each substrate condition as previously reported, at a density of 1 x 10^4 cells/well. At DIV1 and DIV6, 5 mg/ml of diluted MTT solution in PBS was added, then the mixture was incubated for 4 hours at 37 °C with a CO2 (5%) atmosphere. The Formazan crystal produced during the experiment was dissolved by adding 100 µl of dimethylsulfoxide (DMSO) to each well and the mixture was shaken for 45 minutes at 37 °C. Each sample was then transferred to a 96-well plate and a multimode plate reader spectrophotometer (VICTOR X4, PerkinElmer, Waltham, MA, USA) was used to measure the absorbance at 570 nm.

N2A cell differentiation

After 36 hours of incubation under the above conditions, each well was rinsed once with PBS and the medium was changed to a reduced amount of serum, combined with the addition of all-*trans* Retinoic Acid (atRA),(ThermoFisher Scientific, Milano, Italy) in order to inhibit cell growth and promote neuronal differentiation. Specifically, the differentiation medium was composed of DMEM containing 1% FBS, 200 μg/mL L-glutamine, 200 μg/mL penicillin/streptomycin and atRA 10μM. 24 hours of atRA stimulation were performed, followed by washing and fixing for DIV1. Up until the achievement of the DIV6, the complete stimulating medium was changed every two days.

Analysis of neurite orientation and average neurite length

In order to analyze neurite orientation, at DIV 1 and DIV 6 the cells were washed with PBS and fixed in 2,5 % glutaraldehyde for 20 minutes, after which they were washed once more before proceeding with dehydration using ethanol at gradually increasing concentrations. Neurite outgrowth, in terms of neurite orientation and average length for cell, was quantified from optical micrographs at 20x magnification using the NeuriteTracer plugin of ImageJ[9], considering only well distinguishable and measurable neurites, aside from those at the edge. At neurite bifurcation points, a single neurite path was selected following the longer branch of the extension. The number of neurite-bearing cells was calculated from at least three independent images obtained from non-overlapping areas on each substrate.

Electrical stimulation experiment

An home-built measurement setup was *ad-hoc* designed to allow DC stimulation of cells seeded on nanomodulated PEDOT:PSS substrates. Briefly, a six multiwell culture plate was modified so that each stimulation well was endowed with two electrodes (gold plate wires), being the terminals at which the stimulating bias was applied. Two of the six wells were used for the control samples (unstimulated group), thus they were not modified. Wires were connected to a multiplexer (outside the cell incubator) which was, in turn, connected to a two channel Keysight B2912A source-measure unit (Keysight, CA, United States) to apply a constant voltage to the samples of 1V (generating an average current of 15 ± 4 μA during the stimulation experiment for all investigated substrates). Cells were electrically stimulated for 6 hours, after having let them grow in undifferentiating medium for 36h and then in differentiating medium for 24h. At the end of the electrical stimulation, cells were further cultured for 18 hours, then fixed and the neurite length measured. Stimulation time was defined based on the results of preliminary tests using smaller stimulation times (1-3 hours) which, however, led to poorly appreciable differences in average neurite length compared to control samples.

Confocal immunofluorescence analysis

Cells were fixed with 4% paraformaldehyde at 4 °C for 20 minutes and then permeabilized with 0.1% Triton X-100 for 5 minutes. After blocking with 2% bovine serum albumin (BSA) in pH 7.4 phosphate buffer saline (PBS) for 1 hour, N2A cells were incubated at room temperature for 3 hours with anti-β-III tubulin recombinant Rabbit Monoclonal Antibody (Life Technologies, Monza, Italy), diluted 1:100 in 0,1% BSA in PBS. The cells were then incubated with Goat anti-rabbit IgG (H+L) Highly Cross-Adsorbed secondary Antibody, Alexa Fluor Plus 488 (Life Technologies, Monza, Italy) at 1:600 dilution in 0,1 % BSA at room temperature for 45 minutes. Intracellular F-Actin was detected with CellMask Deep red Actin Tracking stain (Life Technologies, Monza, Italy) incubate the cells at

1X concentration for 30 minutes at 37° degree. Nuclei were counterstained with 10µg/ml Hoechst 33342 blue dye. Images were acquired with a Nikon A1 confocal laser scanning microscope[10].

SEM analysis of neural cell morphology

For SEM evaluations, cells cultured on substrate at different time points were fixed in 4 % glutaraldehyde in phosphate buffer (pH 7.4), post-fixed in 2 % osmium tetroxide, dehydrated in an ascending series of alcohols and dried with hexamethyldisilazane. Samples were then mounted on a metal stub and gold sputter-coated (15 ~ nm) with Q150RS magnetron sputter (Quorum Tech, London,UK). ASEM ZEISS EVO40 XVP (Carl Zeiss NTS GmbH, Oberkochen, Germany) was used, operating at 20 kV acceleration voltage.

AFM analysis of differentiating neural cells

Differentiating N2A cells were investigated by AFM at different experimental times using the same microscope used for the characterization of film topography, operated in air and upon cell fixation (according to the same protocol used for the SEM analysis). Large area images (40x40 µm) were initially acquired to spot the whole cell; than decreasing scan size images were acquired to get additional insights about lateral dimension of neurite and axons and spot additional details such as morphology of the growth cones.

Section referring to the preliminary study reported in Chapter 4.

Isolation of rat brain microvascular endothelial cells (rBMECs)

The process of isolating primary rat brain endothelial cells was conducted using Long Evans rats aged between 3 and 5 weeks. Cervical dislocation was employed to sacrifice the animals, after which the brain hemispheres were meticulously isolated and submerged in ice-cold DMEM liquid. The meninges were carefully removed by rolling the brains on sterile Whatman filter paper. Following the removal of the meninges from the forebrains, the brain tissues were subjected to mincing using a homogenizer. Subsequently, the minced tissues were subjected to enzymatic digestion using a solution containing collagenase and DNAse. This enzymatic digestion process was carried out for a duration of 1 hour at a temperature of 37°C, utilizing an orbital shaker set at a speed of 180 revolutions per minute. In order to isolate the myelin, the suspension was subsequently combined with a solution consisting of 20% (w/v) BSA/DMEM. Subsequently, the sediment underwent a second round of digestion using a mixed enzymatic solution. During the digestion process, a density gradient percoll solution was established by employing an ultracentrifuge operating at a speed of 3000 times the force of gravity for a duration of 1 hour at a temperature of 4°C. Following this, the digested solution was separated by subjecting it to a centrifugal force of 700 times the force of gravity for a period of 10 minutes at a temperature of 4°C. The cellular structures were readily discernible in the interphase, appearing as a cluster. The interphase was extracted using a sterile needle of considerable length, followed by a further centrifugation of the cells at a force of 1000 times the acceleration due to gravity for a duration of 10 minutes at a temperature of 4 degrees Celsius. The pellet was reconstituted in MCDB 131 containing 20% bovine serum, 200 ng/mL basic fibroblast growth factor (bFGF), 100 µg/mL heparin, 100 µg/mL gentamicin, and 2.5 mM 4-(2-hydroxyethyl)-1-piperazineethanesulfonic acid (HEPES) supplemented with 4 µg/mL puromycin. The pellet that had been resuspended was carefully transferred to culture plates that had been precoated with collagen type IV and fibronectin.

Intracortical device coating

In order to coat intracortical neural devices, endothelial cells that were previously obtained from rat brain, as explained in the preceding section, were subjected to trypsinization and subsequently resuspended in a manner that resulted in a concentration of 200.000 cells per 500ml of culture media. The cylindrical or shank-shaped device was immersed in the cell solution for a duration of 24 hours while continuously rotating, enabling the adherence of cells over the entirety of the device surface.

Surgical Procedures

The male Long Evans rats were subjected to anesthesia using an isoflurane vaporizer, with a concentration of 3% in oxygen for induction and 1.5% for the duration of the treatment. The rats' unconsciousness was verified using the toe pinch method. Following the process of induction, every animal was affixed to a stereotactic frame (David Kopf Instruments, USA) and subjected to thermal stimulation using a hot water pad (Farmigea, Italy) set at a temperature of 37° C. Following the procedures of shaving and sterilizing of the implantation site using iodine and ethanol, an incision was performed to expose the lambda and bregma lines of the cranial vault. Regarding the coronal suture, bilateral bone screw sites were created at 1 mm anterior to lambda and 1.5 mm distal from the midline using a surgical drill equipped with a 0.007 drill bit. Saline rinses were conducted on the cranial surface to safeguard the animal and mitigate the thermal effects resulting from the drilling process. Two bone screws made of Stainless Steel, with a shaft diameter of 1.17 mm and a length of 4.7 mm, were inserted, ensuring meticulous care was taken to avoid penetrating the brain tissue. Two electrode holes were created at a location 2 mm posterior to the lambda point and 2 mm from the midline. Non-functional electrodes manufactured by Neuro Nexus were then put into the holes and sealed using Kwik-Cast Sealant, (World Precision Instruments Inc, USA). In this work, the utilization of dummy probes was preferred over functional probes due to the high costs associated with the latter and the absence of necessity for the specific tests conducted. Subsequently, dental cement was administered in a liberal manner and subsequently solidified using ultraviolet (UV) light at each of the four designated locations. This procedure was performed to secure the probes in position and create a protective head helmet. The incision sites were closed with sutures and treated with a topical antibiotic. Additionally, the animals were administered an intraperitoneal injection of Ketofen at a dosage of 5 mg/kg. The Ketofen used in this study was a solution with a concentration of 100 mg/mL (Zoetis Inc, located in Kalamazoo, MI, USA). The rats were returned to their designated cages and positioned on a warming pad until they regained consciousness. The administration of Ketofen injections at a dosage of 5 mg/kg was maintained daily for a duration of three days following the surgical procedure, with the aim of managing postoperative pain. At the two-week mark, the animals were administered an excessive dosage of ketamine/xylazine (80 - 100 mg/kg and 5 - 10 mg/kg, respectively), as seen by the absence of the toe/tail pinch response. A surgical procedure involved the creation of an incision to reveal the diaphragm, which was subsequently removed to expose the thoracic cavity. The rats were subjected to perfusion using 100 mL of phosphate-buffered saline (PBS) followed by an additional 100 mL of cold 4% paraformaldehyde (PFA) solution in PBS. The inferior portion of the cranium was surgically excised to provide access to the cerebral organ, and subsequently, the cranium was immersed in a 4% paraformaldehyde solution at a temperature of 4 degrees Celsius for a duration of 4 to 6 hours. The brains were preserved in a sucrose solution, frozen, and subsequently cut into slices that were 10μm thick using cryosectioning techniques.

Immunohistochemistry (IHC)

Immunohistochemical staining was performed on tissue slices that included the site of implant damage. The staining procedure involved rehydration of the brain slices in citrate buffer, followed by blocking with 10% goat serum. Subsequently, the brain slices were treated with 0.1% Triton-x for a duration of 45 minutes. The staining of the brains was conducted using specific antibodies targeting NeuN (Millipore mouse 1:250), NF200 (Abcam rabbit 1:500), Iba-1 (Millipore mouse 1:500), GFAP (DAKO rabbit 1:500), and Caspase-3 (Cell Signaling mouse 1:500). The selected stains were employed with the purpose of identifying the existence of reactive astrocytes (GFAP), neuronal axons (NF200) and density (NeuN), microglia (Iba-1), and apoptosis (Casp-3) in the vicinity of the implantation sites. The relative intensity of these antibodies was used as a basis for comparing the control group and the cell coated group.

<u>Section referring to the published paper reported in Chapter 5.</u>

DOI: 10.4103/1673-5374.346054

Neurosurgery harvest and isolation of hBMEC culture

The hBMECs were isolated from cortical GM and subcortical WM biopsies obtained during scheduled brain tumor resection surgery from five Caucasian male patients (M1-M2-M3-M4-M5) aged 55–72 years old and five Caucasian female patients (F1-F2-F3-F4-F5) aged 65–75 years old, diagnosed with grade II or III glioma and/or meningioma. The protocol was approved by the local Ethical Committee, Comitato Etico di Area Vasta Emilia Centro (approval code number CE-AVEC 640/2018/Sper/UniFe) on October 18, 2018. Peritumoral neurosurgical resections were collected at the Azienda Ospedaliero-Universitaria of Ferrara (Italy), using standard operating procedures for enrollment and consent of only adult patients, as well as for tissue collection, handling, and de-identification of patient clinical data. Postmenopausal condition was inferred by the age of female patients. It has to be specified that the neurosurgical intervention itself was not the subject of this study. Resected tissues were immediately transferred to sterile conical tubes containing ice-cold Hibernate A medium (Thermo Fisher Scientific, Milan, Italy) supplemented with 50X B27 Plus and 50 mM GlutaMAX-I supplements (Thermo Fisher Scientific) and delivered to the laboratory of translational neurophysiology of the University of Ferrara. The hBMECs were isolated from GM and/or WM resections as previously described[11] with slight modifications. Briefly, a gentle mechanical dissociation of both GM and WM specimens weighing 300–400 mg was performed with a glass potter followed by the first step of digestion using a mixture of collagenase/dispase (270 IU collagenase/mL, 0.1% w/v dispase) and DNAse (10 IU/mL) in Advanced DMEM serum-free medium (Thermo Fisher Scientific) for 60 minutes at 37°C in a thermostatic orbital shaker. The cell pellets were separated and demyelinized by 20% w/v bovine serum albumin (BSA)/DMEM by centrifugation (1000 × *g* for 15 minutes, at 4°C), followed by second digestion of the pellet in the collagenase/dispase mixture for 45 minutes at 37°C. According to previously reported methods of primary cultures of human brain microvascular endothelial cells by Weksler et al. (2005) and Park et al. (2022), capillary endothelial cells were retained on a 10-µm nylon mesh cell strainer, removed from the filter with MCDB 131 medium (Thermo Fisher Scientific), an endothelial cell basal medium for the culture of human microvascular endothelial cells, supplemented with 20% v/v bovine plasma-derived serum (PDS; First Link Ltd., Birmingham, UK) and antibiotics (penicillin, 100 IU/mL; streptomycin, 100 µg/mL), seeded on 30-mm Petri dishes and then flasks coated with 150 µg/mL rat tail collagen type I (Thermo Fisher Scientific). During the first 2 days of culture, the hBMEC medium contained 4 μg/mL puromycin to eliminate P-glycoprotein negative contaminating cell types[11]. Vascular endothelial growth factor (VEGF; 1 μg/mL) was then added to the medium. Following this procedure, only BMECs expressing high levels of P-glycoprotein selectively survived over other cell types[11]. This culture medium was then removed and replaced by the same MCDB 131 medium supplemented with 20% bovine plasma-derived serum but containing a mixture of 2 ng/mL basic fibroblast growth factor, 500 ng/mL hydrocortisone, 1 μg/mL VEGF. This latter culture medium was further spiked with 10 nM β-estradiol 17-acetate, dissolved in dimethyl sulfoxide (DMSO), which reached a 0.0001% final concentration of vehicle in the medium, used to grow WM-derived hBMECs freshly isolated from female patients F4–F5 immediately after thawing and splitting; otherwise used to grow GM-derived hBMECs isolated from patients M1- M2-M3-M4 exclusively to allow their growth immediately after thawing and splitting. All the above hormones and growth factors were purchased from Merck, Milan, Italy. All hBMEC cultures were incubated at 37°C, 95% humidity, and 5% CO_2 until cells reached approximately 80% confluence when cells were passaged using trypsin/EDTA (Thermo Fisher Scientific). All the hBMECs growing in culture were cryopreserved at confluence in freezing medium consisting of 90% FBS plus 10% DMSO and stored at –80°C.

Cell counting on phase contrast images of hBMECs two-dimensional monolayers

Cell morphology was examined by phase contrast microscopy imaging in a Motic microscope (Seneco S.r.l., Milan, Italy) using phase-contrast optics and related images were acquired with a Moticam digital camera (Seneco S.r.l.). hBMECs were routinely photographed under a light phase-contrast microscope, the related images acquired and counted by ImageJ 1.46r software (Image Processing and Analysis in Java; available at https://imagej. nih.gov/ij/index.html) to estimate cell number and density. Each image was initially converted to grayscale before adjusting the threshold to highlight cells. Later, to split up the merged cells, the watershed tool was used. After applying these functions, a binary image was created for cell counting. Data for growth curves were then plotted as graphs and analyzed with GraphPad Prism 8.43 (GraphPad Software, San Diego, CA, USA, www.graphpad.com)

Trypan blue exclusion test for viability evaluation of hBMECs

Cell viability of male and female GM- and WM-derived hBMECs cultured on 30-mm Petri dishes was determined by trypan blue exclusion test following the procedure of Hansen et al. (2021)[12]. Confluent cells were harvested in 5 mL of growth medium. About 1 mL aliquot of cell suspension was centrifuged for 5 minutes at 100 × g. Cell pellets were resuspended in 1 mL of PBS.

Approximately 100 μL of this suspension was mixed with 100 μL of 0.4% Trypan blue solution (Thermo Fisher Scientific). Cells excluding Trypan blue (viable cells) and dead cells were counted under the microscope using a Bürker hemocytometer (Brand GmbH, Wertheim, Germany). The percentage of viable cells was calculated as follows: Viable cells (%) = total number of viable cells per mL cell suspension /total number of cells per mL cell suspension× 100. The resulting data were plotted as graphs and analyzed with GraphPad Prism 8.43 (GraphPad Software).

Immunofluorescence staining

The primary antibodies mouse anti-human CD62E (Cat# MCA1969, RRID: AB_2186827), mouse anti-human CD31 (Cat# MCA1738, RRID: AB_322710) and mouse anti-human CD54 (Cat# MCA532, RRID: AB_321784) were purchase from Bio-Rad Laboratories S.r.l, Milan, Italy, and were used at the company's recommended working dilution for immunofluorescence. CD62E antibody is the endothelial leukocyte adhesion molecule-1 marker that mediates the initial interaction of leukocytes and platelets with endothelial cells, and it was directed towards the binding site of leukocytes to human E-selectin. Epitope recognized by CD31 antibody also known as platelet endothelial cell adhesion molecule 1 (PECAM-1) is an essential marker for transendothelial migration under most inflammatory conditions. It has been mapped to be within residues 228 and 234 of cluster of differentiation 3. The epitope of CD54 antibody, also known as inter cellular adhesion molecule 1 (ICAM-1), is the intracellular adhesion molecule-1 that participates in cell-cell adhesion between leukocytes and endothelial cells, facilitating leukocyte recruitment and transmigration at the sites of inflammation. It has been mapped to the first domain of the ICAM-1 molecule. Secondary antibodies fluorochrome-conjugated goat anti-mouse Alexa Fluor 488 (Cat# A-21121, RRID: AB_2535764), goat anti-mouse Alexa Fluor 568 (Cat# A-21124, RRID: AB_2535766), and goat anti-mouse Alexa Fluor 633 (Cat# A-21146, RRID: AB_2535782) were purchased from Thermo Fisher Scientific and were used at the manufacturer's recommended working dilution.

The hBMECs were seeded on the glass bottom coated with 150 μg/ mL collagen type I of CELLVIEW$_{TM}$ culture dishes (Greiner Bio-One, VWR International, Milan, Italy) and grown until confluence. The cells were then washed three times with the Hank's buffer salt solution (HBSS), fixed in 3% v/v paraformaldehyde for 15 minutes at room temperature (RT) and incubated with 5% w/v BSA/HBSS blocking solution for 60 minutes at room temperature on an orbital shaker. Mouse anti-human CD62 monoclonal antibody, mouse anti-human CD31 monoclonal antibody and mouse anti-human CD54 monoclonal antibody were used with a dilution of 1:50 and incubated for 4 hours at room temperature. Then, secondary antibodies fluorochrome-conjugated goat anti-mouse Alexa Fluor

488, goat anti-mouse Alexa Fluor 568 and goat anti-mouse Alexa Fluor 633 were used at a dilution of 1:400 and incubated for 1 hour at room temperature in the dark. Total nuclei were stained with 15 µg/mL Hoechst 33342 blue dye solution (Cat# B2261, Merck). Immunofluorescence staining of all markers was merged with the nuclear Hoechst dye. The cells were washed three times with HBSS and embedded with glycerol/PBS 1:1, and finally stored at 4°C until images were acquired by an Olympus BX51 fluorescence microscope using Neurolucida software (MBF Bioscience, Williston, VT, USA). Cell fluorescence intensity was measured by ImageJ 1.46r software (Image Processing and Analysis in Java; available at https://imagej.nih.gov/ij/index.html). The corrected total cell fluorescence (CTCF) was calculated using the following formula: CTCF = integrated density - (area of selected cell × mean fluorescence of background readings). Data were then plotted as graphs and analyzed with GraphPad Prism 8.43 (GraphPad Software).

Positive control for primary antibody staining

hCMEC/D3 human cerebral microvascular endothelial immortalized cell line (Cat# CLU512, RRID: CVCL_U985; Weksler et al., 2005) was employed as positive control fitting for all primary antibodies. hCMEC/D3 cells were activated by human tumor necrosis factor-alpha (TNF-α; Thermo Fisher Scientific) as previously reported[13–15]. hCMEC/D3 cells were purchased from TebuBio (Magenta, Milan, Italy) and cultured under similar conditions for primary hBMECs. Subsequently, hCMEC/D3 cells were grown to confluence on 150 µg/mL rat tail type I collagen coated glass coverslips in the 30-mm Petri dishes, washed with fresh MCDB 131 medium, and activated by 24-hour stimulation with 10 ng/mL TNF-alpha in the same medium. Finally, cells were washed and labeled with antibodies CD62-E, CD54 and CD31, and processed for the visualization and quantification of cells immunofluorescence intensity as described above.

Data Analysis

Data analysis and graphing has been performed with Graphpad software (GraphPad, version Prism 9.5.1, GRAPHPAD 2365 Northside Dr., San Diego, CA, USA, 2102) and Matlab (version 9.10, Mathworks, Natick, MA, USA) for all the experiments in this thesis.

In Vitro statistical Analysis

All data were presented as mean ± standard deviation (SD). In particular, data from biological experiments were analyzed by Graphpad software applying one-way analysis of variance followed by Bonferroni's multiple comparisons test or Dunnet's *post hoc* test and two-way analysis of variance (ANOVA) followed by Tukey's multiple comparisons test and unpaired t-test for statistical comparison between control and materials tested in several assays. Level of significance was set at $^*p < 0.05$. Data were expressed as means ± standard deviations of experiments carried out in triplicate.

Immunohistochemistry histology Analysis

Images of slices were obtained using confocal fluorescent microscopy (OlympusFluoview 1000). Images were analyzed in a custom Matlab script. Bins of 10 µm were created concentrically around the probe implant and the intensity of the stain or number of cells labeled per bin was measured. Intensities and counts were scaled to control regions at the corners of the images. Background intensity was calculated from the corners of the image (20% of the total image area) by removing pixels greater than 1 standard deviation (STD) above the mean and calculating the mean and variance of the remaining pixels. All pixels greater than 1STD above the mean background intensity were used for analysis. Manual blinded counts within masked bins were performed to obtain the data for NeuN and Caspase-3.

BIBLIOGRAPHY

1. Carli, S. et al. Water-Based PEDOT:Nafion Dispersion for Organic Bioelectronics. ACS Appl. Mater. Interfaces 12, 29807–29817 (2020).

2. Stříteský, S. et al. Printing inks of electroactive polymer PEDOT:PSS: The study of biocompatibility, stability, and electrical properties. Journal of Biomedical Materials Research Part A 106, 1121–1128 (2018).

3. Fotakis, G. & Timbrell, J. A. In vitro cytotoxicity assays: Comparison of LDH, neutral red, MTT and protein assay in hepatoma cell lines following exposure to cadmium chloride. Toxicology Letters 160, 171–177 (2006).

4. Kumar, P., Nagarajan, A. & Uchil, P. D. Analysis of Cell Viability by the Lactate Dehydrogenase Assay. Cold Spring Harb Protoc 2018, pdb.prot095497 (2018).

5. Repetto, G., del Peso, A. & Zurita, J. L. Neutral red uptake assay for the estimation of cell viability/cytotoxicity. Nat Protoc 3, 1125–1131 (2008).

6. Bianchi, M. et al. Scaling Capacitance of PEDOT:PSS: Volume vs Area. Journal of Materials Chemistry C.

7. Singh, Y. Electrical resistivity measurements: a review. Int. J. Mod. Phys. Conf. Ser. 22, 745–756 (2013).

8. Schneider, C. A., Rasband, W. S. & Eliceiri, K. W. NIH Image to ImageJ: 25 years of image analysis. Nature Methods 9, 671–675 (2012).

9. Bertani, G. et al. Flow-dependent shear stress affects the biological properties of pericyte-like cells isolated from human dental pulp. Stem Cell Research & Therapy 14, 31 (2023).

10. Bertani, G. et al. Flow-dependent shear stress affects the biological properties of pericyte-like cells isolated from human dental pulp. Stem Cell Research & Therapy 14, 31 (2023).

11. Perrière, N. et al. Puromycin-based purification of rat brain capillary endothelial cell cultures. Effect on the expression of blood–brain barrier-specific properties. Journal of Neurochemistry 93, 279–289 (2005).

12. Hansen, C. et al. High metabolic substrate load induces mitochondrial dysfunction in rat skeletal muscle microvascular endothelial cells. Physiological Reports 9, e14855 (2021).

13. Weksler, B. B. et al. Blood-brain barrier-specific properties of a human adult brain endothelial cell line. The FASEB Journal 19, 1872–1874 (2005).

14. Jassam, S. A. et al. TNF-α enhancement of CD62E mediates adhesion of non–small cell lung cancer cells to brain endothelium via CD15 in lung-brain metastasis. Neuro-Oncology 18, 679–690 (2016).

15. Dunst, J., Kamena, F. & Matuschewski, K. Cytokines and Chemokines in Cerebral Malaria Pathogenesis. Frontiers in Cellular and Infection Microbiology 7, (2017).

LIST OF FIGURES

PEDOT:Nafion coating (b); cell density (c) at different time points (** $p < 0.01$, *** $p < 0.001$, **** $p < 0.0001$).

Figure 2.5 | Evaluation of fibroblasts viability on PEDOT:Nafion coating. Cytotoxicity of the PEDOT: Nafion coating was evaluated by MTT (a), LDH (b) and neutral red assay (c) at 1 day and 7 days after seeding (* $p < 0.05$, ** $p < 0.01$, **** $p < 0.0001$).

Figure 3.1 | Fabrication and characterization of the NanoPEDOT. a) Sketch of the fabrication process, encompassing metallization of a nanomodulated polycarbonate substrate and subsequent PEDOT:PSS electrodeposition. b) AFM analysis of the substrates investigated in this study: 2D topography image (i) and 3D rendering (ii) of NanoPEDOT; 3D topography of NanoPC (iii), height profiles NanoPEDOT and NanoPC (iv); 3D rendering of FlatPEDOT (v) and FlatPC (vi). c) Water contact angle and (d) EIS spectra of the investigated samples. e) Sheet resistance under dry and wet conditions of FlatPEDOT and NanoPEDOT

Figure 3.2 | Evaluation of N2A cell differentiation on NanoPEDOT. Results from a) MTT and b) proliferation tests. *, **, **** refer to $p < 0.05$, $p < 0.01$ and $p < 0.001$, respectively. c) Scanning electron microscopy (c) and immunofluorescence (d) images of N2A cells at DIV 6 on NanoPEDOT. In d), the following neuronal markers are shown: β-III Tubulin (green), Intracellular F-Acting (red) and Hoechst 33342 (blue); the double-ended arrows are a guide-for-the-eye to show the main direction of the pattern compared to the direction of the axons.

Figure 3.3 | Analysis of cell neurite polarization. a) Polar plots showing the angular distribution of neurites with respect to the main pattern direction (indicated by the dotted line) at DIV 6. Each sector corresponds to a range of 15° deg. (b) Average neurite length per cell at DIV1 and DIV6.

Figure 3.4 | AFM analysis of neurite morphology on NanoPEDOT (DIV6). a) (45 μm x 30 μm) 3D topography image of parallel neurites from different cells. b) (20 μm x 10 μm) topography image (i) and height profile (ii) of a portion of axon. c) line profile from a), showing the presence of both axonal and smaller neurite processes. d) combination of four different AFM scans (i) enabling to follow one single neurite up to more than 100 mm of length; (ii) detail from (i) showing the squeezing of the neurite inside the nanogroove and (iii) relative height profiles. e) 3D rendering (i) and relative height profiles (ii) of a growth cone.

Figure 3.5 | Electrical stimulation of neural cells on nanoPEDOT. a) Sketch of the setup used for the electrical stimulation experiment. b) Average neurite length of N2A differentiating on NanoPEDOT and FlatPEDOT with and without electrical stimulation. c) Representative AFM image of neurites sprouted from stimulated (top) and non-stimulated (bottom) N2A cells on NanoPEDOT.

Figure.4.1 | Morphological representation of rat BMECs. (a) Day 0 of isolated rBMECs . (b) Day 5 of isolated rBMECs after culture purification with puromycin. 200 µm scale bar applied.

Figure 4.2 | Intracortical device type and delamination evaluation. (a) planar shape Neuronexus A-style probe. (b) cylindrical shape Thomas type wire probe. (c) Histogram showing non-significant difference in Calcein AM intensity between "pre insertion" and "post insertion" conditions (d-e) Exemplary rBMECs-coated Thomas-type wire stained with Calcein AM before (d) and after (e) insertion in "brain phantom".

Figure.4.3 | Neuron density close to the electrode site is preserved by rBMECs device coating. (a) NeuN (neurons) and NF200 (axons) staining representative images for the groups of control and BMEC-coated devices. (b)Number of neurons per square micrometer (¼m) as a function of the distance from the implant center is shown. (c) Histogram showing the neuron density average in coated and uncoated devices, with statistically significant difference. (d) NF200 intensity as a function of distance from electrode, normalized to image corners. (e) A histogram showing the normalized NF200 intensity average. (**: $p < 0.01$, two-way ANOVA).

Figure 4.4 | Caspase-3 expression is reduced by rBMECs device coating. (a) Caspase-3 (apoptosis marker) staining representative images for the groups of control and cell-coated devices. Areas expressing Caspase-3 are shown by red arrows. Caspase-3 (green) and NeuN (grey) overlay to show neuron death. (b) The two groups' Caspase-3 numbers at various distances from the electrode center (n.s.Two-way ANOVA).

Figure 4.5 | Astrocytic and microglial activation close to the electrode is inhibited by the device coating of rBMECs. (A) GFAP (astrocytes) and Iba-1 (microglia) staining representative photos of the control and cell-coated device groups. (b) GFAP intensity plotted against distance from electrode center, normalized to image corners. (c) A bar graph showing the average normalized GFAP intensity. (d) Iba-1 intensity normalized to image corners plotted against electrode center distance. (c) Bar graph showing the average normalized Iba-1 intensity. (**: $p < 0.01$, Two-way ANOVA).

Figure 5.1 | Effects of donor's gender, tissue source and 10 nM β-estradiol 17-acetate on hBMECs recovery and growth after fresh isolation from neurosurgical specimens. Representative phase contrast images of morphology and density of female WM-derived hBMECs spiked with 10 nM β-estradiol 17-acetate, after 4 and 22 days in culture from isolation. Scale bars: 20 µm. (B) Representative phase contrast images of male GM-derived hBMECs in the absence of 10 nM β-estradiol 17-acetate, and male WM-derived hBMECs in the absence and presence of 10 nM β-estradiol 17-acetate, after 4 and 22 days in culture from isolation. Scale bar: 20 µm. (C) Comparison between growth curves of GM-derived hBMECs freshly isolated from male patients M1-M4 in the absence of 10 nM β-estradiol 17-acetate (blue squares) and WM-derived hBMECs freshly isolated from male patients M2-M5 in the absence (green circles) and presence of 10 nM β-estradiol 17-acetate (violet triangles) and WM-derived hBMECs isolated from female patients F4 and F5 and spiked with 10 nM β-estradiol 17-acetate (dark pink triangles). Each independent culture was related to GM-derived hBMECs (*n* = 4) and to WM-derived hBMECs (*n* = 4) obtained from male patients, and to WM-derived hBMECs (*n* = 2) obtained from female patients. Each point represents the mean ± SEM of four experiments from individual cell preparations obtained from each donor. Effects of days of culture, gender and/or estrogen treatment on growth curves were analyzed by two-way analysis of variance followed by the Tukey's multiple comparisons test. **P* = 0.001 for male GM-hBMECs vs. male WM-hBMECs; °*P* = 0.05 for male WM-hBMECs *vs*. male β-estradiol 17-acetate-treated WM-hBMECs; §*P* = 0.001 for female β-estradiol 17-acetate-treated WM-hBMECs *vs*. male GM-hBMECs; £*P* = 0.01 for female β-estradiol 17-acetate-treated WM-hBMECs *vs.* male β-estradiol 17-acetate-treated WM-hBMECs. GM: Gray matter; hBMECs: Human cerebral microvascular endothelial cells; WM: white matter.

Figure 5.2 | Effect of donor's gender, tissue source and 10 nM β-estradiol 17-acetate on hBMECs recovery and growth after thawing from cryopreservation and splitting. (A) Representative phase contrast images of morphology and density of male GM-derived hBMECs and of female WM-derived hBMECs subcultured for 6 days and 12 days, respectively, after thawing from cryopreservation both in the presence and in the absence of 10 nM β-estradiol 17-acetate. Scale bars: 20 μm. (B) Comparison between growth curves related to GM-derived hBMECs isolated from male patients M1-M4, thawed and subcultured in the absence (blue triangles) and in the presence (violet squares) of 10 nM β-estradiol 17-acetate, and growth curves related to WM-derived hBMECs isolated from female patients F4–F5, thawed and subcultured in the presence (pink triangles) and in the absence (red circles) of 10 nM β-estradiol 17-acetate. (C) Effects of withdrawal (blue circles) and new addition (violet triangles) of 10 nM β-estradiol 17-acetate on recovery and growth after thawing of GM-derived hBMECs isolated from male patients M1-M5 and effects of withdrawal of 10 nM β-estradiol 17-acetate on recovery and growth after thawing of WM-derived hBMECs isolated from female patients F4–F5, each subcultured after thawing. The inserted graph represents the magnification of the failed recovery after withdrawal and re-addition of 10 nM β-estradiol 17-acetate in WM-derived hBMECs from female patients F4–F5. Each point represents the mean ± SEM of four experiments from individual cell preparations obtained from each donor. Effects of thawing, gender and/or estrogen treatment on growth curves were analyzed by two-way analysis of variance (*P* = 0.0001) followed by the Tukey's multiple comparisons test. (B) Male GM-derived hBMECs with estrogen *vs*. male GM-derived hBMECs without estrogen, **P* = 0.0001; female WM-derived HBMECs with estrogen *vs*. female WM-derived hBMECs without estrogen, °*P* = 0.0001. (C) Male GM-derived hBMECs withdrawal of estrogen v*s*. male GM-derived hBMECs re-addition of estrogen, **P* = 0.0002; male GM-derived hBMECs re-addition of estrogen *vs*. female WM-derived hBMECs readdition of estrogen, ***P* = 0.0007. GM: Gray matter; hBMECs: Human cerebral microvascular endothelial cells; WM: white matter.

Figure 5.3 | Cell viability. (A) Phase contrast images of bright fields of the hemocytometer and (B) quantification of the live/dead trypan blue exclusion assay, referred to male GM- and WM-derived hBMECs and female WM-derived hBMECs, each of them splitted after thawing. Red arrows indicate dead cells. Scale bar = 50 μm. No statistical differences (NS) in viability resulted from one-way analysis of variance (*P* = 0.1035) followed by Bonferroni's multiple comparisons test, performed on three aliquots of cells deriving from three independent cultures (*n* = 3) of each male GM- and WM-derived hBMECs and female WM-derived hBMECs, respectively. GM: Gray matter; hBMECs: Human cerebral microvascular endothelial cells; WM: white matter

Figure 5.4 | Visualization and quantification of immunofluorescence staining of CD31, CD54 and CD62E markers in representative cultures of male GM- and WM-derived hBMECs and female WM-derived hBMECs. (A) Constitutive expression of the endothelial marker CD31 or PECAM-1 was shown for all the types of hBMECs both after fresh isolation and after thawing from cryopreservation. TNF-α activated hCMEC/D3 cells were used as positive control for staining of CD31. CD31 primary antibody was stained in green by fluorochrome-conjugated goat anti-mouse secondary antibody Alexa Fluor 488 and nuclei were stained by the blue Hoechst 33342 dye. (B) Immunofluorescence intensity quantification (in arbitrary units; A.U.) of CD31-stained hBMECs in comparison to the TNF-α activated hCMEC/D3 cells, CD31 positive control. Scale bars: 50 μm. **P = 0.0075, ***P = 0.0002, ****P = 0.0016, *****P = 0.0003. (C) CD54 or ICAM-1 exhibited a low expression in male GM-derived hBMECs and female WM-derived hBMECs compared with the positive control TNF-α activated hCMEC/D3 cells, as shown by fluorescence intensity quantification. CD54 primary antibody was stained in red by fluorochrome-conjugated goat anti-mouse secondary antibody Alexa Fluor 633 and nuclei were stained by the blue Hoechst 33342 dye. Scale bars: 50 μm. *P = 0.0167, ***P = 0.0004, ****P = 0.00001. (D) CD62E or E-Selectin was clearly seen as being negative both for male GM-derived hBMECs and female WM-derived hBMECs in comparison with the TNF-α activated hCMEC/ D3 cells, as shown by fluorescence intensity quantification. CD62-E primary antibody was stained in orange-yellow by fluorochrome-conjugated goat anti-mouse secondary antibody Alexa Fluor 568 and nuclei were stained by the blue Hoechst 33342 dye. All the endothelial markers were merged with the nuclear Hoechst 33342 dye. Scale bars: 50 µm. Each point represents the mean ± SEM of four experiments from individual cell preparations obtained from each donor. Significance was calculated by one-way analysis of variance followed by Dunnet's post hoc test, comparing each marker staining in hBMECs with its staining in hCMECs/D3 positive control. AT: After thawing; FI: Fresh isolation; GM: gray matter; hBMECs: Human cerebral microvascular endothelial cells; WM: white matter.

LIST OF PUBBLICATIONS and CONFERENCES

Publications:

Magistroni, R. et al. TRPP2 dysfunction decreases ATP-evoked calcium, induces cell aggregation and stimulates proliferation in T lymphocytes. *BMC Nephrology **20**, 355 (2019).*

Patergnani, S. et al. The induction of AMPK-dependent autophagy leads to P53 degradation and affects cell growth and migration in kidney cancer cells. *Experimental Cell Research **395**, 112190 (2020).*

Guzzo, S. et al. Evaluation of the In Vitro Biocompatibility of PEDOT:Nafion Coatings. *Nanomaterials **11**, 2022 (2021).*

Guzzo, S., De Bonis, P., Pavan, B. & Fadiga, L. β-Estradiol 17-acetate enhances the in vitro vitality of endothelial cells isolated from the brain of patients subjected to neurosurgery. *Neural Regeneration Research **18**, 389 (2023).*

Bianchi, M. et al. Synergy of nanotopography and electrical conductivity of PEDOT:PSS for enhanced neuronal development. *ACP Applied Materials and Interfaces **15**, 51, 59224–59235 (2023).*

Conferences:

“Biohybrid microelectrodes coated with human brain microvascular endothelial cells (hBMECs) as a novel therapeutic tool for taking foreign body reaction”; 16th International Summer Schools on Nanosciences & Nanotechnologies, Organic Electronics & Nanomedicine (ISSON22).

"Evaluation of cell viability in primary fibroblast cultures with materials for neural interfaces"; 1st Workshop on Neuromorphic Organic Devices.

"Development of neural devices which use endothelial cells isolated from human brain capillaries"; 1st Workshop on Neuromorphic Organic Devices.

“Multiscale patterning of conducting polymers: applications in neurotechnology”; 78th International Workshop & 6th Orbitaly.

Acknowledgments